12 SECTOR DTC AND PSO-PI CURRENT CONTROL TECHNICS OF Z-SOURCE MATRIX CONVERTER FOR IM DRIVE

SEYED SINA SEBTAHMADI

FACULTY OF ENGINEERING
UNIVERSITY OF MALAYA
KUALA LUMPUR

2016

12 SECTOR DTC AND PSO-PI CURRENT CONTROL TECHNICS OF Z-SOURCE MATRIX CONVERTER FOR IM DRIVE

SEYED SINA SEBTAHMADI

THESIS SUBMITTED IN FULFILMENT OF THE REQUIREMENTS FOR DOCTOR OF PHILOSOPHY

FACULTY OF ENGINEERING
UNIVERSITY OF MALAYA
KUALA LUMPUR

2016

UNIVERSITY OF MALAYA

ORIGINAL LITERARY WORK DECLARATION

Name of Candidate: SEYED SINA SEBTAHMADI

Registration/Matric No: KHA120009

Name of Degree: DOCTOR OF PHILOSOPHY

Title of Thesis:

12 Sector DTC and PSO-PI Current Control Technics of Z-Source Matrix Converter for IM Drive

Field of Study:

Power Electronics

I do solemnly and sincerely declare that:

(1) I am the sole author/writer of this Work;
(2) This Work is original;
(3) Any use of any work in which copyright exists was done by way of fair dealing and for permitted purposes and any excerpt or extract from, or reference to or reproduction of any copyright work has been disclosed expressly and sufficiently and the title of the Work and its authorship have been acknowledged in this Work;
(4) I do not have any actual knowledge nor do I ought reasonably to know that the making of this work constitutes an infringement of any copyright work;
(5) I hereby assign all and every rights in the copyright to this Work to the University of Malaya ("UM"), who henceforth shall be owner of the copyright in this Work and that any reproduction or use in any form or by any means whatsoever is prohibited without the written consent of UM having been first had and obtained;
(6) I am fully aware that if in the course of making this Work I have infringed any copyright whether intentionally or otherwise, I may be subject to legal action or any other action as may be determined by UM.

Candidate's Signature Date:

Subscribed and solemnly declared before,

Witness's Signature Date:

Name:

Designation:

ABSTRACT

The first stage of this study investigates the sophisticated analysis of a novel switching strategy for a matrix converter (MC) based direct torque control (DTC) of an induction motor (IM) drive. The proposed switching paradigm utilizes twelve 30° sectors for both flux and voltage vectors. Analytical expressions of change rates of torque and flux for IM as a function of MC's voltage vectors are derived. The influence of MC's voltage vectors on the stator flux and electromagnetic torque variation is examined and an advanced switching scheme independent of any load and speed variation is developed. To decrease the switching losses of MC, the optimum switching state is selected by means of discretization and averaging on the flux variations. The performance of the proposed switching strategy is validated under rated conditions, and compared to the conventional hexagonal boundary switching scheme. In the proposed method, the characteristic of low torque ripples can be achieved with no need of rotational coordinate transformation and minimized switching frequency. The results verify that the degree of freedom to select proper voltage increases, and the torque ripple is hence significantly reduced up to 60% in comparison with the standard DTC method.

The second phase of this study illustrates an IM fed by an Ultra Sparse Z-source Matrix Converter (USZSMC) under abnormal rate of input voltage, which reduces the THD of the output current by applying the intelligent method in the Particle Swarm Optimization (PSO) PI controller. The PSO method is employed to tune Kp and KI in the PI controller, and the coefficient of reference current and stator current. The practical topology of matrix converter has been improved by using only 9 semiconductor switches and 18 diodes. A Z-source network has been placed at virtual DC-link in order to boost up the voltage transfer ratio with the least number of passive elements. By applying any changes in reference current or frequency, the modulation index can be automatically adjusted and

respond to changes without additional optimization or high computational requirements in the system.

The merging above parts can bring the system a step forward to industries such aerospace. Since those advantage are the novelties of this research, which help us to have a simple, yet very cost effective and efficient system that can meet the requirements for industry. The concentration of this research is on reducing the torque ripple of IM, having a compact, light system with ability to meet the standards for industrial use with no extensive computing time. The promising simulation and experimental results have been presented to valide the proposed method.

ABSTRAK

Pada peringkat pertama kajian ini adalah kajian secara mendalam analisis daripada strategi pensuisan yang baru untuk penukar matriks (MC) kawalan berpusat tork secara langsung (DTC) bagi pemacu motor aruhan (IM). Paradigma beralih yang dicadangkan menggunakan dua belas sektor 30° untuk kedua-dua vektor fluks dan voltan. Ungkapan analisis kadar perubahan tork dan fluks untuk IM sebagai fungsi vektor voltan MC ini diperolehi. Pengaruh vektor MC voltan pada fluks pemegun dan variasi tork elektromagnet diteliti dan ditambah skim pensuisan bebas daripada sebarang beban dan kelajuan perubahan dibangunkan. Untuk mengurangkan kerugian penukaran MC, kadar pensuisan optimum dipilih melalui pendiskretan dengan purata pada variasi fluks. Prestasi strategi penukaran yang dicadangkan disokong dengan keadaan bersyarat, dan juga skim pensuisan perbandingan heksagon sempadan konvensional. Kaedah yang dicadangkan mempunyai ciri-ciri riak tork rendah, putaran untuk penyelarasan transformasi tidak diperlukan dan frekuensi pensuisan juga dikurangkan. Keputusan mengesahkan bahawa darjah kebebasan untuk memilih kenaikan voltan yang betul, dan tork riak dapat dikurangankan sehingga 60% jika dibandingkan dengan kaedah DTC standard.

Fasa kedua kajian ini menggambarkan IM diberi masukan oleh Ultra penyedia sumber-Z Matrix Penukar (USZSMC) di bawah kadar normal 40% daripada voltan input, yang mengurangkan arus keluaran THD dengan menggunakan kaedah pintar dalam Zarah Swarm Optimization (PSO) pengawal PI. Topologi praktikal matriks penukar telah ditambah baik dengan hanya menggunakan 9 suis semikonduktor dan 18 diod. Rangkaian sumber-Z telah diletakkan di rangkaian maya DC untuk meningkatkan nisbah pemindahan voltan dengan unsur pasif paling minima. Dengan menggunakan sebarang perubahan dalam arus rujukan atau frekuensi, indeks modulasi boleh dilaraskan secara

automatik dan bertindak balas kepada perubahan tanpa pengoptimuman tambahan atau keperluan sistem komputer yang canggih.

Penggabungan bahagian-bahagian yang dinyatakan boleh membawa sistem dalam industri aeroangkasa satu langkah ke hadapan. Kelebihan implementasi penyelidikan ini membantu untuk mempunyai sistem yang berkesan, cekap serta mudah, dengan kos yang dapat memenuhi keperluan industri. Penumpuan kajian ini adalah untuk mengurangkan riak tork IM, padat, sistem yang lebih ringkas dengan keupayaan untuk memenuhi standard kegunaan industri tanpa masa perkomputeran yang lama. Simulasi dan keputusan eksperimen yang dibentangkan membuktikan kesahihan kaedah yang dicadangkan.

ACKNOWLEDGEMENTS

I would like to express my deepest appreciation to all those who provided me the possibility to complete this research. A special gratitude I dedicate to my supervisor, **Prof. Saad Mekhilef**. His contribution in motivating suggestions and encouragement helped me to coordinate my target to accomplish this project.

I would take this opportunity to appreciate the guidance, comment and advice given by other fellows as well as the esteemed examiners, which have improved the quality level of this study. Therefore, my warmest acknowledge goes to them for their crucial roles as follows,

Prof. Hirofumi Akagi *(Tokyo Institute of Technology, Japan)* ➔ for his consultant in the experimental setup and technical points for publishing

Prof. Andrzej M. Trzynadlowski *(University of Nevada, USA)* ➔ for his considerable comments in the first phase of this research

Prof. Mutsuo Nakaoka *(Kyungnam University, Japan)* ➔ for his guidance in the theoretical approach and industrialization

Associate Prof. Ahmad Radan *(K.N. Toosi University of Technology, Iran)* ➔ for his consultant in the organization of this project

Prof. Tsorng-Juu Liang *(National Cheng Kung University, Taiwan)* ➔ for his advices to choice the title and publication guidance

Prof. Carlo Cecati *(Università degli Studi dell'Aquila, Italy)* ➔ for his valued comments in the second phase of this study

Another appreciation should be presented to my colleagues at Power Electronics and Renewable Energy Research Laboratory (PEARL), especially, **Md. Didarul Islam**, **Leong Wen Chek**, **Hazrul Bin M. Basri**, **Kafeel A. Kalwar** and **Tofael Ahmed**. Your commitment to excellence has inspired me all the times.

To

My Family

You do not choose your family.

They are God's gift to you, as you are to them.

TABLE OF CONTENTS

LIST OF FIGURES

LIST OF TABLES

LIST OF SYMBOLS AND ABBREVIATIONS

T_e^*	Torque command
$\vec{V}_s$	Stator-voltage space vector
$\vec{\psi}_s$	Stator-flux vector
$\vec{\psi}_r$	Rotor-flux vector
$\hat{\psi}_s^*$	Stator-flux command
$\overrightarrow{\Delta\psi_s}$	Stator-flux vector variation
$\Delta\lvert\vec{\psi}_s\rvert_{pu}$	Stator flux variation in per unit
ϕ_u	Voltage phase-shift
$\Delta\phi_u$	Phase-shift difference of voltage
C	Capacitor of z-source network
c_1	Cognitive parameter in PSO
c_2	Social parameter in PSO
C_f	Capacitor of input filter
CSI	Current source inverters
CSR	Current source rectifier
H_{Te}	Torque hysteresis output controller
H_φ	Flux hysteresis output controller
I	Output current of inverter
i_1	The fundamental frequency component of the output current
IM	Induction motor
IMC	Indirect matrix converter
i_n	*RMS* current of nth harmonic
I_{ref}	Reference point of current

J	Friction factor
K	Flux vector sector number
k	*a-b-c* phase sequence of a three-phase ac power source,
k_1 & k_2	Flux and torque variation coefficient, respectively
k_T	Constant value
L	Voltage vector sector number
L	Inductor of z-source network
L_f	Inductor of input filter
L_m	Mutual inductance
L_r	Rotor leakage inductance
L_s	Stator leakage inductance
MC	Matrix converter
P	Number of poles
P_g	Best global particle position in PSO
P_i	Best individual particle position in PSO
PSO	Particle swarm optimization
r_1	Random number
r_2	Random number
R_f	Resistance of input filter
R'_r	Rotor resistance
R_s	Stator resistance
S	Complex frequency domain
S_k	Switching states
t_0	Initial time
T_0	Shoot-through switching period
T_1	Non-shoot-through switching period

T_e	Electromagnetic torque of the induction machines
$T_{e,\,base}$	Rated torque
U_c	Voltage of capacitor in z-source network
U_{dc}	Dc-link voltage
U_i	Output voltage of z-source network
U_L	Voltage of inductor in z-source network
U_o	Output line-to-line voltage
USZSMC	Ultra sparse z-source matrix converter
v_{+1} & v_{-1}	Voltage vector first order in $(+)_{ve}$ and $(-)_{ve}$ regions, respectively
V^i_k	Inertia
V_m	Rated voltage
VSI	Voltage source inverter
V_{sm1}	Minimum vector voltage for conventional (60°) scheme
V_{sm2}	Minimum voltage vector for proposed (30°) scheme
V_{sr} & V_{st}	Radial and tangential components of stator-voltage space vector
$V_{s\alpha}$ & $V_{s\beta}$	A and βcomponents of stator voltage, respectively
w	Inertia weight
X'_{lr}	Rotor reactance
X_{ls}	Stator reactance
X_m	Mutual reactance
Z	Equivalent load of connected im in rated conditions
α & β	Real and imaginary components of the transformation from 3-phase stationary coordinate system to the 2-phase coordinate system

γ	Load angle
γ_1	Angle between stator and rotor-flux vectors
Δt	Time interval
ΔT_e	Variation of electromagnetic torque
$\Delta T_{e,\,pu}$	Torque variation in per unit
$\Delta\gamma$	Variation of load angle
$\Delta\zeta$	Variation of rotor-flux vector angle
$\Delta\theta$	Variation of stator-flux vector angle
θ	Angle of stator-flux vector
σ	Leakage factor
ψ_m	Maximum flux of stator
ω_s	Synchronous speed
VVVF	Variable voltage variable frequency

Note: all the motor parameters are referred to stator side.

LIST OF APPENDICES

CHAPTER 1: INTRODUTION

1.1 Power Electronics

Power electronics is an industrial science based on the combination of control, electronics and energy systems. The outcomes of the power electronics industry enable to convert the energy between source and load. The power conversion is a necessary task with the purpose of providing the precise and energy efficient operation in the industrial and household appliances. Meanwhile, the generated power and frequency, as the source, are not apocopate for the various demands of voltage, current and frequency in the load side. Figure 1-1 shows the integration of controller and converter as a power electronics interface.

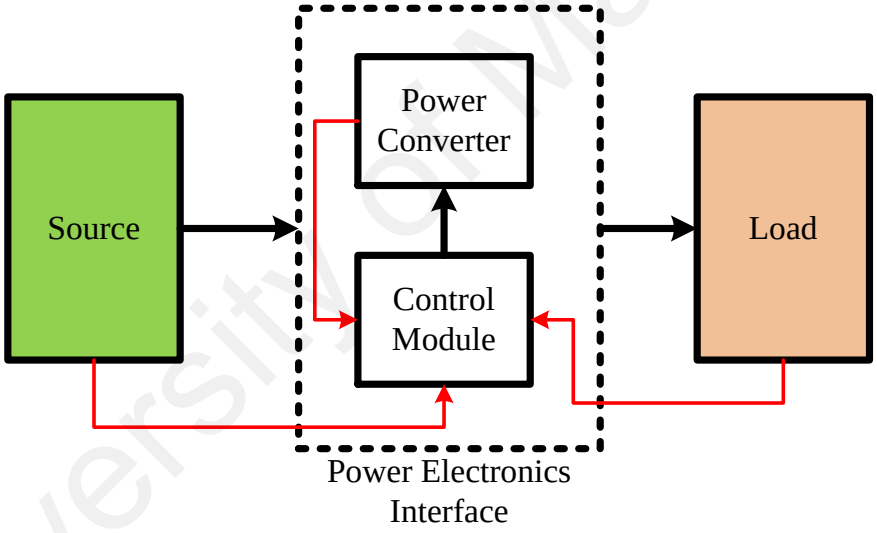

Figure 1-1: The interface of power electronics from source to load

A power converter consists magnetic transformer, energy storage components, and semiconductor devices, which can carry out the high power. On the other hand, the controller consists the low-power analog and/or digital elements, which controls the switching devise in the power converter part. Normally, the control algorithm is according to a special driving plan, which considers the response characteristics and stability of total system.

The improvement of power semiconductor devices with high power capabilities has a great effect on the enhancement trend of power electronics. With advent of thyristor or

silicon-controlled rectifier (SCR) in 1956 by Bell laboratory, which was commercialized in 1958 by General Electric, a new window to the modern power electronics was opened. The trend of development in this field has been recently changed from device-driven-based to application-driven-based (Rashid, 2010). This change makes the power electronics more practical in more electrical applications such as industrial, commercial and residential environment, and transportation, communication, military and aerospace industries.

The power conversion is categorized into four types, according to the input and output characteristics:

1. AC-DC: is known as rectifiers to convert an AC input voltage to a controllable DC voltage.
2. DC-DC: to convert a DC input voltage with no regulation to a controlled variable DC output voltage. The DC-DC converters are classified as shown in Figure 1-2. In this subclass, existing the transformer is an important issue to classify the fly-back and forward types.

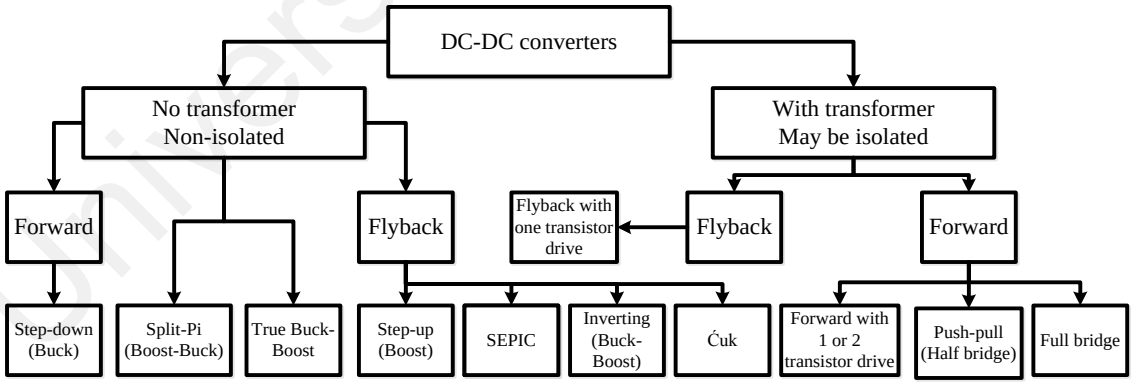

Figure 1-2: DC-DC classification

3. DC-AC: is recognized as inverters. The characteristic feature of this converter is to generate controllable AC output waveforms from a DC power supply, which can be modified in terms of frequency, magnitude and phase

4. AC-AC: to convert an AC input voltage to a regulated AC voltage with variable amplitude and frequency.

1.2 AC–AC Power Converters

AC–AC converters normally use for converting the frequency and magnitude. The overall topologies of them can be categorized in three classes, depending upon the type of AC–AC conversion. The diagram of classification for frequency converters is depicted in Figure 1-3. The AC–AC frequency converters are different in details especially in the technical functionality. Moreover, the improvement in the topology of the converters is yet in progress (Dalla Vecchia, Brunelli Lazzarin, & Barbi, 2015; Jothibasu & Mishra, 2015; Yao et al., 2015). The current classify is including the direct topologies without DC energy storage components, the indirect constructions with the energy storage elements at DC-link, and hybrid configurations. The hybrid configurations have smaller DC energy storage components as compare with previous categories.

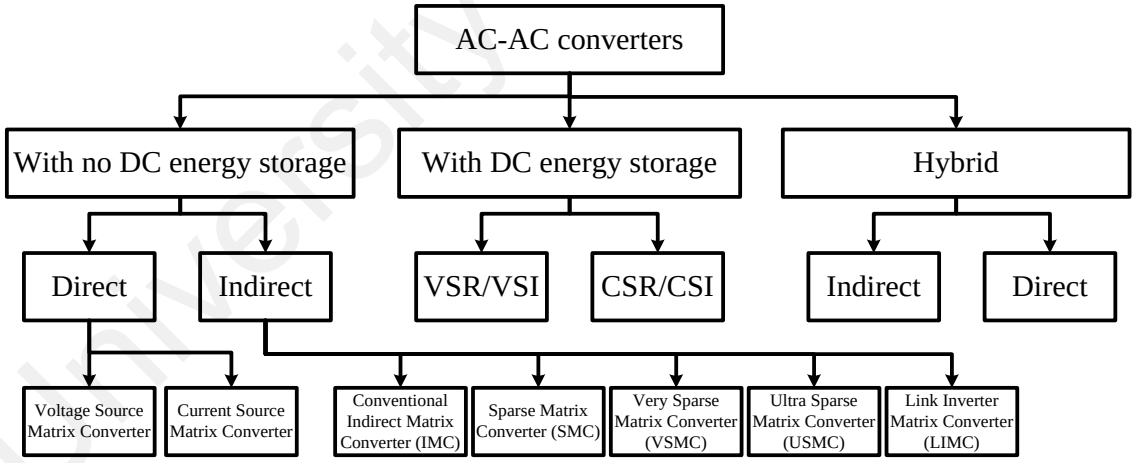

Figure 1-3: The category of AC-AC converters

The direct and indirect AC-AC converters with no DC energy storage components consist the Matrix converter (MC) family. They include of an array of static power semiconductor switches linked between the load terminal and connected grid supply. The voltage and current source matrix converters are the subset of direct topologies of this group. The second category includes the most prevalent and extensively used in industry.

The voltage source inverters (VSI) and current source inverters (CSI) are directly able to convert the frequency and magnitude. The combination of above-mentioned categories, open a new chapter in AC-AC converters, which have a small-sized DC energy storage. Normally, this group has a DC–DC boost converter at the virtual DC-link.

1.3 Motivations of Research

The new generation of unconventional AC-AC converters have rarely applied into the high-performance industries. Normally, they have poor ability to tolerate the critical conditions. Accordingly, the elimination of defects and enhancing the performance can carry them a step forward to industry.

The first advantage of the current study is developing the switching strategy for MC to drive induction motor (IM) for reduction of torque ripple while the converter is connected to an ideal input voltage and balanced load. Meanwhile, the unbalanced voltage source could affect the control system of MC Merging the reduction of torque ripple based on 12-sector space vector switching for direct torque control (DTC) of IM as first motivation of this research with applying on ultra-sparse MC under the abnormal condition is a novel idea, which can lead the matrix converter family step forward to the reliable industry, especially into the aerospace manufacturing.

1.4 Problem Statements

Currently, the MC family is utilized as a laboratory AC/AC driver with almost no reliable potential for industry (Andreu et al., 2012) because of:

1. Complexity in control (Niaki, Iravani, & Kojori, 2014; Snary, Bhangu, Bingham, Stone, & Schofield, 2005),
2. Sensitivity in face to the abnormal input (D. Casadei, Serra, & Tani, 1998; Chen & Yao, 2006; Weizhang et al., 2013),

3. Limitation of voltage transfer ratio up to 86.6% (Karaman, Farasat, & Trzynadlowski, 2014; Weizhang et al., 2013),
4. Proliferation of semiconductor switches (Aten et al., 2006; Zhaoyang, Minli, Chunjiang, & Weiyang, 2012).
5. Direct matrix converter (DMC) has flow power path in bidirectional mode for transmitting the power whether from grid to the consumer or in generative mode can be reverse (Karaman et al., 2014). However, the bidirectional capability is an advantage for many various applications (Weerasinghe, Thrimawithana, & Madawala, 2014); in aerospace industry the power flow must be in one direction (Kiwoo, Eun-Sil, & Kyo-Beum, 2010; Wheeler et al., 2006; Xiaoyan, Goodman, Gerada, Youtong, & Qinfen, 2012). and
6. The excess number of switches for DMC has increased the weight of whole prototype (Xiaoyan et al., 2012) which is ineligible for aerospace manufacturing, nevertheless, eliminating the bulky DC-like is an inherent specification of MC (Empringham, Kolar, Rodriguez, Wheeler, & Clare, 2013)

The above-mentioned weaknesses are the most considerable obstacles to accept the MC family as an industrial converter by manufacturers. Therefore, this study focuses to prepare a simple and practical control algorithm, tolerant system under high abnormality main, unity voltage transfer ratio, and, a compact and light system with ability to meet the standards for industrial use with no extensive computing time.

1.5 Research Objectives

A switching strategy is required to take advantage of the ultra-sparse Z-source matrix converter (USZSMC) base on DTC, which can reduce the torque ripple of IM. Simultaneously, this method should drive the motor under abnormal input voltage, while

it compensates the voltage transfer ratio up to unity. Therefore, the objectives of this study are as follows,

I. To implement twelve 30°sectors of voltage vector scheme in DTC control in order to reduce the torque ripple and increase the performance of system.

II. To design a converter that works under abnormal input voltage.

III. To compensate the voltage transfer ratio up to unity through the applied Z-source network.

IV. To employ particle swarm optimization (PSO) in order to optimize the PI controller parameters to reduce the THD of stator current.

1.6 Thesis Outlines

In this study, a profound survey on the earlier investigates is presented in chapter 2. Furthermore, the fundamental of switching algorithms and control strategy are provided in the affiliated subject. The methodology of proposed system is illustrated in chapter 3, which is distinct in three segments. Primarily, a novel switching strategy in Space Vector Modulation (SVM) is developed based on twelve 30° sectors for the circular locus of increase the degrees of freedom in selecting voltage and flux vectors. Second, under abnormal input voltage, the integrated metaheuristic algorithm (PSO) is employed to find the optimum values of PI and the coefficient of references, load current and modulation index in a single multimodal problem. As a final point, the switching strategy of first stage is considered for the topology and input condition of second stage to reduce the torque ripple of induction motor, while it functions under abnormal input voltage and compensates the stator voltage to 100% of the grid voltage.

Chapter 4 addresses the simulation and experimental results. This chapter discusses about the findings of the proposed study and comparing to other aligned researches.

In chapter 5, the conclusions of project and its recommendations for further researches are summarized.

CHAPTER 2: LITERATURE REVIEW

In this chapter, the background of the study is divided into two sub-sections including topology and control algorithm. The practical topologies of MC are attentively presented in 2.2. The feasible strategies to control an MC are profoundly discussed in 2.4. Therefore, according to the objectives of the study, the standard direct torque control method is comprehensively reviewed in order to drive an induction motor.

2.1 Background of Study

The rectifier and inverter have been integrated as a unique AC/AC converter by J.C. Read in 1945 (Read, 1945). In 1995, this research was expanded to enhance the synchronization of switching inverter, and the suppress voltage emissions, which greatly improved the DC-AC part of the converter (Kates, 1995). The suggested topology of J.C. Read with insulated-gate bipolar transistor and control algorithm developed by Kates has been introduced for the demand market of power converters.

Dewan, and Rosenberg, have presented a theoretical analysis of pulse width control in three-phase pulse width-modulated inverters in 1970. In their study, clamped commutation and independent commutations have been compared to the number of commutations per cycle and the effect of load conditions on the output-voltage waveforms (Dewan & Rosenberg, 1970). Later, Erik Persson enhanced the efficiency of Dewan's work. In particular, the pulse width modulated (PWM) inverter output amplitudes and rise times were investigated (Persson, 1992).

By modifying the Persson's theory, it was applicable to obtain the unity input displacement and sinusoidal input and output current waveforms, which presented by Kaufman few years later. (Kaufman, 1995). The outcome of PWM control method for the forced commutated cyclo-converters, which was suggested by them, is as follows:

1) A decrease in the switching frequency and an increase in the input-to-output voltage ratio can be achieved when the two-phase switching method is used. The control functions that were suggested consist of the standard type for the time when the input displacement factor is unity.
2) Asymmetrical and/or harmonic distortion input source voltages are compensated.

According to above-mentioned researchers' efforts, the power electronics industry starts a new age of development. It means the efficiency improvement of the converters is not only an appreciative of the topology developments, but also the perfection of control systems, which have a significant effect on enhancement of the performance.

2.2 The Topology of Matrix Converters

The topology of matrix converters is divided into two main categories as shown in Figure 2-1. The direct topology of MC includes voltage and current source MCs, while the indirect matrix converter has four various prototypes. The conventional IMC is an equivalent circuit of direct matrix converter but the sparse, very sparse and ultra-sparse topologies have some dissimilarities that will be discussed in next sections.

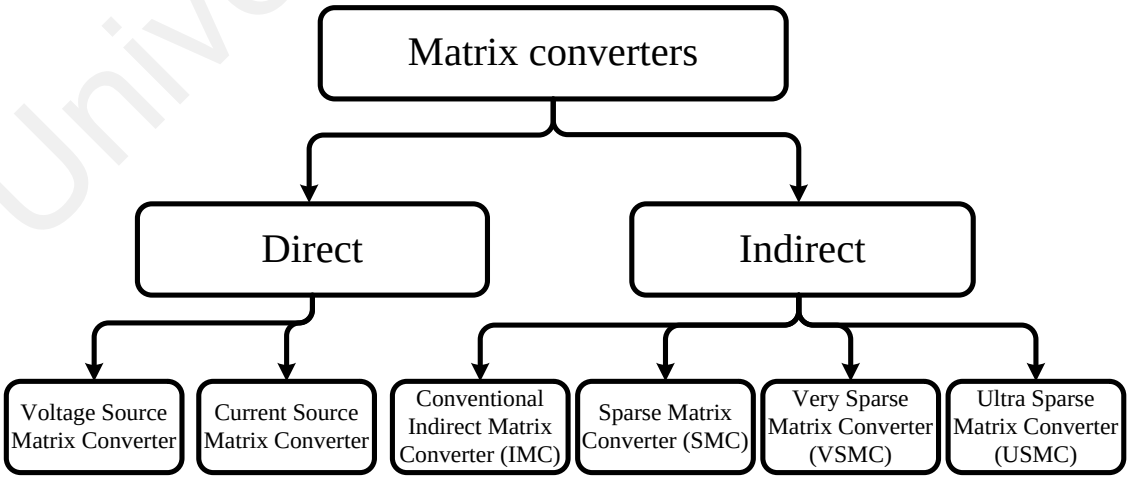

Figure 2-1: The classification of matrix converter based on topology

2.2.1 Direct Matrix Converter (DMC)

The earlier research presented the unlimited frequency changers using thyristors, which needed to implement the bidirectional controlled switch for external commutation circuits. This commutation is mandatory and unavoidable. The former power circuits were massive and the performance of them was poor (Stacey, 1976). The introduction of the bidirectional switches as power transistors made the matrix converter topology more interesting (Chattopadhyay, 1976).

The actual progress to incorporate the rectification and inversion parts as DMC has been introduced by Venturini and Alesina in1980. They presented a circuit of a power converter with matrix property. In this topology, the output and input voltage and current have been defined as a 3×1 matrix, and simultaneously, the transfer-matrix is 3×3. The output voltage has direct relation with the input voltage and transfer-matrix while, the output current has indirect dependency to input current because of transposed transfer-matrix. As can be seen in Figure 2-2, the semiconductor switches in topology are bidirectional, which includes the common emitter, collector in back-to-back configuration, and switch cell with Diode-Bridge.

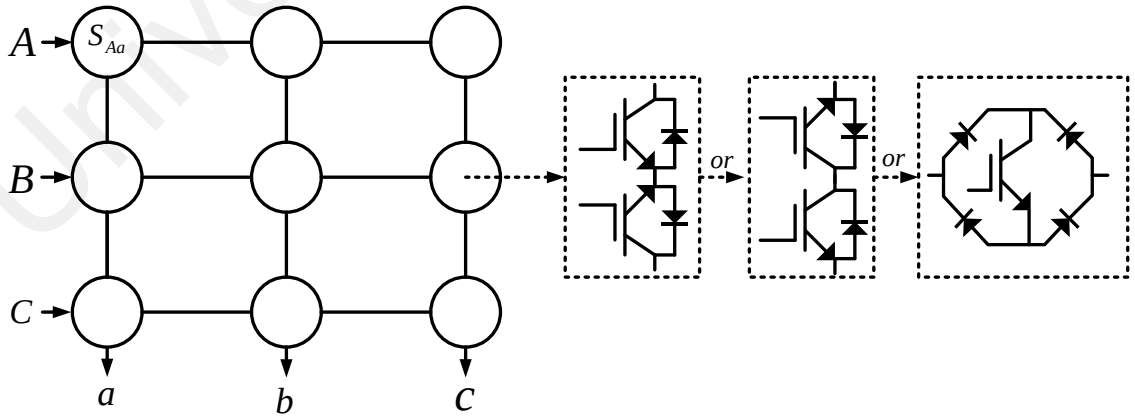

Figure 2-2: Direct matrix converter prototype

For each four-quadrant switch, the combination of two anti-parallel diodes and two IGBTs prepares a particular turn-on of the switch to be selected in each current direction.

Hence, this combination is quite essential to have a safe multi-step commutation approach(P. W. Wheeler, J. Rodriguez, J. C. Clare, L. Empringham, & A. Weinstein, 2002).. The short-circuiting in or an abrupt interruption of an output phase current can be avoided By applying this prototype to combine the IGBTs and diodes

According to a three-phase AC motor drive applications, the input voltages and output currents of converter are supposed to be impressed by modulation schemes for the DMC and these can be classified into direct and indirect schemes for converting the magnitude and frequency(Alesina & Venturini, 1989; Ishiguro, Furuhashi, & Okuma, 1991).

2.2.2 Indirect Matrix Converter Topology

The topology of direct matrix converter can be disintegrated into two independent part of rectification and inversion as depicted in Figure 2-3. The disintegrated circuit enables to keep all the specifications of DMC. Moreover, in indirect matrix converter (IMC) topologies, the virtual DC-link is accessible, while it was unreachable (Huber & Borojevic, 1995; Ziogas, Khan, & Rashid, 1986). Therefore, the indirect categories are recommended for the applications that require accessing the DC-link.

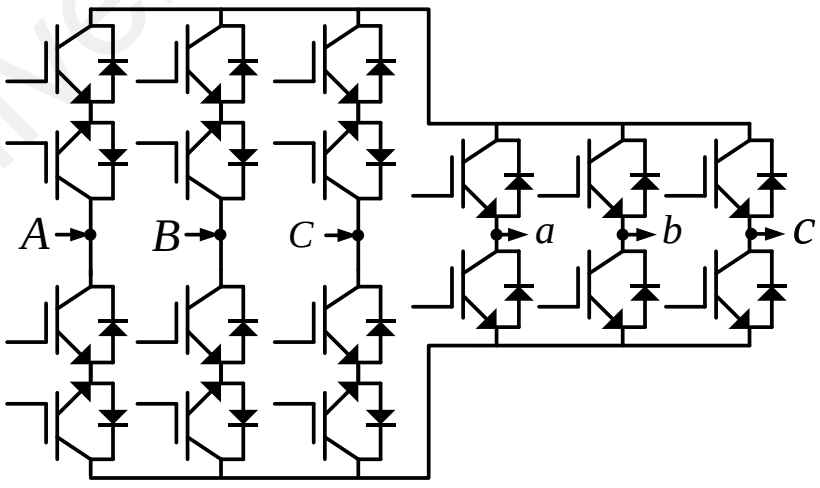

Figure 2-3: The indirect matrix converter with common-emitter configuration

The DMC is divided into a rectifier, as the input stage with voltage-fed, and, the inversion part with influenced output currents. However, the DC-link is not accessible

but the virtual stages of DMC are directly coupled with the DC level (Iimori, Shinohara, Tarumi, Zixum, & Muroya, 1997).

A four-quadrant switch and current source rectifier, feeds a traditional voltage source inverter (two-quadrant switch) which is able to operate with a positive and negative DC current for a unipolar DC-link voltage as required by the inverter stage. The input capacitor of the inverter is sufficiently effected by the AC voltage of grid side, filter capacitors of the rectifier stage. The output inductor of the rectifier is adequately effected by the current influencing inductance of the load (J. W. Kolar, T. Friedli, J. Rodriguez, & P. W. Wheeler, 2011).

Having a fixed polarity is an essential requirement for the DC-link voltage of the IMC.The IMC four-quadrant switch (current source rectifier) is capable of operating with both positive and negative DC-link voltage polarities.

2.2.3 Sparse Matrix Converter

Owing to plethora of the semiconductor switches in the direct and indirect MC, this convertor was not able to satisfy the expectations of manufacturer, specially, where the weight and volume of the converter are considerable. Thus, a new sparse topology has been introduced in (J. W. Kolar, F. Schafmeister, S. D. Round, & H. Ertl, 2007b). As ~~can be~~ shown in Figure 2-4, the sparse matrix converter has nine semiconductor switches in the rectification part, with the same number of diode in main topology of IMC.

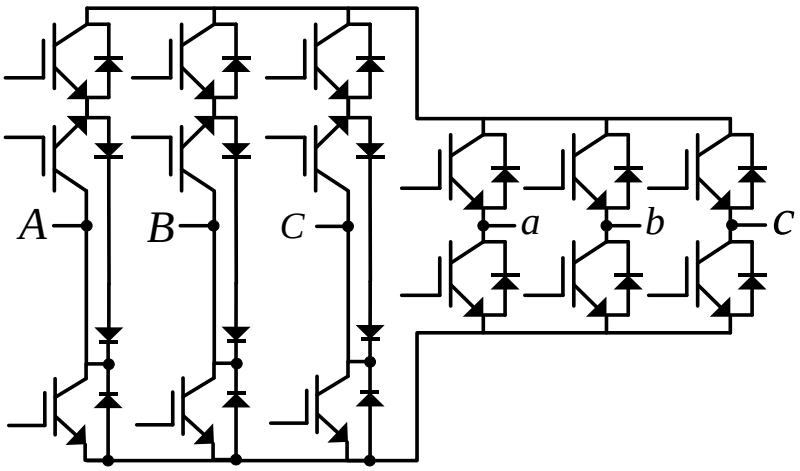

Figure 2-4: Sparse matrix converter topology

Compared to the DMC, the sparse topology provides equal performance, but with a diminished number of semiconductor switches and the choice of using an enhanced structure of zero current commutation for DC-link, which brings lower complexity in control, more safety and advanced reliability. In other words, based on functionality resemblance of the DMC and SMC, the line-to-line input phase currents and output voltages resulting are compiled for the different switching state combinations. The ability of control and the operation range of the SMC are not limited, notwithstanding the reduced number of unipolar turn-off power semiconductors and as a result; the SMC signifies a very reasonable alternative to the DMC/IMC for industrial demands.

2.2.4 Very-Sparse Matrix Converter

However, the sparse matrix converter has eliminated three semiconductor switches from the rectification part; the topology has still too many IGBT/MOSFET. Therefore, the new prototype has been presented as a very-sparse matrix converter (VSMC) (F Schafmeister, Rytz, & Kolar, 2005). As can be seen in Figure 2-5, VSMC has only six controllable semiconductor switches but 24 diodes in rectifier.

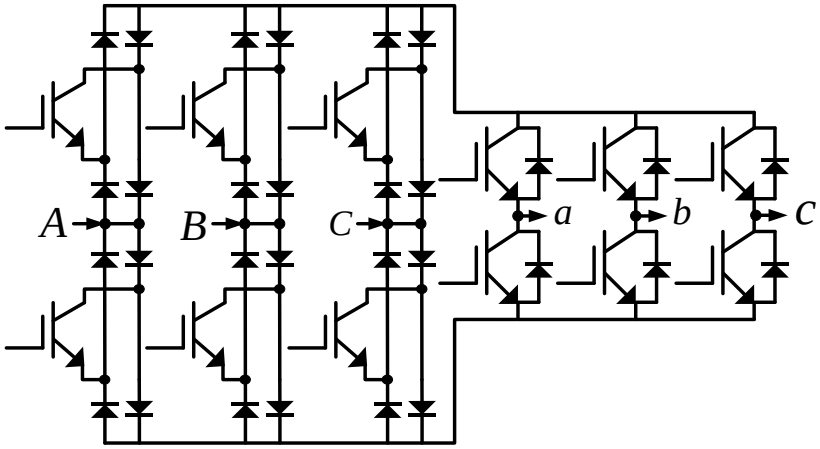

Figure 2-5: Very sparse matrix converter topology

Compared with the SMC, there are fewer number of semiconductor switches, while the conduction losses are immense because of the increment in the number of diodes in the power transmission. Compared to the normal back-to-back converters, with six power switches and anti-parallel diodes, the VSMC has 12 more diodes. Therefore, according to the both comparisons, the specification of this topology has no reliable or economic justification (F Schafmeister et al., 2005).

2.2.5 Ultra-Sparse Matrix Converter

The Ultra-Sparse Matrix Converter (USMC) is an indirect matrix converter with a low-complexity modulation scheme compared with the conventional IMC. It only requires nine semiconductor switches, three switches in the rectification part and the remaining six switches in the inversion part. The USMC is separated into input and output stages to avoid the complex multi-step commutation method of the conventional matrix converter. It uses a simple zero-current commutation DC-link scheme to reduce the switching losses of the rectifier stage (Schönberger, Friedli, Round, & Kolar, 2007).

Although, the previous research has reduced the number of semiconductors; the indirect matrix converter still had many components in its topology. This fact was the main momentum of creating the Ultra-Sparse Matrix Converter (USMC). In the category

of IMCs, the ultra-sparse topology not only has less number of switches and diodes but also the power direction is unidirectional, which is demanded by various application such as aerospace industry (Kolar, Baumann, Schafmeister, & Ertl, 2002; Schönberger et al., 2007). Figure 2-6 illustrates the configuration of semiconductors as the topology of USMC and which is the most compact prototype in category of MC family.

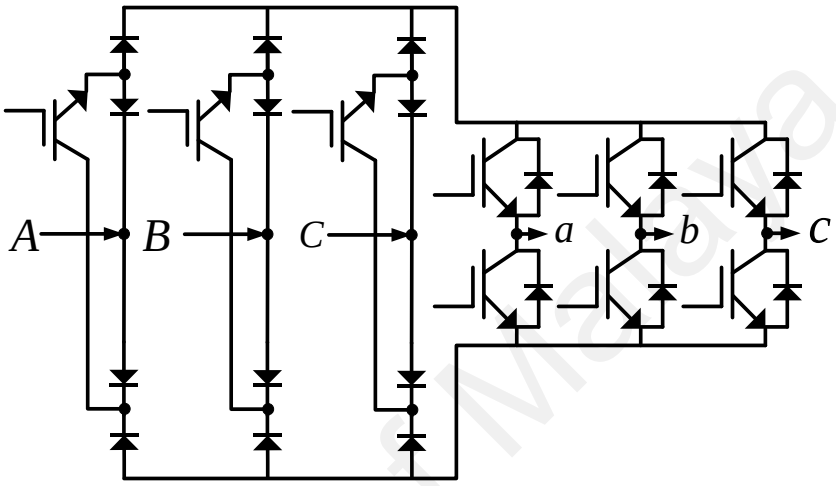

Figure 2-6: Ultra-Sparse matrix converter topology

2.2.5.1 Ultra Sparse Rectification Stage Topology

The three-phase ultra-sparse rectifier employs only 3 IGBTs and 12 diodes, as shown in Figure 2-7.

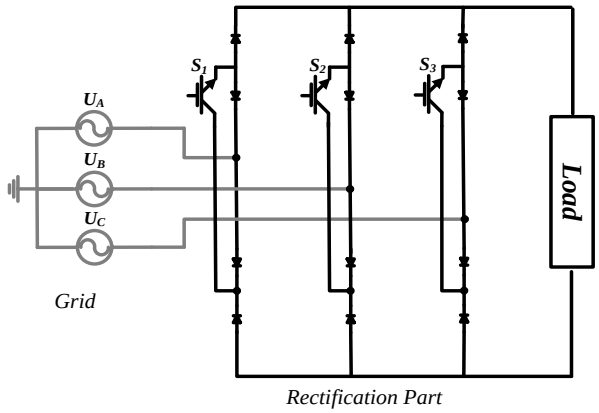

Figure 2-7: Ultra sparse rectifier

The simple controlling method for the rectifier is simple due to having only three active switches; and the probability of facing short circuit or failure is less because of the

absence of three semiconductor switches at the lower part of each legs. As one of the limitations faced by the back-to-back converter is its sensitivity toward electromagnetic interference and other sources of noises that can accidentally turn-on two switches from the same phase-leg, causing a short-circuit fault in turn. Dead-time protection and its associated volt-second error are, therefore, unavoidable for the back-to-back converter.

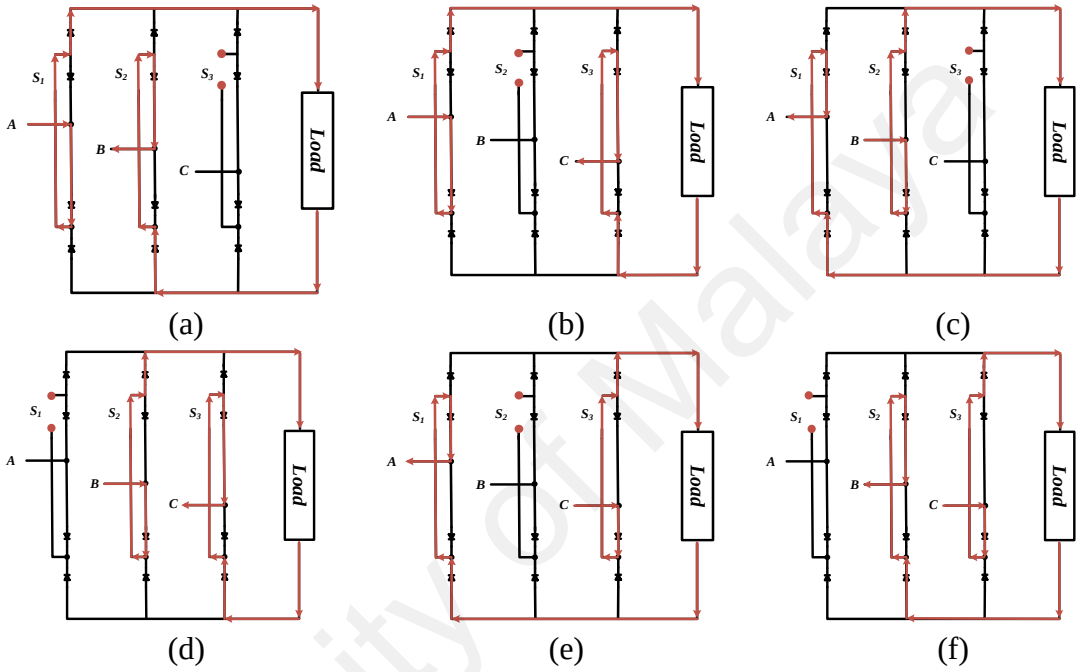

Figure 2-8: The six possible power flows in the ultra-sparse rectifier

Table 2-1 shows the operation of the sparse rectifier in the six maintained states as follows:

Table 2-1: The switching scheme of the ultra-sparse rectifier

State No.	S_1	power flow through S_1	S_2	power flow through S_2	S_3	power flow through S_3
1	ON	IN	ON	OUT	OFF	NULL
2	ON	IN	OFF	NULL	ON	OUT
3	ON	OUT	ON	IN	OFF	NULL
4	OFF	NULL	ON	IN	ON	OUT
5	ON	OUT	OFF	NULL	ON	IN
6	OFF	NULL	ON	OUT	ON	IN

The six different operation modes of the rectifier system are shown in Figure 2-8. In Figure 2-8(a) input phase A is at its peak positive value and is clamped to the positive DC-link rail by input switch S_1. The switch S_2 is also turned on to conduct the return

current. During this interval output leg S_1 has its high side switch active while the other output switches have their low side switches active. Figure 2-8(b) shows that the S_1 is conducting A and S_3 plays the role of S_2 in the previous stage while the S_2 is open. In Figure 2-8(c), S_2 has the same duty of S_1 in the first stage to lead the power into the rectifier where the energy aims to return through S_1 while S_3 is off. In Figure 2-8(d), S_2 brings the power in and S_3 returns whereas S_1 is open. The S_3 leads the power into the rectifier and S_1 drives it out via phase A while S_2 is off as can be seen in Figure 2-8(e). Figure 2-8(f) shows that S_3 plays the same role of previous stage while the S_1 and S_2 interchange their task.

2.3 Z-source Network in Matrix Converters

The Z-source network is normally known as a DC-DC booster. This converter is mostly implemented in the DC-link of AC/DC/AC converters to boost up the voltage transfer ratio.

In (Peng, 2003; Peng, Shen, & Qian, 2005), an associated comparison for DC/AC inverters has been presented in which a DC-DC boost converter is placed instead of a series diode before connecting to the VSI at the end of the rectification part in the IMC. A similar substitution of entrance diode of ZSI has been expressed in (Dehghan, Mohamadian, Yazdian, & Ashrafzadeh, 2010; Pan, 2014; Zhu, Yu, & Luo, 2010) with the constant DC voltage source instead of the rectification part. A prior series diode is essential, unless the rectifier diodes are fast recovery ones. Therefore, the alternative topology can provide the same functionality in the tail-end CSR, which is a cost effective saving of a diode (Changliang & Xinmin, 2015; Pan, 2014).

The Z-source can be placed by two configurations which include the series and cascaded categories. As can be seen in Figure 2-9(a), the series Z-source has an extra diode in compared to the cascaded Z-source network. Therefore, when the weight and

volume of system is concerned, the cascaded configurations are preferred than series ones (Karaman et al., 2014).

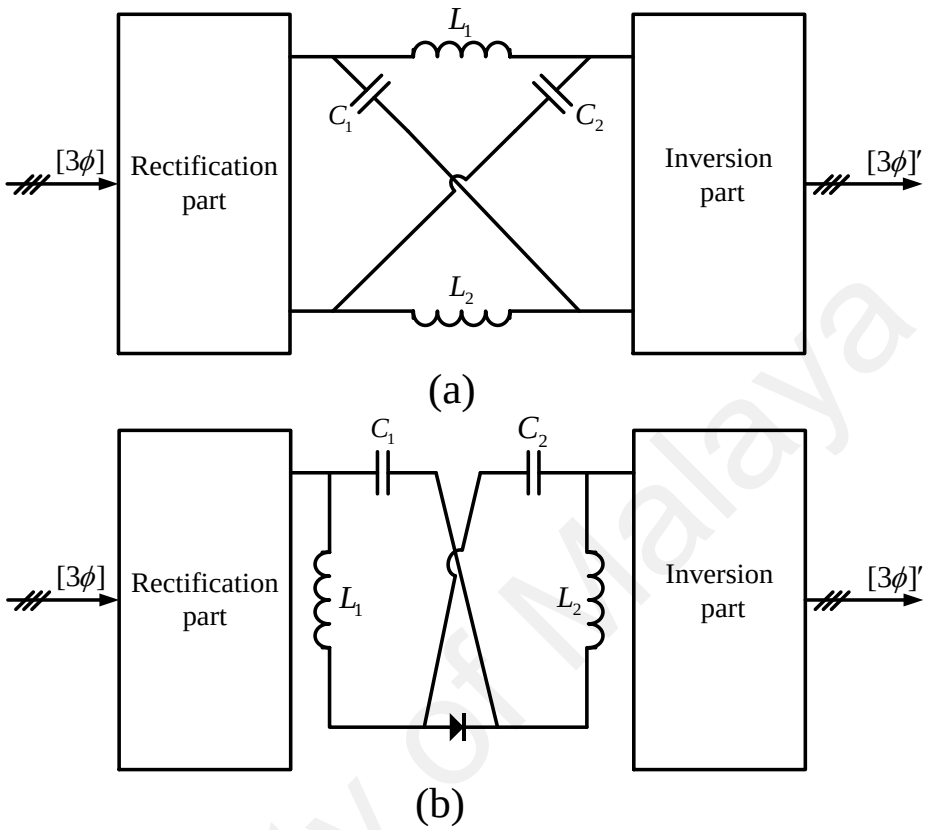

Figure 2-9: configuration of Z-source network: (a) cascaded. (b) series.

2.3.1 Comparison of MC Topologies

While, the various research chiefly concern DMCs, an indirect matrix converter can be considered as an option for the DMC (M. Y. Lee, Wheeler, & Klumpner, 2010; Metidji, Taib, Baghli, Rekioua, & Bacha, 2013). Still, the main circuit of the IMC has drawbacks compared to the DMC, eg. power losses (Faraji, Aghasi, Khaburi, & Ghorbani, 2011) of the IMC are larger with most loading situations. In addition, its output/input voltage ratio is more non-linear compared to DMC, which reduces its suitability to the speed sensor-less drive of IM (Johann W Kolar, Thomas Friedli, Jose Rodriguez, & Patrick W Wheeler, 2011). One of the biggest difficulties in the operation of this converter was the commutation of the bidirectional switches. This problem has been solved by introducing intelligent and soft commutation techniques, giving new momentum to

research in this area, while with a suitable modulation method there is no need for special commutation of MCs (Patrick W Wheeler, Jose Rodriguez, Jon C Clare, Lee Empringham, & Alejandro Weinstein, 2002).

According to the literature review of the performance of MC topologies, it is essential to select the appropriate topology based on the proposed application. As can be seen in Table 2-2, a comparison has been performed between the members of MC family. It illustrates that reducing the number of semiconductor switches will increase the average value of switching stress.

Table 2-2: Comparison of the various MC topology (J. W. Kolar, F. Schafmeister, S. D. Round, & H. Ertl, 2007a)

Converter Type	Switch	Diode	Isolated Driver Source	Directionality	Average Switching Stress
DMC	18	18	9	Bidirectional	Low
IMC	18	18	8	Bidirectional	Medium
SMC	15	18	7	Bidirectional	Medium
VSMC	12	30	10	Bidirectional	High
USMC	9	18	7	Unidirectional	High

2.4 Control Strategy

The control strategies for matrix converter can be categorized into four sub-classes include of the scalar, PWM, DTC and predictive controls as depicted in Figure 2-10. The methods target to drive an induction machine. More details have been provided in the sub-sections of this chapter.

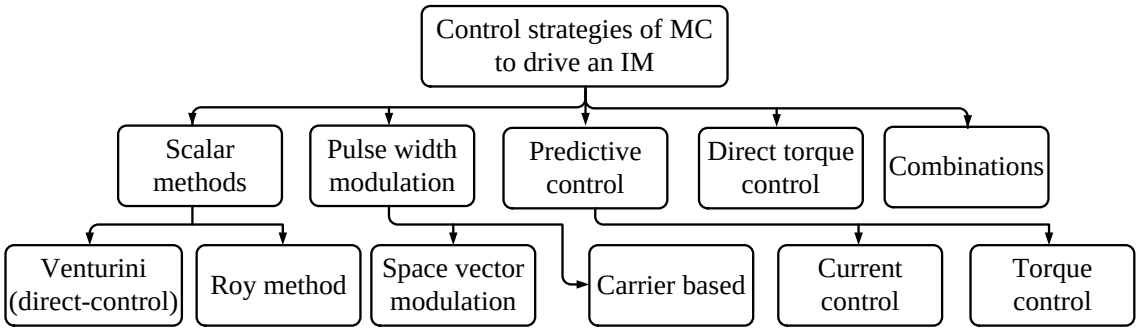

Figure 2-10: Control approaches of MC to drive an IM

2.4.1 The Fundamental of Matrix Converter

The Matrix Converter, which has an array of $m \times n$ bidirectional power switches to connect directly, and m-phase voltage source to an n-phase load, is a single stage converter. Figure 2-11 belongs to a Matrix Converter of 3×3 switches, which owns the broadest functional interest because a three-phase voltage source with a three-phase load; usually, a motor is linked to it. A voltage source caters for the matrix converter, which is why being short-circuited is necessary for the input terminals. Furthermore, an inductive nature is attributed to the load usually and this is the reason why opening an output phase should never be considered. Based on the restrictions put forward above switching function of a single switch can be defined.

$$S_{kj} = \begin{cases} 1; S_{kj} \Leftrightarrow close \\ 0; S_{kj} \Leftrightarrow open \end{cases} \rightarrow k = \{A, \mathrm{B}, \mathrm{C}\}; \mathrm{j} = \{a, \mathrm{b}, \mathrm{c}\} \qquad 2\text{-}1$$

The constraints discussed above can be expressed by:

$$S_{Aj} + S_{Aj} + S_{Aj} = 1 \Leftrightarrow j = \{a, b, c\} \qquad 2\text{-}2$$

With these restrictions, the 3× 3 Matrix Converter has 27 possible switching states are shown in Figure 2-11. The load and source voltages are referenced to the supply neutral, '0' in Figure 2-11, and can be expressed as vectors defined by:

$$U_o = \begin{pmatrix} u_a(t) \\ u_b(t) \\ u_c(t) \end{pmatrix} \Leftrightarrow U_i = \begin{pmatrix} u_A(t) \\ u_B(t) \\ u_C(t) \end{pmatrix} \qquad 2\text{-}3$$

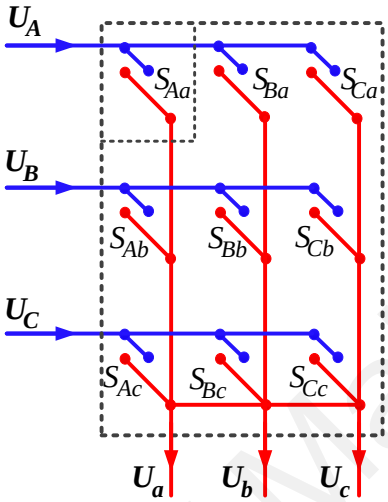

Figure 2-11: Simplified circuit of a 3× 3 Matrix Converter

The relationship between load and input voltages can be expressed as:

$$\begin{pmatrix} U_a(t) \\ U_b(t) \\ U_c(t) \end{pmatrix} = \begin{pmatrix} S_{Aa}(t) & S_{Ba}(t) & S_{Ca}(t) \\ S_{Ab}(t) & S_{Bb}(t) & S_{Cb}(t) \\ S_{Ac}(t) & S_{Bc}(t) & S_{Cc}(t) \end{pmatrix} . \begin{pmatrix} U_A(t) \\ U_B(t) \\ U_C(t) \end{pmatrix} \leftrightarrow U_o = T.U_i \qquad 2\text{-}4$$

where T is the instantaneous transfer matrix.

In the same form, the following relationships are valid for the input and output currents:

$$i_o = \begin{pmatrix} i_a(t) \\ i_b(t) \\ i_c(t) \end{pmatrix} \leftrightarrow i_i = \begin{pmatrix} i_A(t) \\ i_B(t) \\ i_C(t) \end{pmatrix} \qquad 2\text{-}5$$

And also, we have:

$$i_i = T^T . i_o \qquad 2\text{-}6$$

where T^T is the transpose matrix of T.

The immediate connections between input and output quantities are given by 2-4 and 2-6. It is also vital to take into account the switching pattern that is used to derive modulation rules. It usually adheres to a form which resembles the one displayed in Figure 2-12.

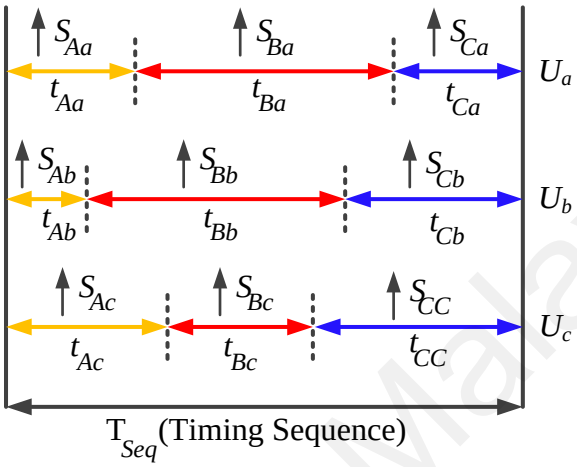

Figure 2-12: General model of timing sequence for Matrix Converter

It is possible to produce a low-frequency output voltage of variable amplitude and frequency by modulating the duty cycle of the switches and performing their respective switching functions, only if we assume that the bidirectional power switches operate with high switching frequency.

Let $m_{Kj}(t)$ be the duty cycle of the switch S_{Kj} defined as $m_{Kj}(t) = {}^{t_{Kj}}/_{T_{seq}}$, that has the following values

$$0 < m_{Kj} < 1 \qquad K = \{A,B,C\} \; ; \; j = \{a,b,c\} \tag{2-7}$$

$$M(t) = \begin{pmatrix} m_{Aa}(t) & m_{Bb}(t) & m_{Ca}(t) \\ m_{Ab}(t) & m_{Bb}(t) & m_{Cb}(t) \\ m_{Ac}(t) & m_{Bc}(t) & m_{Cc}(t) \end{pmatrix} \tag{2-8}$$

The low-frequency component of the output phase voltage is given by

$$U_o(t) = M(t).U_i(t) \tag{2-9}$$

The low-frequency component of the input current is

$$i_i = M^T(t).i_o \qquad 2\text{-}10$$

2.4.2 Basic Modulation Solution

The switching losses associated with the modulation schemes have been considered as a related matter by (Helle, Larsen, Jorgensen, Munk-Nielsen, & Blaabjerg, 2004). Recently, a unique method for evaluating various modulation schemes associated with switching losses was suggested (Huu-Nhan & Hong-Hee, 2016; Siwakoti, Peng, Blaabjerg, Loh, & Town, 2015), which used three-phase to three-phase matrix converters as an appropriate topology. The important characteristics of modulator are considered as the quality of input and output waveform in this approach.

The modulation problem normally considered for the matrix converter can be stated as follows:

Given a set of input voltages and an assumed set of output currents

$$U_i = U_{im}\begin{pmatrix}\cos(\omega_i t)\\ \cos\left(\omega_i t+\frac{2\pi}{3}\right)\\ \cos\left(\omega_i t+\frac{4\pi}{3}\right)\end{pmatrix},\ i_o = I_{om}\begin{pmatrix}\cos(\omega_o t)\\ \cos\left(\omega_o t+\phi+\frac{2\pi}{3}\right)\\ \cos\left(\omega_o t+\phi+\frac{2\pi}{3}\right)\end{pmatrix} \qquad 2\text{-}11$$

find a modulation matrix *M(t)* such that

$$U_o = qU_{im}\begin{pmatrix}\cos(\omega_o t)\\ \cos\left(\omega_o t+\frac{2\pi}{3}\right)\\ \cos\left(\omega_o t+\frac{4\pi}{3}\right)\end{pmatrix},\ i_i = q\cos(\phi)I_{om}\begin{pmatrix}\cos(\omega_i t)\\ \cos\left(\omega_i t+\phi+\frac{2\pi}{3}\right)\\ \cos\left(\omega_i t+\phi+\frac{2\pi}{3}\right)\end{pmatrix} \qquad 2\text{-}12$$

and that the constraint 2-2 is satisfied. In 2-12, *q* is the voltage gain between the output and input voltages.

There are two basic solutions:

$$M_1 = \frac{1}{3}\begin{pmatrix} 1+2q\cos(\omega_m t) & 1+2q\cos(\omega_m t-\frac{2\pi}{3}) & 1+2q\cos(\omega_m t-\frac{4\pi}{3}) \\ 1+2q\cos(\omega_m t-\frac{4\pi}{3}) & 1+2q\cos(\omega_m t) & 1+2q\cos(\omega_m t-\frac{2\pi}{3}) \\ 1+2q\cos(\omega_m t-\frac{2\pi}{3}) & 1+2q\cos(\omega_m t-\frac{4\pi}{3}) & 1+2q\cos(\omega_m t) \end{pmatrix} \quad 2\text{-}13$$

With $\varphi_m = (\varphi_o - \varphi_i)$

$$M_2 = \frac{1}{3}\begin{pmatrix} 1+2q\cos(\omega_m t) & 1+2q\cos(\omega_m t-\frac{2\pi}{3}) & 1+2q\cos(\omega_m t-\frac{4\pi}{3}) \\ 1+2q\cos(\omega_m t-\frac{2\pi}{3}) & 1+2q\cos(\omega_m t-\frac{4\pi}{3}) & 1+2q\cos(\omega_m t) \\ 1+2q\cos(\omega_m t-\frac{4\pi}{3}) & 1+2q\cos(\omega_m t) & 1+2q\cos(\omega_m t-\frac{2\pi}{3}) \end{pmatrix} \quad 2\text{-}14$$

With $\varphi_m = -(\varphi_o + \varphi_i)$

The outcome of 2-13 yields $\varphi_i = \varphi_o$ giving the same phase dislocation at the input and output ports but the outcome of 2-14 yields $\varphi_i = -\varphi_o$ giving reversed phase displacement. By putting the two results together, we obtain the tools for input dislocation factor control. A direct transfer function method is presented in this basic solution, which is identified by the fact that, during each switches sequence time (T_{seq}), the typical output voltage is identical with the target voltage. Obviously, in order to make this happen the target voltages should be within the input voltage envelope for any output frequency that results in restriction of the highest voltage ratio.

2.4.3 Voltage Ratio Limitation and Optimization

The modulation solutions in 2-13 and 2-14 have a maximum voltage ratio q of 50% as illustrated in Figure 2-13.

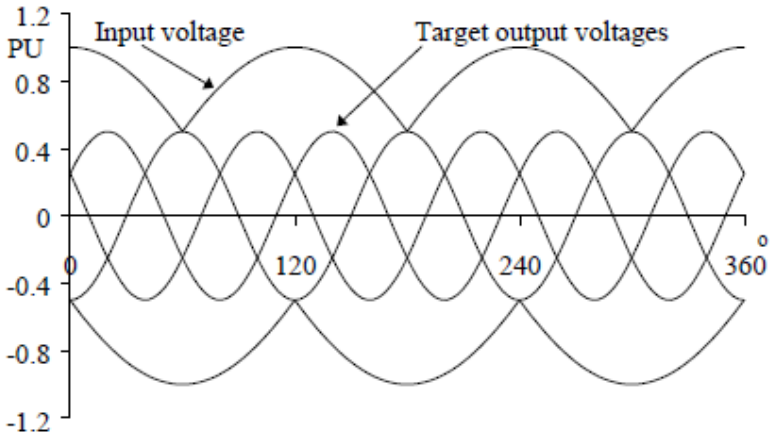

Figure 2-13 :The maximum voltage ratio of 50**%** *(Rodriguez, Pontt et al. 2007)*

The inclusion of common mode voltages to the demanded outputs can make improvements in the realizable voltage ratio to $\sqrt{3}/2$ or 87%, which is shown in equation 2-15.

$$U_o = qU_{im}\begin{pmatrix} \cos(\omega_o t) - \frac{1}{6}\cos(3\omega_o t) + \frac{1}{2\sqrt{3}}\cos(3\omega_i t) \\ \cos\left(\omega_o t + \frac{2\pi}{3}\right) - \frac{1}{6}\cos(3\omega_o t) + \frac{1}{2\sqrt{3}}\cos(3\omega_i t) \\ \cos\left(\omega_o t + \frac{4\pi}{3}\right) - \frac{1}{6}\cos(3\omega_o t) + \frac{1}{2\sqrt{3}}\cos(3\omega_i t) \end{pmatrix} \quad 2\text{-}15$$

The output line-to-line voltages are not affected by the common mode voltages, however the demanded outputs are permitted by common mode type to fit within the input voltage envelope with a value of q up to 87% as shown in Figure 2-14.

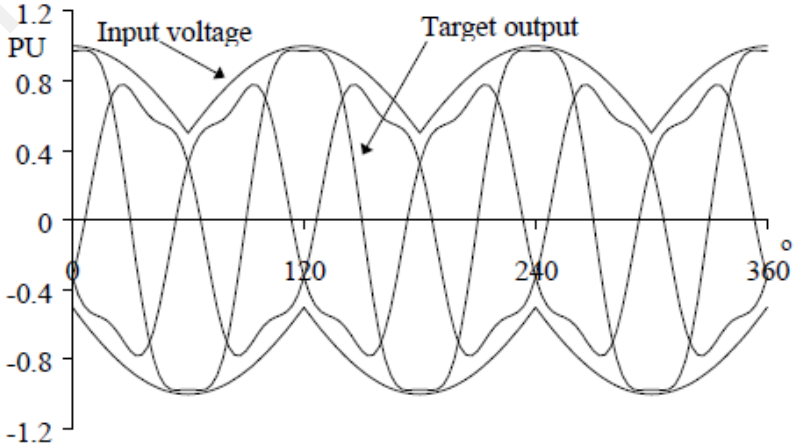

Figure 2-14 :The voltage ratio improvement to 87**%** (Rodriguez, Pontt et al. 2007)

If the null output states of the converter are redistributed (with a connection made between all output lines and the same input line), improvement in voltage ratio will be obtained which is parallel to an almost identical method in standard DC Link PMW converters. It is noticeable that where the target output voltage equals the mean output voltage during each switching sequence, a voltage ratio of 87% is the intrinsic maximum for any modulation method.

2.4.4 Scalar Modulation Methods

The most relevant modulation methods developed up to now, for the MC, are the scalar techniques and pulse width modulation methods (PWM). These MC modulations are efficient, but complex to understand, and synthesize compared to the three phase VSI modulations, consequently, its implementation is difficult in digital processors. An alternative solution conventionally in use is to apply SVM for MCs (Jussila & Tuusa, 2006; Johann W Kolar, Frank Schafmeister, Simon D Round, & Hans Ertl, 2007; Jose Rodriguez, Rivera, Kolar, & Wheeler, 2012; Zarri, Mengoni, Tani, & Ojo, 2014).

2.4.4.1 Venturini Modulation Method

The direct approach (Venturini method) is primarily studied and utilized together with voltage source converters, which then gave rise to a direct current control method for matrix converters. This method has been introduced for MC by Venturini and Alesina in1980; the popularity of Venturini technique has been enhanced by employing the advanced direct current control method for MC (Mutschler & Marcks, 2002).

The contribution of their study was that the desired current has to be impressed into the load, and the current drawn from the mains, should be in phase with the voltage and should be almost sinusoidal. The validation of this approach was verified by implementing a 10-kVA matrix converter. The main targets of the direct current control can be observed as follows:

1) The current that is obtained from the mains is required to have the same phase as the voltage and ought to be almost sinusoidal, finally, the proper current has to be injected into the load.
2) This suggests that the line filter is being damped to 400*Hz* resonance frequency actively (Mutschler & Marcks, 2002).

The first approach that is applied by Venturini can be seen in equations 2-13 and 2-14. But, to calculate the switch timings directly from these equations is a tedious process and therefore not suitable for practical approach. It is easier to discuss them directly regarding the input voltages and the target output voltages (considering unity displacement factor) in the form of 2-16.

$$m_{kj} = \frac{t_{kj}}{T_{seq}} = \frac{1}{3}\left[1 + \frac{2U_k U_j}{U_{im}}\right] \qquad For \begin{cases} k = A, B, C \\ j = a, b, c \end{cases} \qquad 2\text{-}16$$

It can be neglected for the 50% voltage ratio restriction such an approach,. The common mode addition approach, illustrated in equation Eq.2-15, is used in Venturini's optimum method so that a maximum voltage ratio of 87% is gained. As can be seen in 2-16, the proper statement of the algorithm inclusive of dislocation factor control appeared in Venturini's important work which is regarded somehow difficult. It is also considered inappropriate for the real-time execution. In actuality, on condition that the unity input dislocation element is necessary, then the algorithm can be seen in a simpler way in the form of 2-17.

$$m_{kj} = \frac{1}{3}\left[1 + \frac{2U_k U_j}{U_{im}^2} + \frac{4q}{3\sqrt{3}}\sin(\omega_i t + \beta_k)\sin(3\omega_i t)\right]$$

$$For\ K = A,\ B,\ C\ and\ j = a,\ b,\ c \qquad 2\text{-}17$$

$$\beta_k = 0\ , \frac{2\pi}{3}\ , \frac{4\pi}{3}; For = A,\ B,\ C\ respectively$$

Considering that in 2-17, the target output voltages, U_j , comprise the common mode addition defined in 2-15. In 2-17 a foundation for the real-time execution of the optimum

amplitude the Venturini approach is offered which is coped with, by processors up to sequence (switching) frequencies of tens of *kHz* at once. By entering a phase shift between the gauged input voltages and the output voltages, U_k, introduced into 2-17 the input dislocation element control is introduced. However, similar to other approaches, the highest voltage ratio is the price paid for the displacement factor control.

A research has been conducted to improve proper digital carrier modulation schemes based on Venturini approach in order to monitor direct and indirect matrix converters. It has minimized semiconductor commutation count and level sextant transitions with accurate states produced (Loh, Rong, Blaabjerg, & Wang, 2009). For the last two characteristics to be guaranteed, it is obligatory to select appropriate sampling instants and state sequence reversal which is shown in the paper for the two different topological options. It must be added that so far such aspects have not been forward in the present literature (Reddy, Anish, Selvan, & Moorthi, 2015).

2.4.4.2 Roy's Modulation

One typical modulation method is Roy's the "scalar" modulation method (Dementyev, Bragin, Kojain, & Udut, 2015; Meng-Jiang & Po-Tai, 2015). This method prepares the development where the switch actuation signals are computed directly from gauging of the input voltages. The complexity of the Venturini approach is considered as the motivation behind their development. Quantification of the immediate input voltages and contrasting their partial greatness are what the scalar method relies on. The elements of this method have been described as:

1) The subscript *m* is assigned to the input with a different polarity to the other.
2) The subscript *L* is assigned to the smallest (absolute) of the other two inputs.

The third input is assigned to subscript *k* and then the modulation duty cycles are given:

$$m_{Lj} = \frac{(U_j - U_m)\,\mathrm{U}_L}{1.5U_{im}^2}, m_{kj} = \frac{(U_j - U_m)\,\mathrm{U}_k}{1.5U_{im}^2}$$

$$m_{mj} = 1 - (\mathrm{m}_{Lj} + m_{kj}); \mathrm{j} = \mathrm{a}, \mathrm{b}, \mathrm{c} \qquad \text{2-18}$$

With the target output voltages, U_j, common mode addition is used to achieve 87% voltage ratio capability. This method, despite of an obvious dissimilarity, gives exactly alike switch timings to the optimum Venturini method. The modulation duty cycles for the scalar method that are expressed in the form of 2-17are given in 2-19.

$$m_{kj} = \frac{1}{3}\,[1 + \frac{2U_k U_j}{U_{im}} + \frac{2}{3}\sin(\omega_i t + \beta_k)\sin(3\omega_i t)] \qquad \text{2-19}$$

At maximum output voltage (q = √3/2), equations 2-17 and 2-19 are identical. The only difference between the methods is that the rightmost term addition is taken pro-rata with q in the Venturini method and is fixed at its maximum value in the scalar method. The effect on output voltage quality is negligible except at low switching frequencies where the Venturini method is superior.

2.4.5 Space Vector Modulation Method

One of the most popular methods of the switching algorithm to control the PWM is the Space Vector Modulation (SVM). Various models of SVM result in different quality and computational requirements. The reduction of THD is the common advantage of all types of SVM, because of providing the inherent fast switching (Irwin, Kazmierkowski, Krishnan, & Blaabjerg, 2002).

In (Holtz & Boelkens, 1989),four different modulation strategies are evaluated, all of them are found on direct SVM approach.. Additionally, the objective of the reducing switching losses can be explained by a new space-vector method which decreases the rate of switching losses ranging from 15% to 35% depending on the output load angle. Both simulations and experimental tests have verified the practicality of the modulation

scheme; it has also been compared to waveforms gained by utilizing existing space vector modulation schemes. The modulation method could be applied where:

1) The output voltage is well-stable where the half of output voltage reference meets the input voltage.
2) The output voltage quality is higher than the standard SVM scheme.

They (Holtz & Boelkens, 1989) have proved the reduced losses in the modulation method and somehow verified the suggested evaluation method in order to show how their system operates. By performing all modulation schemes, they attempted to simulate a matrix converter to drive an IM. It was proven through analytical as well as simulation method. However, in respect of the input and output waveform quality, both Stages Over-modulation (BSO) in the conventional method (10-BSOs strategy) was better; in respect of switching losses, their modified 8-BSO modulation was the most efficient and by conducting experimental tests it was shown that the discussed modulation schemes are practical.

Recently, some improvements have been presented as a simple SVM technique for five-phase matrix converters and considered the BSO region (Dabour, Allam, & Rashad, 2015).

Except for the low switching frequencies where the Venturini method is higher level, the impact on output voltage quality is considered trivial. A famous and accepted method in conventional PWM inverters is the space vector method. Though more complicated, its employment in matrix converters is conceptually almost identical. The SVM can control the output voltage and input current, with a matrix converter. There is a detailed discussion of the SVM and its relationship to other approaches in another paper in this issue (Niaki et al., 2014). Here just output voltage control is studied to determine the basic

principles. In 2-20, the voltage space vector of the target matrix converter output voltages is defined in terms of the line-to-line voltages.

$$U_o(t) = \frac{2}{3}\left(U_{ab} + a.\mathrm{U}_{bc} + a^2.\mathrm{U}_{ca}\right) \text{ where } a = e^{j\frac{2\pi}{3}} \qquad 2\text{-}20$$

In the complex plane, $U_o(t)$ is a vector of constant length ($\sqrt{3}$qU_{im}) revolving at sharp-cornered frequency ω_o. In the SVM, $U_o(t)$ and time are synthesized, averaging from an alternative group of neighbouring vectors in the set of converter output vectors in each sampling period. The choice of vectors for a matrix converter is not unique at all and a number of remaining possibilities are not studied here. For a three-phase Matrix Converter the twenty seven possible output vectors fall into three groups that have the following features:

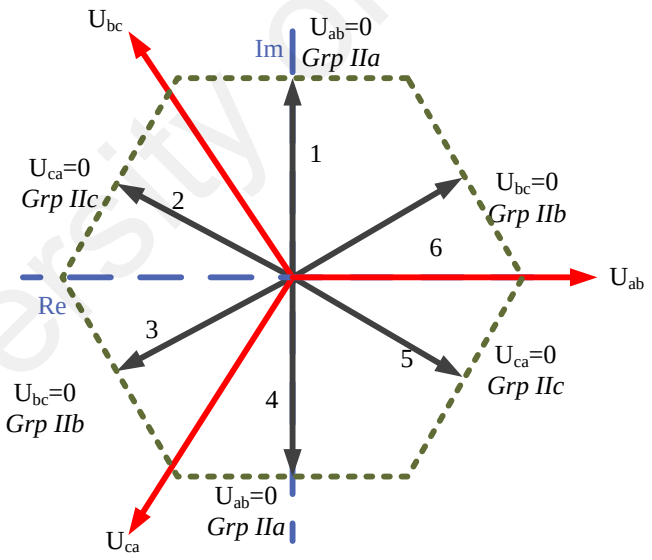

Figure 2-15: Output voltage space vectors

The twenty-seven possible output vectors for a three-phase MC can be classified into three groups with the following characteristics:

Group I: each output line is connected to a different input line. Output space vectors spin (in either direction) at the supply angular frequency and remain unchanged in amplitude.

Group II: two output lines are connected to a common input line; other input lines are connected to the remaining output line. Output space vectors have differing volume and fixed direction settling in one of six positions regularly spaced 60° away from one another. The maximum length of these vectors is $2/\sqrt{3}.U_{env}$ where U_{env} is the momentary value of the rectified input voltage envelope.

Group III: A common input line is connected to all output lines. Output space vectors have zero amplitude (that is, located at the origin). The group I vectors are not used in the SVM. From the group II, active vectors and the group III, zero vectors the target output is synthesized. In Figure 2-15 the hexagon of probable output vectors can be seen, where the group II vectors are further sub-divided dependent on which output line to line voltage is zero. We can see an example of how $U_o(t)$ could be synthesized when it lies in the sextant between vector 1 and vector 6 in Figure 2-16. $U_o(t)$ is produced during the switching sequence through time averaging by choosing the time spent in vector 1 (t_1) and vector 6 (t_6). However, this does not have to be the case; here maximum length vectors are put to work.

2-21 is deducted from Figure 2-16, where t_0 is the time spent in the zero vector (at the origin).

$$t_1 = \frac{|U_o|}{U_{env}} T_{seq} \sin(\theta),$$
$$t_6 = \frac{|U_o|}{U_{env}} T_{seq} \sin(60-\theta), \qquad 2\text{-}21$$
$$t_0 = T_{seq} - (t_1 + t_6)$$

where t_0 is the time spent in the zero vector (at the origin).

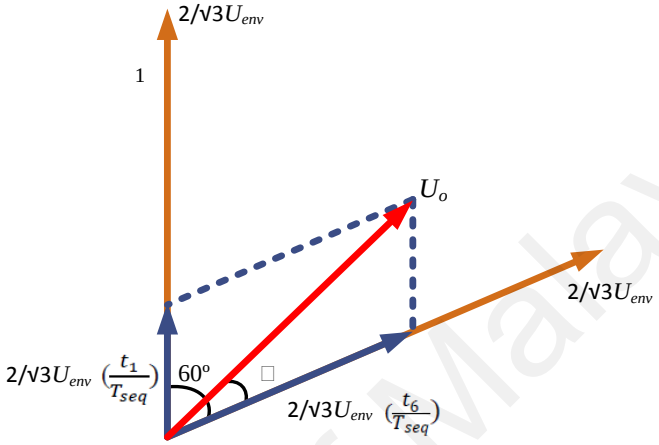

Figure 2-16 : Example of output voltage space vector synthesis

It is not possible to find an exclusive way to distribute the times (t_1, t_6, t_0) within the switching sequence. One suggested method is shown in Figure 2-17.

In order to obtain a favorable harmonic functioning at the input and output ports applying the SVM to input current control and output voltage control is obligatory. This, in general, necessitates four active vectors in each switching sequence, although the concept remains the same. The SVM method, under balanced and impartial input and output circumstances, shows results that are similar to the other methods mentioned earlier. The increased resilience, in a choice of switching vectors for both input current and output voltage control, though, is likely to manifest useful advantages under unbalanced circumstances.

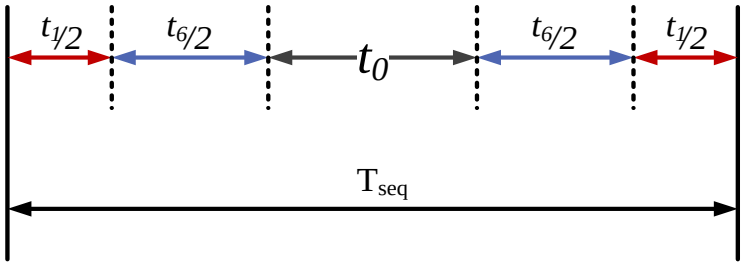

Figure 2-17: Possible way of allocating states within switching sequence

2.4.6 Predictive Control Method

The predictive control model is the innovative method of process control that has been industrialized in chemical and oil plants since 1980. Recently, it has also been utilized in power system issues (Arnold & Andersson, 2011). The modulator of predictive controllers depends on dynamic prototypes of the process, most frequently linear empirical prototypes obtained by system identification (Richalet, Rault, Testud, & Papon, 1978). In fact, the main advantage of this modulation is to optimize the current time-slot, while the future time-slots are simultaneously taken into account. The predictive modulation has two subcategories as current and torque control.

The current regulators for AC inverters are commonly categorized as hysteresis, linear PI, or deadbeat predictive regulators, with a further sub-classification into stationary ABC frame and synchronous d-q frame implementations. Zmood and Holmes have prepared an intelligent control method as predictive scheme in 2003. Their research has presented the relationship between synchronous and stationary frame regulators from a control system and signal processing perspective and has also shown how the regulator transfer function can be transformed instead of the AC current error, to achieve a stationary frame linear PI current regulator with zero steady-state error and a good transient performance. A significant advantage of this regulator is its application to single-phase current regulated systems, where synchronous frame transformations are more difficult to apply (Zmood & Holmes, 2003).

Another investigation on the execution of predictive monitoring scheme for an indirect matrix converter has been done to improve the performance using the torque control modulation (J. Rodriguez et al., 2007). A switching state is selected by the control scheme, which lessens the reactive power and the error in the output currents. It validates the reference values through a process. In order to achieve this goal, it utilizes a prediction horizon of a sample time and an inborn control law. The converter that functions at a sampling time of 20μs uses a standard digital signal processor. It has been observed that controlling such converter with a predictive method is easily executable and input currents with unity power factor along with a less than 5% harmonic distortion are achievable (J. Rodriguez et al., 2007).

2.4.7 Indirect Modulation Methods

The ultimate objective of these approaches is to raise the maximum voltage ratio above the 86.6% limit of the other ones. For this goal to be achieved, the modulation process, which is defined in 2-9 is split into two steps as indicated in 2-22.

$$U_o = \left(AU_i\right)B \qquad 2\text{-}22$$

Pre-multiplication of the input voltages by A, in 2-22, creates a "fictitious DC-link" and post multiplication by B forms the proper output by modulating the fictitious DC-link. Generally, A is pointed out as the "rectifier transformation" and B as the "inverter transformation" which results from the resemblance in concept with a traditional rectifier/DC-link/inverter system. A is given by 2-23.

$$A = K_A \begin{pmatrix} \cos(\omega_i t) \\ \cos(\omega_i t + \frac{2\pi}{3}) \\ \cos(\omega_i t + \frac{4\pi}{3}) \end{pmatrix}^T \qquad 2\text{-}23$$

Hence:

$$U_i = K_v U_{im} \begin{pmatrix} \cos(\omega_i t) \\ \cos(\omega_i t + \frac{2\pi}{3}) \\ \cos(\omega_i t + \frac{4\pi}{3}) \end{pmatrix}^T \begin{pmatrix} \cos(\omega_i t) \\ \cos(\omega_i t + \frac{2\pi}{3}) \\ \cos(\omega_i t + \frac{4\pi}{3}) \end{pmatrix} = \frac{3K_A U_{im}}{2} \qquad 2\text{-}24$$

B is given by 2-25.

$$B = K_B \begin{pmatrix} \cos(\omega_o t) \\ \cos(\omega_o t + \frac{2\pi}{3}) \\ \cos(\omega_o t + \frac{4\pi}{3}) \end{pmatrix} \qquad 2\text{-}25$$

Hence:

$$U_o = AU_i B = \frac{3K_A K_B U_{im}}{2} . \begin{pmatrix} \cos(\omega_o t) \\ \cos(\omega_o t + \frac{2\pi}{3}) \\ \cos(\omega_o t + \frac{4\pi}{3}) \end{pmatrix} \qquad 2\text{-}26$$

The voltage ratio $q = 3K_AK_B/2$. It is obvious that the *A* and *B* modulation steps are interrupted in time as it can be seen above, although they must be implemented by an appropriate choice of the switching states. *To* increase the voltage ratio as much as possible the step in A is implemented in order to continuously select the most positive and the most negative input voltages. This yields $K_A = 2\sqrt{3}/\pi$ with a fictitious DC link of

$3\sqrt{3}Uim/\pi$ (almost identical with a 6-pulse diode bridge with a resistive load). K_B stands for the modulation index of a PWM process and is the maximum value (square wave modulation) of $\frac{2}{\pi}$.

As a result, the overall voltage ratio q has the highest value of $\frac{6\sqrt{3}}{\pi^2} = 105.3\%$ .The achievable voltage ratio is overtly larger than that of other techniques, even though the progress is experienced at the expense of the quality of either the input currents, the output voltages or both. For values of $q > 0.866$, the mean output voltage does not equal to the target output voltage in each switching interval anymore. Low-frequency distortion is resulted from this unavoidability in the output voltage and/or the input current in comparison to other methods with $q < 0.866$. The indirect method yields very similar results to the direct method for $q < 0.866$.

2.4.8 DTC Modulation Method

In control algorithm of IM driver, two elegant and powerful control methods are currently used to control the speed, torque and flux of IM fed by MC. They are listed as field-oriented control (FOC) and DTC (Takahashi & Noguchi, 1986). The advantages of DTC are no requirements for coordinate transformations, decoupling processes for both voltage and currents, robust and fast torque response, robustness against parameter variation, no requirements for PWM pulse generation and current regulators (Lascu, Boldea, & Blaabjerg, 2000). However, the main drawback of the DTC scheme is the high current and torque ripple. The disadvantages of DTC scheme also include variable switching frequency, and difficult-to-control torque and flux at very low speeds (C. L. Xia, J. X. Zhao, Y. Yan, & T. N. Shi, 2014; Zaid, Mahgoub, & El-Metwally, 2010).

The researchers have reported various voltage-vector-selection strategies for matrix converter based DTC scheme (Domenico Casadei, Serra, & Tani, 2001; K.-B. Lee & Blaabjerg, 2007; Ortega, Arias, Caruana, Balcells, & Asher, 2010). The advantages of the

matrix converter were combined with the advantages of the DTC schemes in (Domenico Casadei et al., 2001). The use of matrix converter input voltages with different amplitudes in order to reduce the inherent torque ripple that appears when direct torque control is applied to drive PMSM was investigated in (Ortega et al., 2010). An improved DTC-SVM method for sensor-less matrix converter drives using an over modulation strategy and a simple nonlinearity compensation was proposed in (K.-B. Lee & Blaabjerg, 2007) to overcome the degrading of dynamic torque response as compared to the basic DTC method and improve the phase-current distortion due to the nonlinearity of the matrix converter. However, in all the above-mentioned researches, authors utilized conventional (60°-sector) voltage vector selection algorithm, which limits the degrees of freedom to select voltage vectors. Thus, the torque ripple is significant, which may not be acceptable for high-performance drives (Takeda, Yoshinaga, Tanaka, Naka, & Inomata, 2015).

Lately, researchers have proposed the switching strategy by dividing the space vector into twelve 30° sectors (An, Sun, Zhong, & Matsui, 2012; Gharakhani & Radan, 2007; Kumar, Gupta, & Kumar, 2006a; Nguyen, Lee, & Chun, 2009; Chintan Patel et al., 2012; C Patel et al., 2011; Pavithra, Sivaprakasam, & Manigandan, 2011; C. Xia, J. Zhao, Y. Yan, & T. Shi, 2014b). The switching loss for three-phase VSI by re-carving the six sectors up into twelve ones were minimized in (An et al., 2012). The THD of line-to-line output voltage and peak value of common-mode voltage for an RL load powered through the matrix converter was reduced (Nguyen et al., 2009).

In (Gharakhani & Radan, 2007; Pavithra et al., 2011) , neutral point clamped (NPC) multi-level inverter combined with 12 sector methodology was performed for DTC of IM drive. In (C. Xia et al., 2014b), a novel DTC of MC-Fed permanent-magnet synchronous motor drives using duty cycle control for torque ripple reduction was proposed. In (Alsofyani & Idris, 2016; Kumar et al., 2006a; Chintan Patel et al., 2012; C Patel et al.,

2011), the authors applied 12-sided polygonal space vector based instead of hexagonal based voltage vectors for IM drive by implementing VSI. However, in all listed publications, the focus has not been on development of switching strategy for matrix converter based DTC of IM drive. Moreover, the development of switching strategy, switching lookup table, stator flux variation, torque variation and improvement of degrees of freedom are not discussed profoundly.

2.4.8.1 The Property of Torque with Flux and Stator Current

As introduction of DTC, we need to discuss the relation between the torque and stator current, which has been defined as shown in 2-27 ,

$$\vec{T}_e = \frac{3}{2}.\frac{P}{2}.(\vec{\psi}_s \times \vec{I}_s) \qquad 2\text{-}27$$

where the $\vec{\psi}_s$ is the vector of stator flux. $\vec{I}_s$ is the vector of stator current which can be replaced by the rotor flux ($\vec{\psi}_r$). As shown in Figure 2-18, the flux linkage of stator and rotor can be expanded as follows,

$$\begin{aligned} \vec{\psi}_s &= L_s \vec{I}_s + L_m \vec{I}_r \\ \vec{\psi}_r &= L_r \vec{I}_r + L_m \vec{I}_s \end{aligned} \qquad 2\text{-}28$$

L_s and L_r are the stator and rotor inductance respectively. The equivalent values for them can be written as:

$$\begin{aligned} L_s &= L_{ls} + L_m \\ L_r &= L_{lr} + L_m \end{aligned} \qquad 2\text{-}29$$

L_{ls} is the leakage inductance of stator and L_{lr} is the leakage inductance of rotor. L_m is the magnetizing inductance.

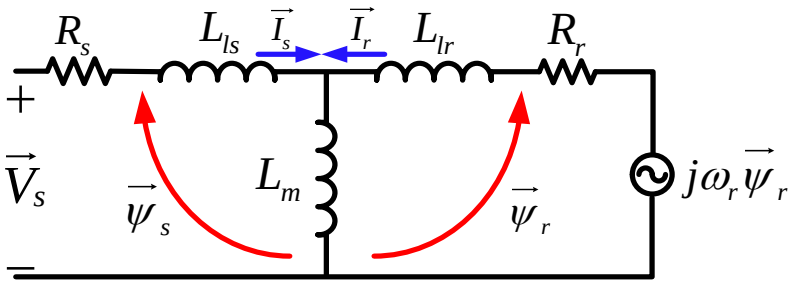

Figure 2-18: The equivalent circuit of IM

From the 2-28, the vector of rotor current $\vec{I}_r$ can be obtained as,

$$\vec{I}_r = \frac{1}{L_r}\vec{\psi}_r - \frac{L_m}{L_r}\vec{I}_s \qquad 2\text{-}30$$

therefore,

$$\vec{\psi}_s = \frac{L_m}{L_r}\vec{\psi}_r + L_s'\vec{I}_s \qquad 2\text{-}31$$

where the L_s' is defined in 2-32. It is obvious that L_r' has the same definition, but in the rotor side,

$$L_s' = \frac{L_s L_r - L^2{}_m}{L_r} \qquad 2\text{-}32$$

Consequently, the stator current vector ($\vec{I}_s$) can be expanded based on flux linkage of stator and rotor, as shown in 2-33.

$$\vec{I}_s = \frac{1}{L_r'}\vec{\psi}_s - \frac{L_m}{L_r L_s'}\vec{\psi}_r \qquad 2\text{-}33$$

Hence, by replacing the 2-33 in 2-27, we have the new property of the electromagnetic torque.

$$\vec{T}_e = \frac{3}{2}.\frac{P}{2}.\frac{L_m}{L_r L_s'}(\vec{\psi}_s \times \vec{\psi}_r) \qquad 2\text{-}34$$

which the magnitude of T_e is,

$$T_e = \frac{3}{4}.\mathrm{P}.\frac{L_m}{L_r L_s'}.|\vec{\psi}_s| \times |\vec{\psi}_r|.\sin\gamma \qquad 2\text{-}35$$

In 2-35, γ is the angle between the stator and rotor flux. γ is denoted as load angle. Figure 2-19 shows the vector relation of 2-34.The ΔT_e is the varying of T_e, when the rotor flux is constant, the stator flux increases for $\Delta\vec{\psi}_s$, and γ is changing with $\Delta\gamma$.

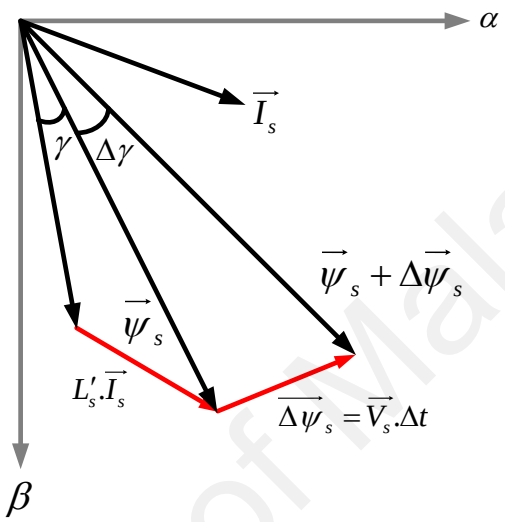

Figure 2-19: The vector of stator current, stator and rotor flux in αβ system (the stator resistor is not considered)

By the stator voltage vector ($\vec{V}_s$), the vector of stator flux can change fast but the rotor flux vector varies slowly because of its large time constant. Therefore, it can be assumed that the vector of rotor flux is constant for the short time durations. This statement can be proven with considering the relation between the flux linkage of rotor and flux linkage of stator based on rotor (Vas, 1998).

$$\vec{\psi}_r^{\,r} = \frac{L_m}{L_s}.\frac{\vec{\psi}_s^{\,r}}{1+s.(\sigma\tau_r)} \qquad 2\text{-}36$$

As can be seen in 2-36, the rotor flux has a first order delay than stator flux. Therefore, the assumption of time constant is correct. According to 2-35, if the magnitude of stator flux was constant, then the electromagnetic torque can be increased and decreased by changing the load angle. Increasing γ can rise the electromagnetic torque and diminishing

the γ can decrease the T_e. Hence, DTC system controls the variation of space vector of stator flux linkage (based on rotor flux linkage). The angle of γ can be modified by selecting the proportional voltage space vector to apply as switching state in VSI part.

Moreover, the angle of γ is not the only factor to determine the appropriate space vector of voltage. The magnitude of stator flux linkage is another factor. As can be seen in Figure 2-18, the relation between the stator flux linkage and stator voltage vector is,

$$\overrightarrow{V_s} = R_s \overrightarrow{I_s} + \frac{d}{dt}(\overrightarrow{\psi_s}) \qquad 2\text{-}37$$

The dropped voltage in the stator resistance is neglect. Therefore, the stator flux equation can be considered as:

$$\overrightarrow{V_s} = \frac{d}{dt}(\overrightarrow{\psi_s}) \qquad 2\text{-}38$$

while it can be expressed for the short period as well,

$$\Delta\overrightarrow{\psi_s} = \overrightarrow{V_s}.\Delta t \qquad 2\text{-}39$$

2-39 indicates that by applying the voltage vector ($\overrightarrow{V_s}$) for a period of time (Δt), the magnitude of stator flux varies for $\Delta\overrightarrow{\psi_s}$. The voltage vector is the output voltage of inverter, which is changing the magnitude of stator voltage vector with the appropriate speed.

2.4.8.2 The Control Strategy of DTC

The general block diagram of direct torque and flux control (Takahashi & Noguchi, 1986) is depicted in Figure 2-20. The command values of stator flux ($\overrightarrow{\psi_s}^*$) and the torque ($T_e^*$) are compared with estimated values of $\overrightarrow{\psi_s}$ and T_e respectively. They are the measured values of motor, which are the representatives of real values of stator flux and the torque. The result of this comparison can create the flux error (E_ψ) and torque error

(E_{T_e}). These results should be transferred to two independent hysteresis control units to determine the appropriate bands. In the flux control loop, a 2-level hysteresis is used that can be expanded as follow,

$$H_\psi = +1 \xrightarrow{for} E_\psi \geq +HB_\psi$$
$$H_\psi = -1 \xrightarrow{for} E_\psi \leq -HB_\psi \qquad \text{2-40}$$

where $2HB_\psi$ is the bandwidth of flux hysteresis. In 2-40, if the flux error was more the half of bandwidth (positive side), then the hysteresis of flux increases. This increment command applies to the switching table unit with $H_\psi = +1$. Therefore, if the flux error was less than the half of bandwidth (with negative sign), then $H_\psi = -1$ command will be applied to the switching table unit.

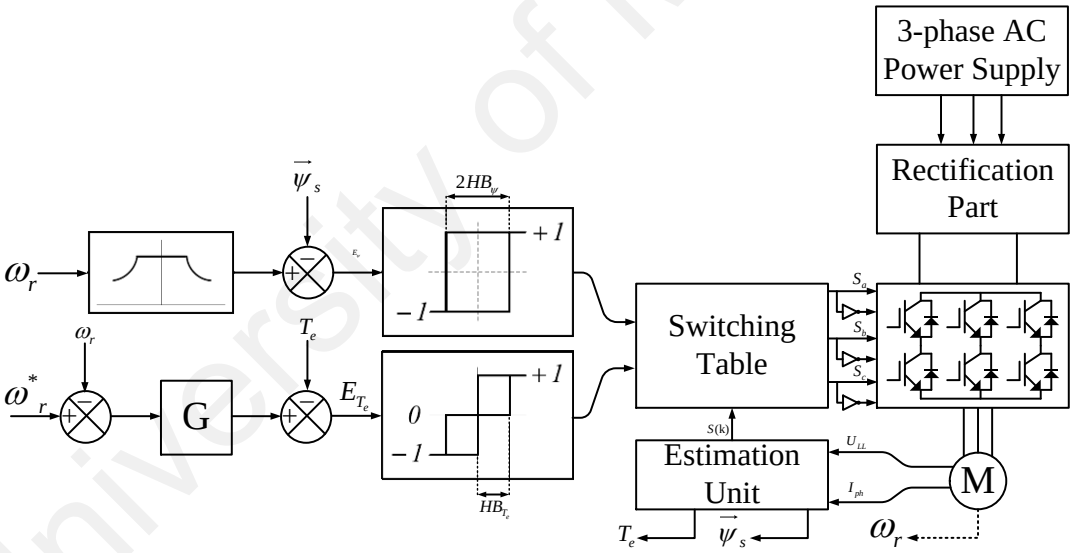

Figure 2-20: The block diagram of direct torque and flux control

In the torque control loop, the hysteresis unit is 3-level that each level has the following commands:

$$
\begin{aligned}
H_{T_e} = +1 &\xrightarrow{for} E_{T_e} \geq +HB_{T_e} \\
H_{T_e} = 0 &\xrightarrow{for} -HB_{T_e} < E_{T_e} < +HB_{T_e} \\
H_{T_e} = -1 &\xrightarrow{for} E_{T_e} \leq -HB_{T_e}
\end{aligned}
\qquad \text{2-41}
$$

$H_{T_e} = +1$ is the increase command, similar to hysteresis of flux, $H_{T_e} = -1$ is the decrease command, and $H_{T_e} = 0$ means continue without no change (Lascu, Jafarzadeh, Fadali, & Blaabjerg, 2015).

The DTC control strategy, based on the vectors in $\alpha\beta$ system, is illustrated in Figure 2-21. The command value of stator flux ($\overrightarrow{\psi_s}^*$) is rotating anti-clockwise with the circle shape path in the hysteresis band. The real value of $\overrightarrow{\psi_s}$ is surrounded by the 0.

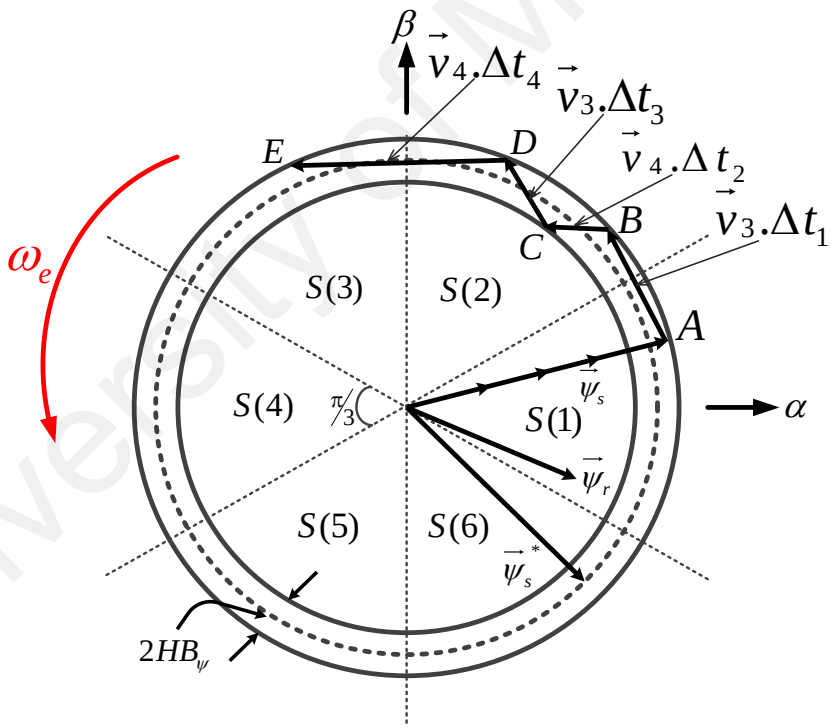

Figure 2-21: The path of stator flux in DTC

The output currents and voltages should be transferred into the signal-processing block (estimation unit) to create a feedback in direct control of flux and torque. This block determines not only the appropriate flux and torque, but also the sector number, which

the stator flux vector has been placed on it. In Figure 2-21, six sectors are shown, which each division has 60°.

As can be seen in Figure 2-20, the switching table block needs the values of hysteresis control of stator flux, torque and the position of flux vector (*S(k)*). Therefore, the switching table values can be predicted as a look-up table, which can select the applicable voltage vector for the inverter, and, consequently, the appropriate command switching state.

The most simplified inverter is the 2-level VSI with six semiconductor switches as can be seen in Figure 2-22.

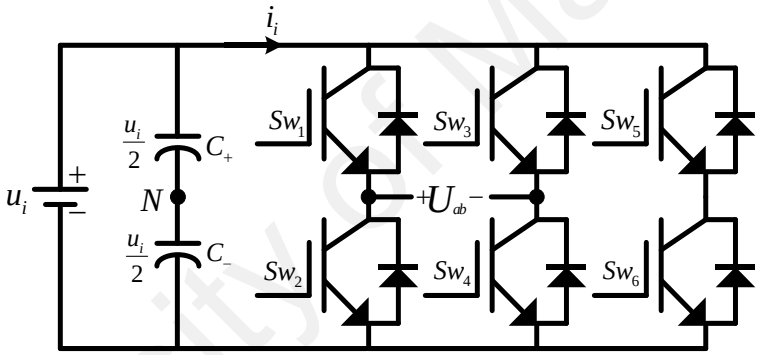

Figure 2-22:2-level inverter

This inverter has total eight possible switching states, which are including the six active positions and two zero vectors ($\vec{v}_0$ and $\vec{v}_7$). The possible switching states and the condition of each semiconductor switch are illustrated in Table 2-3 (Ng, 2015).

Table 2-3: The possible switching states and their condition for 2-level inverter

$\vec{v}_k$	$S_a(t)$	$S_b(t)$	$S_c(t)$	Sw_1	Sw_2	Sw_3	Sw_4	Sw_5	Sw_6
$\vec{v}_0$	0	0	0	OFF	ON	OFF	ON	OFF	ON
$\vec{v}_1$	1	0	0	ON	OFF	OFF	ON	OFF	ON
$\vec{v}_2$	1	1	0	ON	OFF	ON	OFF	OFF	ON
$\vec{v}_3$	0	1	0	OFF	ON	ON	OFF	OFF	ON
$\vec{v}_4$	0	1	1	OFF	ON	ON	OFF	ON	OFF
$\vec{v}_5$	0	0	1	OFF	ON	OFF	ON	ON	OFF
$\vec{v}_6$	1	0	1	ON	OFF	OFF	ON	ON	OFF
$\vec{v}_7$	1	1	1	ON	OFF	ON	OFF	ON	OFF

The generated voltage vector is shown in Figure 2-23. Furthermore, the variation of stator flux is depicted in the period of Δt.

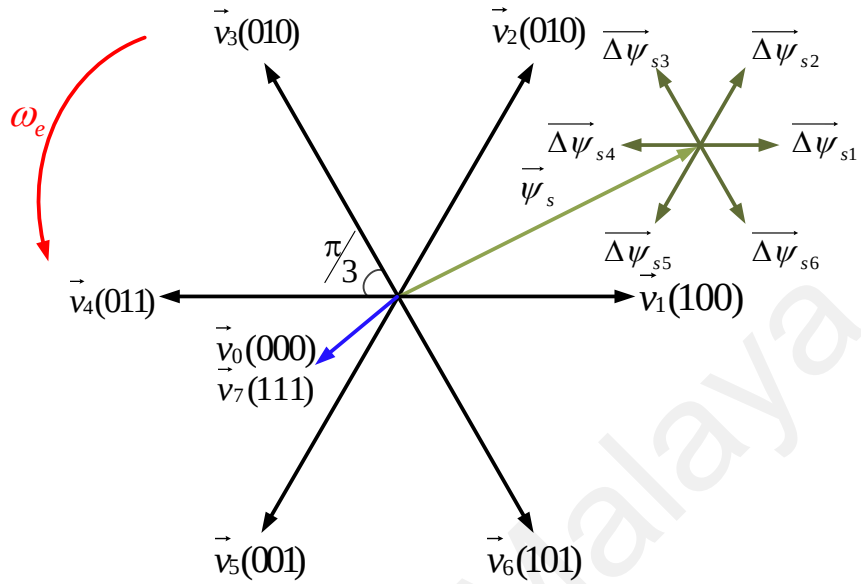

Figure 2-23: The voltage vectors of inverter and vectors of differential flux in Δt.

The variation of stator flux and torque, based on applied voltage vector, toward the position of stator flux vector, as illustrated in Figure 2-23, is summarized in Table 2-4. In the other words, Table 2-4 is summarizing the ratio of stator flux and torque in the state when proper voltage vector is applied versus the stator flux vector position, as illustrated in the Figure 2-23.

Table 2-4: The variation of torque and flux with applying the appropriate voltage vector toward the stator flux vector.

Voltage vector	$\vec{v}_1$	$\vec{v}_2$	$\vec{v}_3$	$\vec{v}_4$	$\vec{v}_5$	$\vec{v}_6$	$\vec{v}_0$	$\vec{v}_7$
ψ_s	↑	↑	↓	↓	↓	↑	0	0
T_e	↓	↑	↑	↑	↓	↓	↓	↓

The value of the stator flux is increased by applying the voltage vectors of $\vec{v}_1$, $\vec{v}_2$ and $\vec{v}_6$, while, the vectors of $\vec{v}_3$, $\vec{v}_4$ and $\vec{v}_5$ are decreasing the stator flux. Moreover, the voltage vectors of $\vec{v}_2$, $\vec{v}_3$ and $\vec{v}_4$ rise the electromagnetic torque, whereas, $\vec{v}_1$, $\vec{v}_5$ and $\vec{v}_6$ reduce T_e. However, the voltage vector of $\vec{v}_0$ and $\vec{v}_7$ are zero vectors, and, they apply no changes in the flux and torque, there will be slight decrement on the torque due to the voltage drop on stator resistant in short circuit condition (Cruz, 2004; Khoucha, Lagoun, Kheloui, & El Hachemi Benbouzid, 2011)

By assuming the position of the voltage vector in k^{th} sector ($1 \leq k \leq 6$), to extract a generalized switching table for 2-level inverter, with considering the Figure 2-24, 2-35 and 2-39, we have three consequences as follows,

1) The value of flux can be increased by selecting the $\vec{v}_k$, $\vec{v}_{k+1}$ and $\vec{v}_{k-1}$, while, it can be decreased by picking the $\vec{v}_{k+3}$, $\vec{v}_{k+2}$ and $\vec{v}_{k-2}$.
2) If the rotation of stator and rotor flux vector is assumed in anti-clockwise path, then, the value of electromagnet torque will be increased by selecting the $\vec{v}_{k+3}$, $\vec{v}_{k+2}$ and $\vec{v}_{k+1}$, and, decreased by selecting the $\vec{v}_k$, $\vec{v}_{k-2}$ and $\vec{v}_{k-1}$.
3) The stator flux can be stopped by picking the zero vectors; then, the rotor flux vector is going to be close to it. Therefore, the γ angle is diminished, and, consequently, the T_e will be decreased(Tripathy & Panigrahi, 2015).

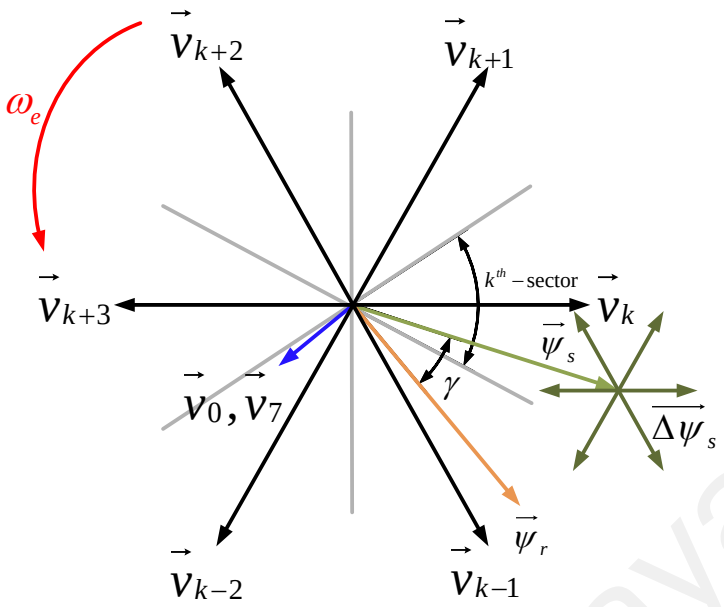

Figure 2-24: The space vector voltage with the stator and rotor flux vectors

According to the above-mentioned points and effect of each voltage vector on torque and flux of IM, the switching table for direct torque and flux control of an induction motor is presented in Table 2-5. It is noticeable that *s(k)* is the sector number, which the $\vec{\psi}_s$ is placed on it. Consequently, the procedure of DTC can be characterized as follows:

Based on Figure 2-24, with assuming the rise command ($H_{T_e}=+1$), the $\vec{v}_{k+1}$ can be used for increment and $\vec{v}_{k+2}$ for decrement. By selecting any of those vectors, the space vector of stator flux rotates in anti-clockwise path; then, the load angle is raised, consequently, the electromagnetic torque increases. This command remains until the torque error is negligible. To keep the former condition, no-change command must be executed ($H_{T_e}=0$). Therefore, the zero vector would be selected, and, the stator flux space vector stops the rotation, then, the rotor flux vector will close to the stator flux vector. This phenomena results the decrement of angle between them (γ); therefore, it drops the torque value. The no-change command would be considered, as the main operation order of DTC, as long as the torque value is greater than its reference, and, the torque error is in admissible band. The increase command will be applied when the torque error or/and

value pass the acceptable points; hence, the rotation of stator flux will be started, and, the increment command is the end-point of this loop (Pan, Wang, Su, Cheng, & Peng, 2015).

Table 2-5: The switching table in DTC for 2-level inverter

H_{ψ}	H_{T_e}	S(1)	S(2)	S(3)	S(4)	S(5)	S(6)
+1	+1	$\vec{v}_2$	$\vec{v}_3$	$\vec{v}_4$	$\vec{v}_5$	$\vec{v}_6$	$\vec{v}_1$
	0	$\vec{v}_7$	$\vec{v}_0$	$\vec{v}_7$	$\vec{v}_0$	$\vec{v}_7$	$\vec{v}_0$
	-1	$\vec{v}_6$	$\vec{v}_1$	$\vec{v}_2$	$\vec{v}_3$	$\vec{v}_4$	$\vec{v}_5$
-1	+1	$\vec{v}_3$	$\vec{v}_4$	$\vec{v}_5$	$\vec{v}_6$	$\vec{v}_1$	$\vec{v}_2$
	0	$\vec{v}_0$	$\vec{v}_7$	$\vec{v}_0$	$\vec{v}_7$	$\vec{v}_0$	$\vec{v}_7$
	-1	$\vec{v}_5$	$\vec{v}_6$	$\vec{v}_1$	$\vec{v}_2$	$\vec{v}_3$	$\vec{v}_4$

As an example, in Figure 2-21, by assuming the stator flux vector is in sector number 2 and at the point B. Moreover, we assume that the flux and torque values are very large and small respectively. Therefore, the hysteresis control commands the reduction of flux and increment of torque. Hence, $H_{\psi} = -1$ and $H_{T_e} = +1$ would be applied to the system. According to Table 2-5, the voltage vector of $\vec{v}_4$ is applied by the invertor, which creates the BC path for stator flux. At the C point, the command of hysteresis controllers will be changed to $H_{\psi} = +1$ and $H_{T_e} = +1$; then, the vector of $\vec{v}_3$ is extracted from the Table 2-5 to keep the stator flux vector in the control margin. The voltage vector should be change to the $\vec{v}_3$ and $\vec{v}_4$ respectively, In order to have the paths of CD and DE.

The employment of the zero vectors instead of other vectors bring some perceptible points as follow,

1) Selecting the zero vector ($\vec{v}_0$ and $\vec{v}_7$) instead of $\vec{v}_{k-1}$ and $\vec{v}_{k-2}$ in order to reduce the electromagnetic torque, decrease the switching frequency of inverter. If the value of torque exceeds the reference value, where the torque error passed the allowed

band and the reduction command of torque is issued ($H_{T_e} = -1$), then, $\vec{v}_{k-1}$ and $\vec{v}_{k-2}$ vectors will be selected to decrease quickly the load angle. This action rotates the stator flux vector in the clockwise path (the opposite direction of motor spin) (Ahmadi et al., 2014; Rahim et al., 2015).

2) Choosing $\vec{v}_0$ and $\vec{v}_7$ as zero vectors in each sector, is strongly related to their upper and lower vectors to have the minimum changing in switching state. Hence, the switching frequency is minimized (Korkmaz, Korkmaz, Topaloglu, & Mamur, 2014; Taïb, Metidji, & Rekioua, 2014).

2.4.8.3 Estimation of Torque and Flux

In this study, the estimator of flux is planned using the voltage modulation. The stator voltage vector ($\vec{V}_s$) and the stator current ($\vec{I}_s$) are employed to determine the stator flux vector as follow,

$$\vec{\psi}_s = \int_0^t (\vec{V}_s - R_s \vec{I}_s).dt \qquad 2\text{-}42$$

After estimating the stator flux, we can define the torque using the flux and stator current, as can be seen in :

$$T_e = \frac{3}{4}.\mathrm{p}.(\psi_{s\alpha} I_{s\alpha} - \psi_{s\beta} I_{s\beta}) \qquad 2\text{-}43$$

where the $\psi_{s\alpha}$ and $\psi_{s\beta}$ are the stator flux in αβ system.

2.4.8.4 Determining the Sector for Placing the Stator Flux Vector

For picking the appropriate voltage vector from the Table 2-5, we need to know the position of the stator flux vector. To determine its location, two ways are suggested as follows,

1) Calculating the load angle can be performed using trigonometry, then, compared its angle and the sector angle to find the vector location. This solution is not

recommended due to heavy computational procedure(Cho, Lee, Song, & Lee, 2015; Zhao, Zhang, Ren, & Li, 2015).

2) However, finding the exact place of flux linkage of stator is not required; the calculating of its sector is enough in DTC. Therefore, by using the sign of flux linkage of stator component in αβ system ($\psi_{s\alpha}$ and $\psi_{s\beta}$), the sign of simple statement of ($\sqrt{3}.|\psi_{s\beta}|-|\psi_{s\alpha}|$), and Table 2-6 the position of stator flux linkage can be determined.

Table 2-6: Determining the location of space vector of stator flux

Sign / Sector No.	S(1)	S(2)	S(3)	S(4)	S(5)	S(6)
$\psi_{s\alpha}$	+	+	-	-	-	+
$\psi_{s\beta}$	+-	+	+	+-	-	-
$\sqrt{3}.|\psi_{s\beta}|-|\psi_{s\alpha}|$	-	+	+	-	+	+

2.4.9 Comparison of Control Strategies for MC

As it mentioned in SVM section, low sampling and switching frequency is one of the most attractive features of PWM modulators; however, the scalar methods require the lower frequency for sampling and switching. This frequency is high for both of the predictive controls and very high for the DTC. The dynamic response of predictive control is the highest in comparing the others, while DTC can be categorized, as the second rank with the high-speed response, and the others are averagely ranked at medium-class.

Therefore, Table 2-7 illustrates more details about the difference between the above-mentioned methods, which can help us to select the best control approach based on the intended application.

Table 2-7: The comparison between the various control methods for MC (Jose Rodriguez et al., 2012)

Method / Item	Scalar (Roy)	Scalar (Venturini)	SVM	Carrier based PWM	Predictive (torque control)	Predictive (current control)	Direct torque control
Sampling frequency	very low	very low	low	low	high	high	very high
Switching frequency	very low	very low	low	low	high	high	high
Dynamic response	medium	medium	medium	medium	very high	very high	high
Input-filter resonance	low	low	low	medium	dependent	dependent	very high
Complexity	low	low	very high	very low	low	low	high

The advantages of DTC are no requirements for coordinate transformations, decoupling processes for both voltage and currents, robust and fast torque response, robustness against parameter variation, no requirements for PWM pulse generation and current regulators. However, the main drawback of the DTC scheme is the high current and torque ripple. The disadvantages of DTC scheme also include variable switching frequency and difficult-to-control torque and flux at very low speeds.

2.5 Chapter Summary

In this chapter, the practical topologies of MC family have been presented. The advantages and disadvantages of all types of topology have been discussed. Then, the feasible control methods of MC have been classified into four groups. Each group has been profoundly discussed. Moreover, the standard method of DTC is fully discussed which is essential for the next chapters.

According to MC topologies, USMC has less number of controllable switches and diodes. The conventional prototypes of MC in both direct and indirect layout, have 18 controllable switches plus 18 diodes. The DMC and IMC have the highest number of semiconductors, which can be considered as a drawback for the applications required

compact and lightweight system. Moreover, the power-flow is bidirectional in DMC and IMC. Therefore, wherever the power-flow is restricted to only one direction, the conventional MCs have no chance to be involved, while the USMC is unidirectional.

Based on the literature review of control sections, SVM methods have complex fundamental, but they require low switching and sampling frequency. Therefore, SVM can prepare the same performance and lower switching losses in compare with predictive or DTC schemes. The dynamic response of SVM is classified in the middle class and it reacts to the changes with approximate long time, while the fast dynamic response of DTC is the ordinary feature of it.

In the conventional DTC, the circular locus is divided into six sectors, and, eight voltage vectors are used. However, the discrete inverter switching vectors cannot always generate exact stator voltage required to obtain the demanded electromagnetic torque and stator flux linkages. This results in production of ripples in the flux as well as torque, and, recently, the ripples in the torque has been diminished more using same strategy and duty cycle optimization.

A unidirectional converter with less number of semiconductor components is required. Thus, the recommended topology is USMC. On the other hand, a rapid reflected system with low power losses is demanded. Therefore, the combination of SVM and DTC can prepare a fast responding system with low losses.

CHAPTER 3: METHODOLOGY

In this chapter, a novel switching approach based on 30° sectors of both flux and voltage is introduced to increase the degrees of freedom in choosing the voltage vectors. The change rates of both torque and flux of Induction Motor (IM) as a function of Matrix Converter (MC) voltage vectors are systematically derived.

In Ultra-Spars Z-source Matrix Converter (USZSMC) topology, the Particle Swarm Optimization (PSO) method is employed to tune K_P and K_I in the PI controller, and the coefficient of I_{ref} (reference current) and I_{load} (stator current). Under the abnormal input voltage, this control strategy is employed to minimize the THD of the output current while the output waveforms (current and voltage) are perfectly balanced. The size of Z-source converter has been reduced by applying a novel calculation method with respect to timing and circuit perspective.

The new SVM switching method of 12-sector DTC is implemented to drive an induction motor, while enhances the voltage transfer ratio through the Z-source network.

3.1 The Recommended Topology

The Ultra-Spars Z-source Matrix Converter is well-suited topology for those applications which require unidirectional power flow, high-voltage transfer ratio, and lightweight. Figure 3-1 depicts the block diagram of the topology, which is defined by the USZSMC consisting of an ultra-sparse rectifier and a two-stage inverter with only nine semiconductor switches and 18 diodes. A Z-source network connects the rectification to the inversion part.

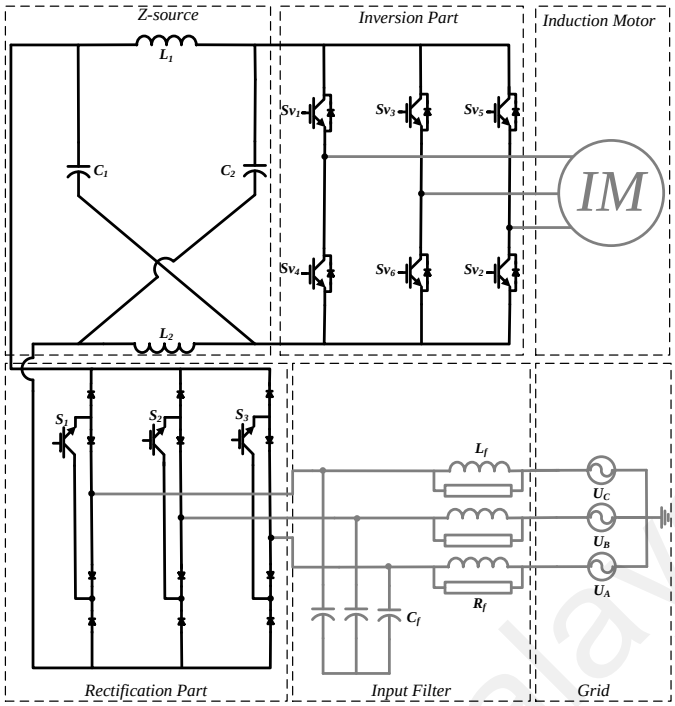

Figure 3-1: An ultra-sparse Z-source matrix converter topology

The Z-source network operates simultaneously as an energy reservoir and a filter to overcome the current and voltage ripple (Friedli, Kolar, Rodriguez, & Wheeler, 2012; C. Xia, J. Zhao, Y. Yan, & T. Shi, 2014a; C. L. Xia et al., 2014). A zero-current commutation of DC-link should be placed in the rectifier part; otherwise, due to the deliberate short circuit which generated from the Z-source inverter, the freewheeling state of inverter returns to the rectification part (Peng, 2003; Frank Schafmeister & Kolar, 2012). As depicted in Figure 3-1, inductors and capacitors are connected in an X shape, to form the impedance source at the DC-link (Z-source network). Although the USZSMC has been developed for eliminating three switches compared to the conventional model, it could provide all the desired characteristics that a common matrix converter would have, except bi-directionality of power flow.

3.2 Suggested DTC Scheme

Neglecting stator-resistance voltage drop, an induction machine's flux equation can be expressed as:

$$\overrightarrow{\Delta\psi_s} = \vec{V}_s \cdot \Delta t \qquad 3\text{-}1$$

Radial component (V_{sr}) of the stator-voltage space vector ($\vec{V}_s$) changes the stator-flux magnitude, and the tangential component (V_{st}) changes the stator-flux angle as shown in Figure 3-2. They can be expressed as:

$$V_{sr} = V_{s\alpha}\cos\theta + V_{s\beta}\sin\theta \qquad 3\text{-}2$$

$$V_{st} = -V_{s\alpha}\sin\theta + V_{s\beta}\cos\theta \qquad 3\text{-}3$$

where, θ is the angle of stator-flux vector $\vec{\psi}_s$.

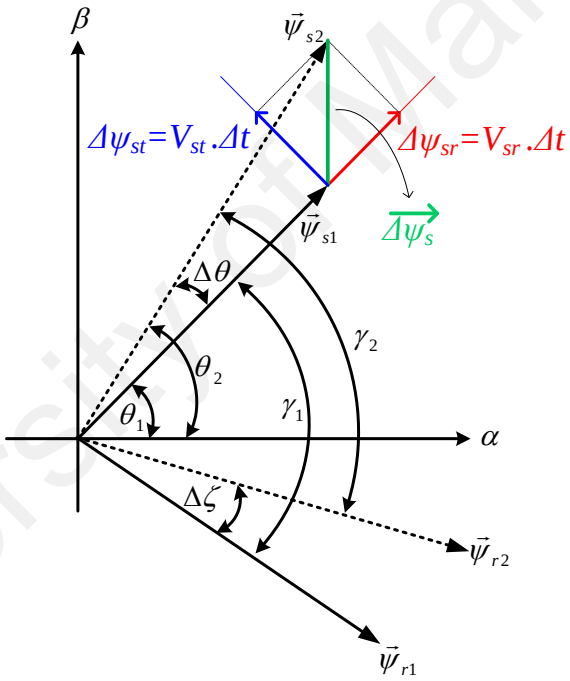

Figure 3-2: Variation of flux vectors pre and post applications of voltage vector in the corporation with DTC based IM drive

After applying a new voltage vector $\vec{V}_s$ for Δt time, the differential change in stator-flux linkage can be written as:

$$\Delta\left|\vec{\psi}_s\right| = \left|\vec{\psi}_{s2}\right| - \left|\vec{\psi}_{s1}\right| \cong V_{sr} \cdot \Delta t \qquad 3\text{-}4$$

Substituting V_{sr} from 3-2 in 3-4 gives:

$$\Delta|\vec{\psi}_s| = \left(V_{s\alpha}\cos\theta_1 + V_{s\beta}\sin\theta_1\right)\cdot\Delta t \qquad 3\text{-}5$$

which reveals the influencing characteristics of each voltage vector on magnitude variation of the stator-flux vector.

The developed electromagnetic torque of IM can be expressed by:

$$T_e = \frac{3}{2}\cdot\frac{P}{2}\cdot\frac{L_m}{\sigma\cdot L_s\cdot L_r}\cdot|\vec{\psi}_r|\cdot|\vec{\psi}_s|\sin\gamma \qquad 3\text{-}6$$

where, γ and σ are load angle and leakage factor, respectively. In order to see the torque variation caused by applying voltage space vector $\vec{V}_s$ during Δt, equation 3-6 is differentiated, assuming constant magnitude for rotor-flux vector during Δt owing to rotor's large time constant (Kumar, Gupta, & Kumar, 2006b). Thus, the following equation is obtained:

$$\Delta T_e = k_T\cdot|\vec{\psi}_r|\cdot\left(\frac{d|\vec{\psi}_s|}{dt}\cdot\sin\gamma + \frac{d(\sin\gamma)}{dt}\cdot|\vec{\psi}_s|\right)\Bigg|_{t_0}\cdot\Delta t \qquad 3\text{-}7$$

where, t_0 is the initial time, which is the time just before applying voltage vector. k_T is a constant defined as:

$$k_T = \frac{3}{2}\cdot\frac{P}{2}\cdot\frac{L_m}{\sigma\cdot L_s\cdot L_r} \qquad 3\text{-}8$$

Rearranging 3-7gives:

$$\Delta T_e = k_T\cdot|\vec{\psi}_r|\cdot\left(\frac{d|\vec{\psi}_s|}{dt}\Bigg|_{t_0}\sin\gamma_1 + \frac{d\gamma}{dt}\Bigg|_{t_0}\cos\gamma_1\cdot|\vec{\psi}_{s1}|\right)\cdot\Delta t \qquad 3\text{-}9$$

where, subscript '1' indicates the magnitude of specified variables at exactly t_0.

Equation 3-5 leads to:

$$\left.\frac{d\left|\vec{\psi}_s\right|}{dt}\right|_{t_0} = V_{s\alpha}\cos\theta_1 + V_{s\beta}\sin\theta_1 \qquad 3\text{-}10$$

where, θ_1 is the angle of stator-flux vector $\vec{\psi}_s$ just before applying voltage vector $\vec{V}_s$.

During Δt, variation of load angle $\Delta\gamma$ is given by:

$$\Delta\gamma = \Delta\theta - \Delta\zeta \qquad 3\text{-}11$$

where $\Delta\theta$ *and* $\Delta\zeta$ are variation of stator and rotor flux angle respectively, due to the application of the new voltage vector, V_s.

Again,

$$\Delta\left|\vec{\psi}_s\right| = \Delta\theta \cdot \left|\vec{\psi}_{s1}\right| \cong V_{st} \cdot \Delta t \qquad 3\text{-}12$$

Substituting V_{st} from 3-3in 3-12yields:

$$\Delta\theta = \frac{-V_{s\alpha}\sin\theta_1 + V_{s\beta}\cos\theta_1}{\left|\vec{\psi}_{s1}\right|} \cdot \Delta t \qquad 3\text{-}13$$

Hence:

$$\left.\frac{d\theta}{dt}\right|_{t_0} = \frac{-V_{s\alpha}\sin\theta_1 + V_{s\beta}\cos\theta_1}{\left|\vec{\psi}_{s1}\right|} \qquad 3\text{-}14$$

Considering rotor flux rotating with synchronous speed ω_s while magnitude remains nearly constant during Δt, $\Delta\zeta$ can be written as:

$$\Delta\zeta = \omega_s \cdot \Delta t \quad \Rightarrow \quad \left.\frac{d\zeta}{dt}\right|_{t_0} = \omega_s \qquad 3\text{-}15$$

3-11, 3-14, and 3-15can be written as:

$$\left.\frac{d\gamma}{dt}\right|_{t_0} = \left.\frac{d\theta}{dt}\right|_{t_0} - \left.\frac{d\zeta}{dt}\right|_{t_0} = \frac{-V_{s\alpha}\sin\theta_1 + V_{s\beta}\cos\theta_1}{\left|\vec{\psi}_{s1}\right|} - \omega_s \qquad 3\text{-}16$$

By substituting 3-10 and 3-16 in 3-9, expression for the torque variation becomes:

$$\Delta T_e = k_T \cdot \left|\vec{\psi}_r\right| \cdot (x - y) \cdot \Delta t \qquad \text{3-17}$$

where, x and y are:

$$\begin{aligned} x &= \left(V_{s\alpha} \cos\theta_1 + V_{s\beta} \sin\theta_1\right) \cdot \sin\gamma_1 \\ y &= \left(V_{s\alpha} \sin\theta_1 - V_{s\beta} \cos\theta_1 + \omega_s \left|\vec{\psi}_{s1}\right|\right) \cdot \cos\gamma_1 \end{aligned} \qquad \text{3-18}$$

For normalization of 3-5 and 3-17, rating values of the machine can be selected as base values:

$$V_m = \omega \cdot \psi_m \quad \Rightarrow \quad \psi_{base} = \frac{V_{base}}{\omega_{base}} = \frac{V_m}{\omega} \qquad \text{3-19}$$

and,

$$T_{e,base} = \frac{3}{2} \cdot \frac{P}{2} \cdot \frac{L_m}{\sigma \cdot L_s \cdot L_r} \cdot \left|\vec{\psi}_{r,base}\right| \cdot \left|\vec{\psi}_{s,base}\right| \cdot \sin\gamma_{base} \qquad \text{3-20}$$

where, the subscript 'base' indicates the base value.

$$\Delta\left|\vec{\psi}_s\right|_{pu} = \frac{\Delta\left|\vec{\psi}_s\right|}{\psi_{base}} = \frac{\left(V_{s\alpha} \cos\theta_1 + V_{s\beta} \sin\theta_1\right) \cdot \Delta t}{V_{base}/\omega_{base}} \qquad \text{3-21}$$

Per-unit equation for flux variation results:

$$\Delta\left|\vec{\psi}_s\right|_{pu} = \left(V_{s\alpha,pu} \cos\theta_1 + V_{s\beta,pu} \sin\theta_1\right) \cdot k_1 \qquad \text{3-22}$$

where, $k_1 = \omega_{base} \cdot \Delta t$.

Torque variation can be expressed in per-unit from 3-6 and 3-17 as follows:

$$\Delta T_{e,pu} = \frac{\Delta T_e}{T_{e,base}} = \frac{k_T \cdot \left|\vec{\psi}_r\right| \cdot (x - y) \cdot \Delta t}{k_T \cdot \left|\vec{\psi}_{r,base}\right| \cdot \left|\vec{\psi}_{s,base}\right| \sin\gamma_{base}} = \left|\vec{\psi}_{r,pu}\right| \cdot \left(x_{pu} - y_{pu}\right) \cdot \Delta t \qquad \text{3-23}$$

where,

$$x_{pu} = \left(V_{s\alpha,pu}\cos\theta_1 + V_{s\beta,pu}\sin\theta_1\right)\cdot\frac{\sin\gamma_1}{\sin\gamma_{base}}\cdot\omega_{base}$$
$$y_{pu} = \left(\left(V_{s\alpha,pu}\sin\theta_1 - V_{s\beta,pu}\cos\theta_1\right)\cdot\omega_{base} + \omega_s\cdot\left|\vec{\psi}_{s1}\right|_{pu}\right)\cdot\frac{\cos\gamma_1}{\sin\gamma_{base}} \quad 3\text{-}24$$

Equation 3-23for torque variation per-unit can be rewritten as:

$$\Delta T_{e,pu} = \left|\vec{\psi}_{r,pu}\right|\cdot\left\{\Delta\left|\vec{\psi}_s\right|_{pu}\left(\sin\gamma_1\right)_{pu} - \left(\left(V_{s\alpha,pu}\sin\theta_1 - V_{s\beta,pu}\cos\theta_1\right) + (2/p)\cdot\omega_{s,pu}\cdot\left|\vec{\psi}_{s1}\right|_{pu}\right)\cdot\sqrt{k_2 - \left(\sin\gamma_1\right)_{pu}{}^2}\cdot k_1\right\} \quad 3\text{-}25$$

where, $k_2 = \dfrac{1}{\left(\sin\gamma_{base}\right)^2}$.

Expression 3-25 is applicable to any size IM drive, but because of its dependency on γ_{base}, influencing characteristics of voltage vectors can differ in low and high power applications.

3.2.1 Fundamentals of Matrix Converter Based DTC Scheme

Based on the earlier torque and flux equations, the block diagram of the proposed matrix converter based DTC scheme for IM drive is shown in Figure 3-3. By estimating the electromagnetic torque and flux through $\overline{e_o}$ *and* $\overline{\imath_o}$, the value of $\widehat{\psi_s}$ and $T_e$can be calculated which should be applied to H_{T_e} *and* H_ψ. Likewise, by estimating $< \sin\Phi_i >$ through the $\overline{e_\imath}$ *and* $\overline{\imath_\imath}$, the obtained value should be applied on the hysteresis of H_Φ. The switching algorithm of MC is configured by the value of $\overline{e_\imath}$, $\widehat{\psi_s}$, H_{T_e}, H_ψ and $\overrightarrow{\psi_s}$.

The direct matrix converter as shown in Figure 3-4(a) is of the highest practical interest as it connects a three-phase voltage source with a three-phase load (typically a motor). There are 27 possible switching configurations, but only 21 of them are useful in DTC algorithm, which are given in Table 3-1. Figure 3-4(b) shows the first 18 active voltage vectors having fixed directions. As shown in Table 3-1, the magnitudes of voltage vectors depend on the input voltages. The fourth and fifth columns of Table 3-1 show real

(α) and imaginary (β) components of the matrix converter's output voltage vectors in stationary reference frame. The last three switching configurations correspond to zero-output voltage vectors.

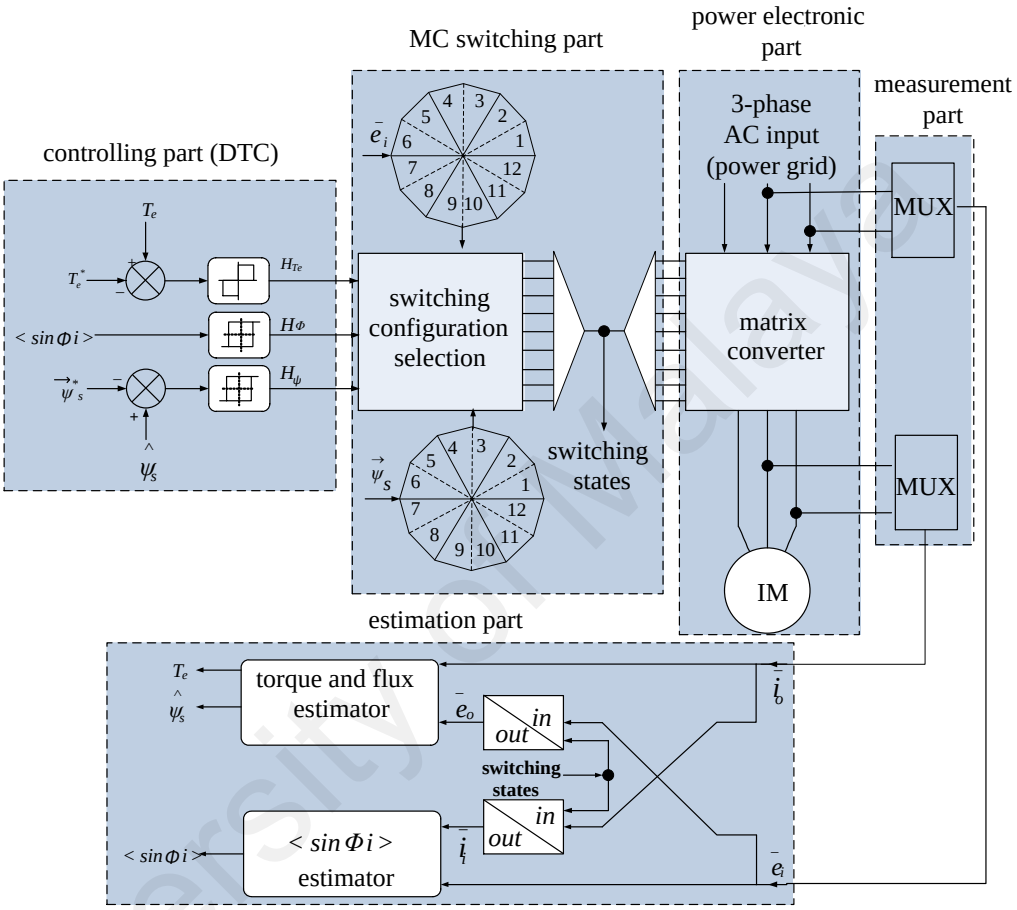

Figure 3-3: Block diagram of the proposed DTC based switching strategy by matrix converter.

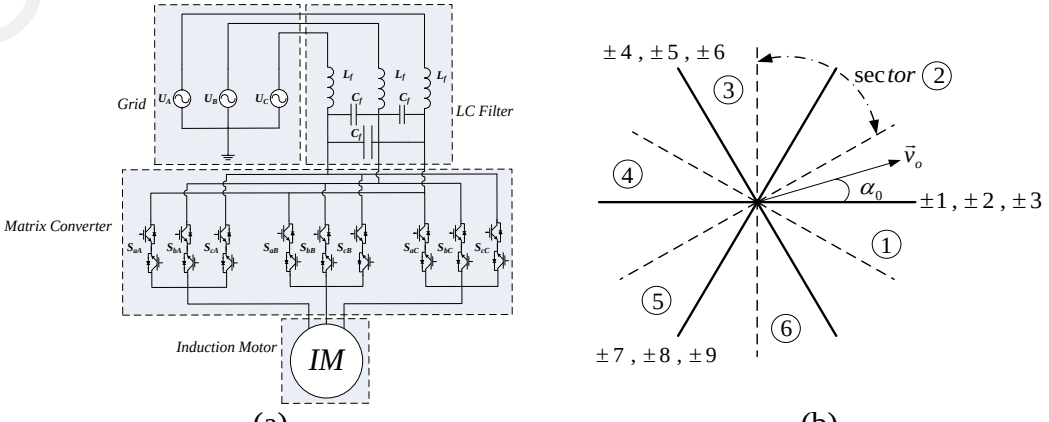

(a) (b)

Figure 3-4: (a) direct matrix converter configuration (b) active voltage vectors produced by matrix converter

Table 3-1: 3×3 matrix converter switching configuration.

switching combinations	on switches			voltage-vector values		αcomponent value	β component value
				v_o	α_o		
+1	S_{Aa}	S_{Bb}	S_{Bc}	$2/3v_{AB}$	*0*	$2/\sqrt{3}V_m\cos(\omega t+\pi/6)$	*0*
-1	S_{Ba}	S_{Ab}	S_{Ac}	$-2/3v_{AB}$	*0*	$-2/\sqrt{3}V_m\cos(\omega t+\pi/6)$	*0*
+2	S_{Ba}	S_{Cb}	S_{Cc}	$2/3v_{BC}$	*0*	$2/\sqrt{3}V_m\cos(\omega t-\pi/2)$	*0*
-2	S_{Ca}	S_{Bb}	S_{Bc}	$-2/3v_{BC}$	*0*	$-2/\sqrt{3}V_m\cos(\omega t-\pi/2)$	*0*
+3	S_{Ca}	S_{Ab}	S_{Ac}	$2/3v_{CA}$	*0*	$2/\sqrt{3}V_m\cos(\omega t+5\pi/6)$	*0*
-3	S_{Aa}	S_{Cb}	S_{Cc}	$-2/3v_{CA}$	*0*	$-2/\sqrt{3}V_m\cos(\omega t+5\pi/6)$	*0*
+4	S_{Ba}	S_{Ab}	S_{Bc}	$2/3v_{AB}$	$2\pi/3$	$-1/\sqrt{3}V_m\cos(\omega t+\pi/6)$	$V_m\cos(\omega t+\pi/6)$
-4	S_{Aa}	S_{Bb}	S_{Ac}	$-2/3v_{AB}$	$2\pi/3$	$1/\sqrt{3}V_m\cos(\omega t+\pi/6)$	$-V_m\cos(\omega t+\pi/6)$
+5	S_{Ca}	S_{Bb}	S_{Cc}	$2/3v_{BC}$	$2\pi/3$	$-1/\sqrt{3}V_m\cos(\omega t-\pi/2)$	$V_m\cos(\omega t-\pi/2)$
-5	S_{Ba}	S_{Ca}	S_{Bc}	$-2/3v_{BC}$	$2\pi/3$	$1/\sqrt{3}V_m\cos(\omega t-\pi/2)$	$-V_m\cos(\omega t-\pi/2)$
+6	S_{Aa}	S_{Cb}	S_{Ac}	$2/3v_{CA}$	$2\pi/3$	$-1/\sqrt{3}V_m\cos(\omega t+5\pi/6)$	$V_m\cos(\omega t+5\pi/6)$
-6	S_{Ca}	S_{Ab}	S_{Cc}	$-2/3v_{CA}$	$2\pi/3$	$1/\sqrt{3}V_m\cos(\omega t+5\pi/6)$	$-V_m\cos(\omega t+5\pi/6)$
+7	S_{Ba}	S_{Bb}	S_{Ac}	$2/3v_{AB}$	$4\pi/3$	$-1/\sqrt{3}V_m\cos(\omega t+\pi/6)$	$-V_m\cos(\omega t+\pi/6)$
-7	S_{Aa}	S_{Ab}	S_{Bc}	$-2/3v_{AB}$	$4\pi/3$	$1/\sqrt{3}V_m\cos(\omega t+\pi/6)$	$V_m\cos(\omega t+\pi/6)$
+8	S_{Ca}	S_{Cb}	S_{Bc}	$2/3v_{BC}$	$4\pi/3$	$-1/\sqrt{3}V_m\cos(\omega t-\pi/2)$	$-V_m\cos(\omega t-\pi/2)$
-8	S_{Ba}	S_{Bb}	S_{Cc}	$-2/3v_{BC}$	$4\pi/3$	$1/\sqrt{3}V_m\cos(\omega t-\pi/2)$	$V_m\cos(\omega t-\pi/2)$
+9	S_{Aa}	S_{Ab}	S_{Cc}	$2/3v_{CA}$	$4\pi/3$	$-1/\sqrt{3}V_m\cos(\omega t+5\pi/6)$	$-V_m\cos(\omega t+5\pi/6)$
-9	S_{Ca}	S_{Cb}	S_{Ac}	$-2/3v_{CA}$	$4\pi/3$	$1/\sqrt{3}V_m\cos(\omega t+5\pi/6)$	$V_m\cos(\omega t+5\pi/6)$
0_A	S_{Aa}	S_{Ab}	S_{Ac}	*0*	...	*0*	*0*
0_B	S_{Ba}	S_{Bb}	S_{Bc}	*0*	...	*0*	*0*
0_C	S_{Ca}	S_{Cb}	S_{Cc}	*0*	...	*0*	*0*

3.2.2 Effect of Voltage Vector on Flux and Torque

3.2.2.1 Effect of voltage-vector on flux

The IM parameters used for simulation are shown in Table 3-2,which is a three phase 380V-50Hz IM with 1.1 kV power and the rated torque of 6.3Nm. The rated current of this motor is 2.6A which can provide the rated speed of 1473rpm.

For flux variation in different voltage vectors, α and β components of each vector were substituted based on per-unit, and equations obtained. e.g., voltage vector of first order in (+)ve region is obtained from:

$$v_{+1} = \frac{2}{3} v_{AB} \angle 0 = \frac{2}{3}(v_A - v_B).(\cos(0) + j\sin(0)) \qquad 3\text{-}26$$

Equation 3-26 converted into per-unit based on machine's rated voltage (V_{base}); the α and β components of v_{+1} yields:

$$\begin{cases} v_{+1\alpha,pu} = \dfrac{v_{+1\alpha}}{V_m} = \dfrac{2}{\sqrt{3}} \cos\left(\omega t + \dfrac{\pi}{6}\right) \\ v_{+1\beta,pu} = 0 \end{cases} \qquad 3\text{-}27$$

From 3-22 and 3-27 the flux variation can be obtained as:

$$\Delta\left|\vec{\psi}_s\right|_{pu,+1} = \frac{2}{\sqrt{3}} \cdot \left(\cos\left(\omega t + \pi/6\right) \times \cos\theta_1\right) \cdot \left(120\pi\right) \times 10^{-6} \qquad 3\text{-}28$$

In 3-28, rated frequency of motor is considered as *50Hz*, and sampling time-interval is considered *1μs*. The comparison of stator flux variation between the conventional (60° sector) and the proposed (30° sector) switching schemes is shown in Figure 3-5 and Figure 3-6, respectively. As can be seen in Figure 3-5(a) and Figure 3-6(a), the peak-to-peak flux variation in both conventional and proposed switching scheme is the same. However, there is 180° phase difference between Figure 3-5(a) and Figure 3-6(a) by applying voltage vectors v_{+1} and v_{-1}, respectively. In Figure 3-5(b) the color area indicates the (+)ve ($\Delta\left|\vec{\psi}_s\right|_{pu} \geq 0$) variation and white area indicates the (-)ve ($\Delta\left|\vec{\psi}_s\right|_{pu} < 0$) variation of stator

flux. Note that in some sectors, applying the voltage vector when the space vector is divided into six 60° sectors is impossible because the flux increases and decreases at the same time in the sectors. For example, (when $\omega t < 120°$ and $60° < \theta < 120°$), flux in one half of this sector is positive which means that v_{+1} increases the stator flux while in the other half it is negative which means that v_{+1} decreases the stator flux. So, the use of v_{+1} in this sector is not allowed. Hence, for the conventional switching scheme the degree of freedom to choose the stator-voltage vector is limited.

Table 3-2 : Specifications and parameters of the 3-phase test induction-motor, referred to the stator side.

rated power	S	*1100 VA*
rated torque	$T_{e,\,base}$	*6.3 Nm*
rated voltage	$V_{l\text{-}l}$	*380 V*
number of poles	$2P$	*2*
rated frequency	f	*50 Hz*
stator resistance	R_s	*21.405* Ω
stator reactance	X_{ls}	*1.842* Ω
mutual reactance	X_m	*54.09* Ω
rotor resistance	R'_r	*22.395* Ω
rotor reactance	X'_{lr}	*1.834* Ω
friction factor	J	*0.0131 kg/m²*

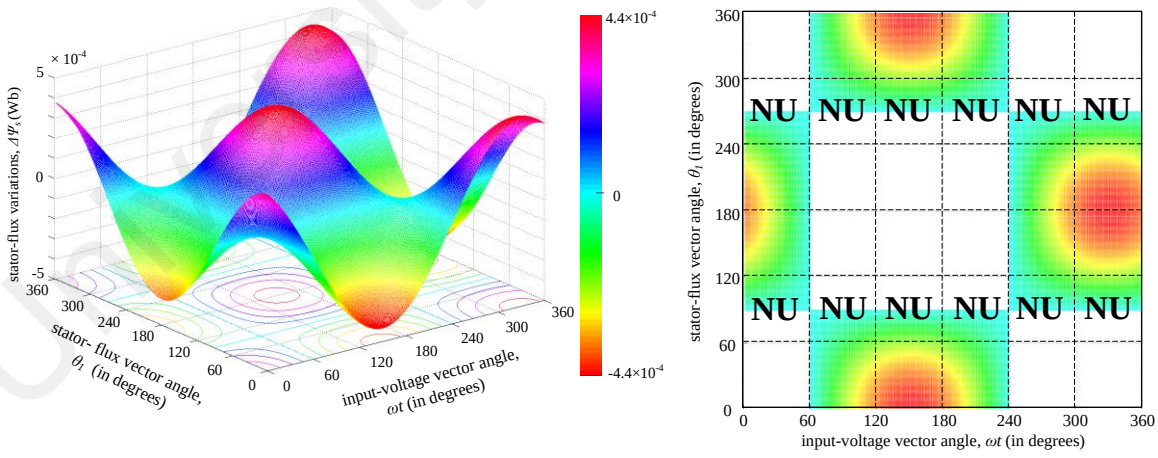

(a) (b)

Figure 3-5: Stator-flux vector variation of conventional (60° sector) DTC scheme under the rated condition of the motor for v_{+1} (NU=No Use). (a) stator flux variation; (b) stator-flux vector behavior characteristic

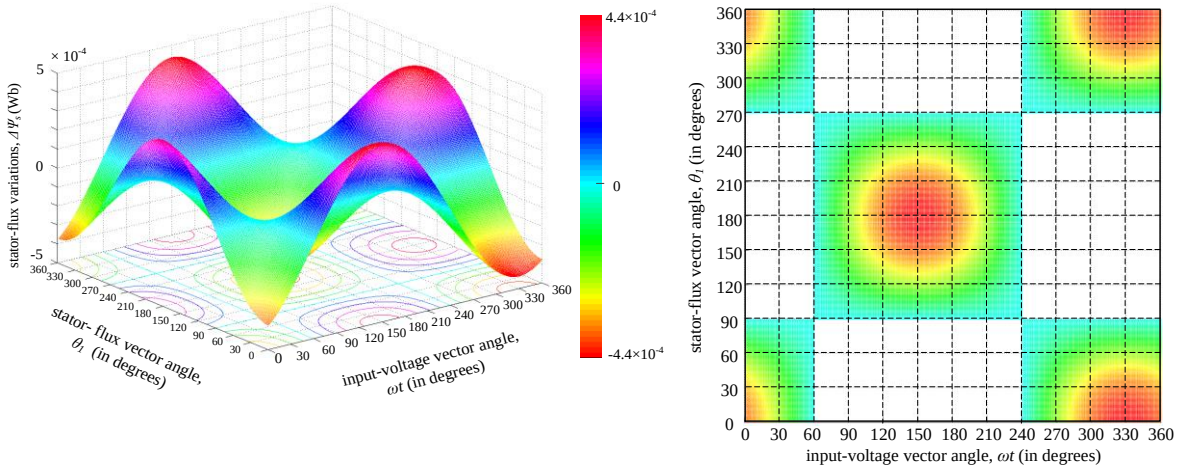

(a) (b)

Figure 3-6: Stator-flux vector variation of the proposed (30° sector) DTC scheme under rated condition of the motor for v_{-1}. (a) stator flux variation; (b) stator-flux vector behavior specific

Figure 3-6(b) shows flux vector variations of voltage vector v_{+1} for the proposed 30° sector based switching scheme. It is clearly seen from the figures that there is no sector when the flux is increasing and decreasing simultaneously. Thus, the stator-voltage vector can be applied for each sector for the proposed 30° sector scheme. Hence, the degrees of freedom to choose the stator-voltage vector with the proposed 30° sector switching scheme is increased significantly as compared the conventional 60° sector scheme. For stator-voltage vector v_{-1}, the stator flux variation is exactly opposite to that of voltage vector v_{+1}. This statement is true for all stator-voltage vectors (e.g., v_{+5} and v_{-5}, etc.)

Figure 3-7 compares instantaneous basic voltage vectors of the proposed (30°- sector) method with the conventional (60°-sector) method. As it is evident in Figure 3-7, the magnitude of voltage vector for the proposed scheme is always higher than or at least equal to that of conventional scheme. Thus, the voltage ripple could be reduced with the proposed scheme. Moreover, the probability of stator voltage reference transgress during large torque demand may reduce because the voltage reference vector limitations are enclosed by 12-side polygonal rather than hexagonal boundary. According to Figure 3-7 the maximum value of reference voltage vector for 12-side polygonal space vector is $V_{sm2} = r\cos(\vartheta)$, and the maximum value of reference voltage vector for hexagonal

boundary is $V_{sm1} = r \cos(\frac{\vartheta}{2})$. While $\vartheta = \pi/6$, the maximum value of reference voltage vector for 12-side polygonal space vector is $V_{sm2} = 1.11\ (V_{sm1})$.

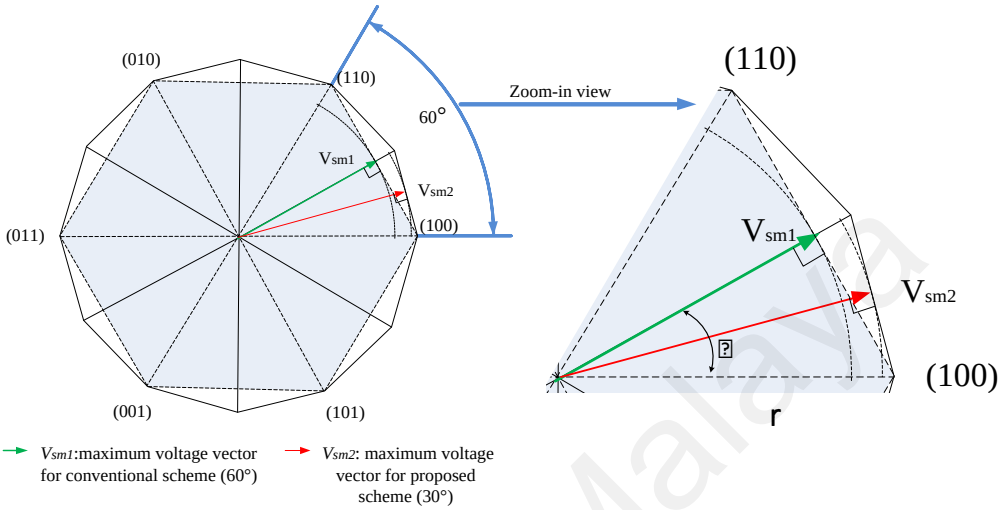

Figure 3-7: Instantaneous basic voltage vectors for both conventional (60° sector) and proposed (30° sector) switching scheme, and the zoom-in view of the first sector.

3.2.2.2 Effect of voltage-vector on torque

Torque variation by applying vectors v_{+1} and v_{+2} are shown in Figure 3-8(a) and Figure 3-8(c), respectively, for the proposed switching scheme. It is clearly seen from the figures that the torque variation not defected when the voltage vector switches from v_{+1} to v_{+2}. The corresponding torque variations on θ_1-ωt plane are shown in Figure 3-8(b) and Figure 3-8(d), respectively. In Figure 3-8(b) and Figure 3-8(d) two color peristyles indicate the (+)ve torque variation and the white area indicates the (-)ve torque variation. The area of color regions is the same in both Figure 3-8(b) and Figure 3-8(d) except their positions are changed.

With the application of various voltage vectors, there is no additional torque variation. It means that with applying a different voltage vector, the torque ripple remains constant. It is found that the developed torque of the motor is stable at different load and speed conditions. Additionally, it is clearly seen from the figures that the torque for v_{+1} and v_{+2} have same space-dependent expression, and for time-dependent expression. The torque

variation by applying vectors v_{+2} lags the torque variation as a result of applying v_{+1} by $\pi/3$.

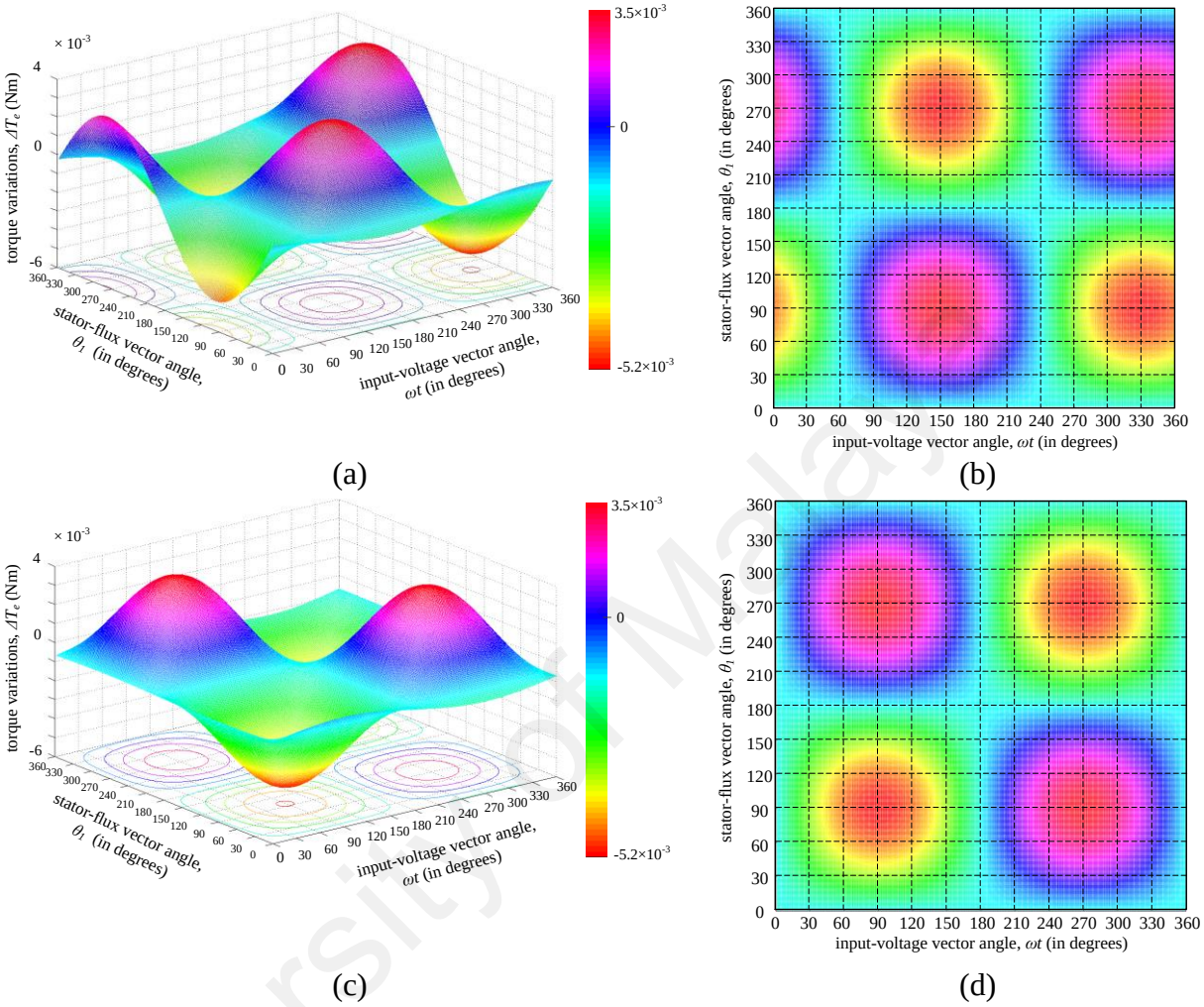

Figure 3-8: Torque variation for the proposed (30° sector) DTC based IM drive under the rated condition of the motor. (a) torque variation for voltage vector v_{+1}; (b) torque behavior characteristic for v_{+1}; (c) torque variation for voltage vector v_{+2}; (d) torque behavior characteristic for v_{+2}

3.2.3 Vectors suitable for control

To examine the effect of *18* active voltage vectors produced by the matrix converter on the flux and torque, a procedure similar to that applied for v_{+1} is applied. Voltage vectors with stable characteristic in the *30°* sectors are then chosen as suitable for control of motor torque and flux. Based on the earlier result analysis, the proposed switching technique is extracted, and shown in Table 3-3. H_{φ} and H_{Te} are the outputs of flux and torque hysteresis controllers, respectively, as shown below:

$$\begin{cases} T_e < T_e^*, H_{T_e} = +1 \\ T_e > T_e^*, H_{T_e} = -1 \end{cases} \quad \text{3-29}$$

$$\begin{cases} \varphi < \varphi^*, H_{\varphi} = +1 \\ \varphi > \varphi^*, H_{\varphi} = -1 \end{cases} \quad \text{3-30}$$

Table 3-3 is produced for the stator flux in the first and the second sectors, but owing to symmetry conditions in space vector the results are valid also for the remaining sectors. It should be noted, $H_{\varphi}=+1$ indicates,which the flux needs to increase. $H_{\varphi}=-1$ indicates that the flux needs to decrease. Similarly, $H_{Te}= +1$ indicates that the torque needs to increase and $H_{Te}= -1$ indicates the torque needs to decrease. Table 3-3 lists the results for the first *six* sectors of the input voltage. The results for the remaining *6* sectors shows, (the first 6 sectors), e.g., in 7th sector (L=7) the voltage vector is -9 while, the voltage vector is *+9* in the first voltage sector (*L=1*) and this logic is true for all remaining sectors (*L=7,8,9,…,12*).

Table 3-3: Degrees of freedom in selecting appropriate voltage vector for the proposed DTC scheme.

proper vectors for k as an odd number ($k = 1,3,5,7,9,11$)				
H_φ	+1		-1	
H_{Te}	+1	-1	+1	-1
L=1	(3k+9)/2	(3k-1)/2 , (3k+1)/2 , (3k+33)/2 , (3k+3)/2 , (3k+29)/2 , (3k+31)/2	(3k+15)/2	(3k+23)/2 , (3k+25)/2 , (3k+19)/2 , (3k+27)/2
L=2	(3k+9)/2	(3k-1)/2 , (3k+1)/2 , (3k+33)/2 , (3k+3)/2 , (3k+29)/2 , (3k+31)/2	(3k+15)/2	(3k+23)/2 , (3k+25)/2 , (3k+17)/2 , (3k+27)/2
L=3	(3k+7)/2	(3k+1)/2 , (3k+11)/2 , (3k+33)/2 , (3k+17)/2 , (3k+3)/2 , (3k+31)/2	(3k+13)/2	(3k-1)/2 , (3k+25)/2 , (3k+5)/2 , (3k+27)/2
L=4	(3k+7)/2	(3k+1)/2 , (3k+11)/2 , (3k+33)/2 , (3k+17)/2 , (3k+3)/2 , (3k+31)/2	(3k+13)/2	(3k+21)/2 , (3k+25)/2 , (3k+5)/2 , (3k+27)/2
L=5	(3k+23)/2	(3k+1)/2 , (3k+21)/2 , (3k+11)/2 , (3k+17)/2 , (3k+31)/2 , (3k+15)/2	(3k+29)/2	(3k+25)/2 , (3k+9)/2 , (3k+3)/2 , (3k+5)/2
L=6	(3k+23)/2	(3k+1)/2 , (3k+21)/2 , (3k+11)/2 , (3k+17)/2 , (3k+31)/2 , (3k+15)/2	(3k+29)/2	(3k+25)/2 , (3k+9)/2 , (3k+19)/2 , (3k+5)/2
proper vectors for k as an even number ($k = 2,4,6,8,10,12$)				
H_φ	+1		-1	
H_{Te}	+1	-1	+1	-1
L=1	(3k+8)/2 (3k+12)/2	(3k-4)/2 , (3k-2)/2 , 3k/2	-	(3k+2)/2 , (3k+20)/2 , (3k+22)/2 , (3k+26)/2 , (3k+28)/2 , (3k+24)/2
L=2	(3k+10)/2 (3k+12)/2	(3k-4)/2 , (3k-2)/2 , 3k/2	-	(3k+2)/2 , (3k+20)/2 , (3k+22)/2 , (3k+26)/2 , (3k+28)/2 , (3k+24)/2
L=3	(3k+10)/2 (3k+12)/2	(3k-2)/2 , (3k+14)/2 , 3k/2	-	(3k+8)/2 , (3k+30)/2 , (3k+22)/2 , (3k+28)/2 , (3k+2)/2 , (3k+24)/2
L=4	(3k+10)/2 (3k+26)/2	(3k-2)/2 , (3k+14)/2 , 3k/2	-	(3k+8)/2 , (3k+30)/2 (3k+22)/2 , (3k+28)/2 , (3k+2)/2 , (3k+24)/2
L=5	(3k+10)/2 (3k+26)/2	(3k-2)/2 , (3k+18)/2 , (3k+14)/2	-	(3k+8)/2 , (3k+22)/2 , (3k+6)/2 , (3k+28)/2 , (3k+12)/2 , (3k+2)/2
L=6	(3k+30)/2 (3k+26)/2	(3k-2)/2 , (3k+18)/2 , (3k+14)/2	-	(3k+8)/2 , (3k+22)/2 , (3k+6)/2 , (3k+28)/2 , (3k+12)/2 , (3k+2)/2

Table 3-4 shows the switching scheme codes corresponding to each voltage vector.

Table 3-4: Matrix converter switching status for proposed switching scheme.

switching code	*vector number*	*on switches*			*equivalent vector code in odd sectors*	*equivalent vector code in even sectors*
1	v_{+1}	S_{Aa}	S_{Bb}	S_{Cb}	*(3k-1)/2*	*(3k-4)/2*
2	v_{+2}	S_{Ab}	S_{Bc}	S_{Cc}	*(3k+1)/2*	*(3k-2)/2*
3	v_{-3}	S_{Aa}	S_{Bc}	S_{Cc}	*(3k+3)/2*	*3k/2*
4	v_{-7}	S_{Aa}	S_{Ba}	S_{Cb}	*(3k+5)/2*	*(3k+2)/2*
5	v_{-8}	S_{Ab}	S_{Bb}	S_{Cc}	*(3k+7)/2*	*(3k+4)/2*
6	v_{+9}	S_{Aa}	S_{Ba}	S_{Cc}	*(3k+9)/2*	*(3k+6)/2*
7	v_{+4}	S_{Ab}	S_{Ba}	S_{Cb}	*(3k+11)/2*	*(3k+8)/2*
8	v_{+5}	S_{Ab}	S_{Bb}	S_{Cc}	*(3k+13)/2*	*(3k+10)/2*
9	v_{-6}	S_{Ab}	S_{Ba}	S_{Cc}	*(3k+15)/2*	*(3k+12)/2*
10	v_{-1}	S_{Ab}	S_{Ba}	S_{Ca}	*(3k+17)/2*	*(3k+14)/2*
11	v_{-2}	S_{Ac}	S_{Bb}	S_{Cb}	*(3k+19)/2*	*(3k+16)/2*
12	v_{+3}	S_{Ab}	S_{Ba}	S_{Ca}	*(3k+21)/2*	*(3k+18)/2*
13	v_{+7}	S_{Ab}	S_{Bb}	S_{Ca}	*(3k+23)/2*	*(3k+20)/2*
14	v_{+8}	S_{Ab}	S_{Bc}	S_{Cb}	*(3k+25)/2*	*(3k+22)/2*
15	v_{-9}	S_{Ab}	S_{Bc}	S_{Ca}	*(3k+27)/2*	*(3k+24)/2*
16	v_{-4}	S_{Aa}	S_{Bb}	S_{Ca}	*(3k+29)/2*	*(3k+26)/2*
17	v_{-5}	S_{Ab}	S_{Bc}	S_{Cb}	*(3k+31)/2*	*(3k+28)/2*
18	v_{+6}	S_{Aa}	S_{Bc}	S_{Ca}	*(3k+33)/2*	*(3k+30)/2*
19	0_a	S_{Aa}	S_{Ba}	S_{Ca}	*19*	*19*
20	0_b	S_{Ab}	S_{Bb}	S_{Cb}	*20*	*20*
21	0_c	S_{Ac}	S_{Bc}	S_{Cc}	*21*	*21*

A special code is developed for each switching state of the matrix converter to determine similar vectors in the other sectors with the first ($L=1$) and second ($L=2$) sectors, as shown in Table 3-4. For example, in order to find the equivalent voltage vector in stator-flux sector five ($k=5$) for voltage vector v_{+2} at the first stator-flux sector ($k=1$), switching code no. 2 is first found from Table 4, then substituting $k=5$ in the corresponding equation yields:

$$(3k+1)/2 = (3\times5+1) = 8$$

Code *8* shows the 8^{th} row of Table 3-4, meaning that voltage vector v_{+5} has equal influence on flux and torque similar to voltage vector v_{+2} at the first stator-flux sector. Again, if the voltage vector is v_{+2}, and the stator flux sector is $k=2$, then in sector $k=4$, the

equivalent voltage vector is v_{-8}. Furthermore, if the voltage vector is v_{-6}, and the stator flux sector is $k=2$, then the equivalent vector code becomes: $(3k+12)/2= (3\times12+12)/2=24$.

If the obtained code is bigger than 18, the valid switching code is achieved by subtracting 18 from the calculated number: $24-18=6$

Hence, from Table 3-4, the switching code number 6, is equivalent to voltage vector v_{+9} in $k=12$.

3.2.4 Selection of optimum vectors to minimize the switching losses

As can be seen from Table 3-3, there are multiple vectors for switching selection in some sectors, which increases the degrees of freedom in selection of space-vector voltage for DTC of IM by matrix converter.

The enhanced degrees of freedom improve the IM drive performance. In addition, the proposed 12-sector switching method is independent of the load and speed variation, to explain the "no use" sectors which are included in Table 3-3 when k is equal to an even number, H_{φ}=-1 and H_{Te}=+1. These redundancies of vectors for switching selection provide an additional option, to optimize the switching losses by proposed 12-sector method compares to the conventional switching. While the switching is fixed in conventional method and there is no redundancy of vectors for switching selection, the proposed method can provide the optimum switching losses due to exist of multiple vectors for switching selection.

In order to obtain minimum switching frequency, which provides optimum switching loss, the space-vector voltage with lowest flux variation is selected from Table 3-5 as the best switching vector. This selection increases the switching period by extending time to reach the hysteresis band in both flux and torque. Accordingly, the switching frequency is optimized hence the switching losses are diminished. The lowest

average values in each sector of the contour-map are chosen for switching by comparing the variation rates of the flux correspond to each input voltage in different flux sectors.

Table 3-5: Impact factor of the flux variation (IF_λ) for v_{+1} and the enhanced table for all 18 active voltage vectors.

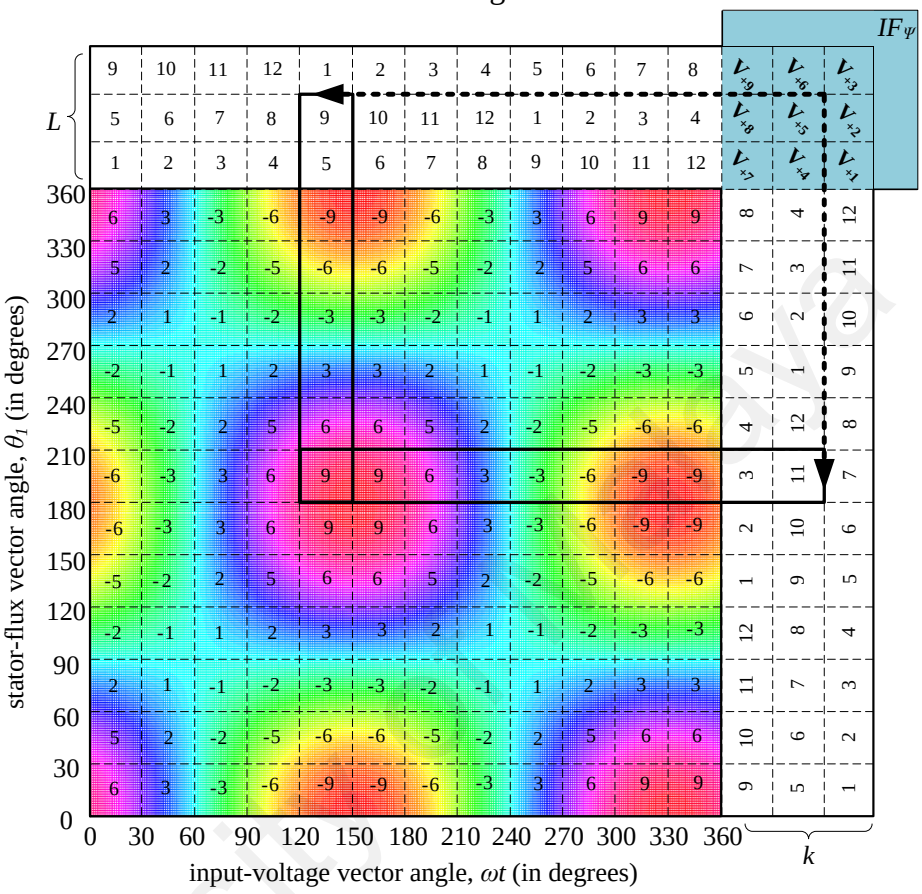

The average value of the flux in each sector in the contour maps is calculated as follows:

$$IF_\psi = \text{round}\left[\frac{R_F}{(\pi/6)^2}\int_{\frac{T}{12}(L-1)}^{\frac{T}{12}(L)}\int_{\frac{\pi}{6}(k-1)}^{\frac{\pi}{6}k}\Delta\left|\vec{\psi}_s\right| d\theta\ d\omega t\right] \qquad 3\text{-}31$$

Where, round of Eq. 3 31 denotes the rounding of the number to the nearest integer, and IF_ψ is the impact factor of flux. The values of IF_ψ are integers between -9 and +9 when the coefficient R_F is equal to 4.4×10^{-3} .

Substituting 3-27into 3-31, the IF_ψ of v_{+1} vector in each zone can be calculated. The enhanced switching table of v_{+1} vector can be established as presented in Table 3-5, in which the effects of v_{+1} switching state on flux variations are shown explicitly over its

corresponding contour map. Due to the symmetry for the voltage vectors, the results in Table 3-5 are extended for all 18 vectors.

3.3 Z-source Inverter and Voltage Transfer Ratio Calculation

The major reason for applying a z-source into the USZSMC is related to utilizing the boosting particularity to a higher range of output voltage. When the expected switching frequency is at least five time bigger than the fundamental frequency of the input voltage, the Z-source inverter (ZSI) is stable and could be considered to be a constant DC source voltage at the specific operating point for each unique modulation index.

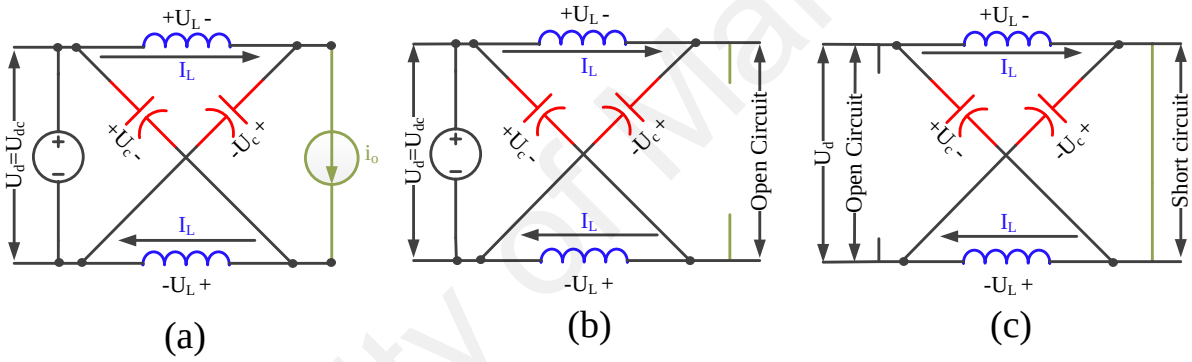

Figure 3-9: Z-source network in mode of (a) dynamic non-shoot-through, (b) inactive non-shoot-through, and (c) shoot-through states

The ZSI works primarily in two distinctive functioning modes: first across the normal operating mode or non-shoot-through state, where the accumulated power is applied into corporate output voltage. Moreover, a steady DC-link voltage delivers the ZSI within a switching period. In Figure 3-9(a), a current source as the output of the Z-source system demonstrates a limited current flow, while Figure 3-9(b) under the same input DC voltage is an open circuit. Meanwhile, in Figure 3-9(c) the output of the z-source network is shorted where the high current flows through the circuit, and, simultaneously, the DC supply for the network is zero. In the shoot-through state, the Z-source network stores the inductive and capacitive power with its elements. The third approach occurs when two

switches from the same leg of the inverter are ON (as pattern Sv_1&Sv_4, Sv_3&Sv_6, and Sv_5&Sv_2) in the VSI part of Figure 3-1.

Assuming that inductors L_1 and L_2 have the same inductance L, and capacitors C_1 and C_2 also have the same capacitance C, the Z-source network becomes symmetrical. From symmetry, we have

$$U_{L1} = U_{L2} = U_L$$
$$U_{C1} = U_{C2} = U_C \qquad 3\text{-}32$$

The timing of the non-shoot-through state modes have been defined with T_1. During this period, the normal operation of the Z-source inverter can be seen in the circuit and the DC-link of rectifier has been connected to the Z-source network. Figure 3-9(a and b) show the equivalent circuit, which has the following voltage relationships:

$$U_L = U_{dc} - U_C , U_d = U_{dc} , U_i = U_C - U_L = 2U_C - U_{dc} \qquad 3\text{-}33$$

The timing of the shoot-through state mode has been defined by T_0, the circuit of the Z-source inverter stage is shorted intentionally, and, at the same time, the DC-link is opened, which separates the CSR from the DC-link. The rectifier operates the commutation as mentioned earlier during this period. The shoot-through in seven various modes could be gained when any single leg of the inverter, couple of legs, or triple legs are shorted. Charging the energy in the Z-source network has been combined with producing a zero shoot-through state. As can be seen in Figure 3-9(c), the voltage relationships are as follows,

$$U_L = U_C , U_d = 2U_C , U_i = 0 \qquad 3\text{-}34$$

The first consideration for deriving the theoretical principles of the voltage transfer ratio is the inductor current in the Z-source network. Based on the conjugation of (32), the current across both inductors should be symmetrical and the same inductivity needs

to be applied to both of them. The expression for the current across the inductor at the end of the shoot-through state is:

$$I_L = \frac{1}{L}\int_0^{T_0} U_L \, dt + I_{L0} \qquad 3\text{-}35$$

where the initial current at time 0 is assumed to be I_{L0}. Moreover, the expression of the inductive current of z-source network at the end of non-shoot-through state is extracted as:

$$I_L' = \frac{1}{L}\int_{T_0}^{T_0+T_1} U_L' \, dt + I_{L0}' \qquad 3\text{-}36$$

where the initial current for the inductor is assumed to be I_{L0}' at time T_0. If we suppose U_L is constant in the 3-35 and 3-36 interval integration, the current variation in the shoot-through and non-shoot-through mode can be extracted by:

$$\Delta I_L = \frac{U_L}{L} T_0 = \frac{U_c}{L} T_0$$
$$\Delta I_L' = \frac{U_L}{L} T_1 = \frac{(U_{dc} - U_c)}{L} T_1 \qquad 3\text{-}37$$

On the other hand, the switching period is assumed to be T, where $T_0 + T_1 = T$, and, during the switching period in the steady state mode, the average voltage of the inductor is moderated by keeping close to zero; hence, we have:

$$\Delta I_L + \Delta I_L' = \frac{U_c}{L} T_0 + \frac{(U_{dc} - U_c)}{L} T_1 \qquad 3\text{-}38$$

$$U_c = \frac{T_1}{T_1 - T_0} U_{dc} \qquad 3\text{-}39$$

During the non-shoot-through state, when T_1 is greater than or equal to T_0, the voltage U_i across the inverter bridges can be expanded based on 3-33 and 3-39 into:

$$U_i = 2U_C - U_{dc} = 2\left(\frac{T_1}{T_1 - T_0}\right)U_{dc} - U_{dc} = \frac{T}{T_1 - T_0}U_{dc}$$

3-40

$$BF_t = \frac{U_i}{U_{dc}} = \frac{T}{T_1 - T_0}$$

The time-based boost factor (BF_t) is determined in 3-40. On the other hand, based on the symmetrical properties of the Z-source network and 3-32, we not only have the same equations for current, but also the ratio for the inductive to capacitive current of Z-source has been kept load dependent, as can be seen in following relations:

$$\begin{cases} I_{c_1}(s) = I_{c_2}(s) = I_C(s) \ , \quad I_{l_1}(s) = I_{l_2}(s) = I_L(s) \\ I_L(s) - I_C(s) = I(s) \\ \dfrac{\frac{1}{cs} + Z}{Ls + Z} = \dfrac{I_L(s)}{I_C(s)} \end{cases}$$

3-41

where Z has been assumed to be the equivalent load of the connected IM rear-end Z-source inverter in complex frequency (S-domain). Therefore, with the same strategy for the conjugate properties of voltage, expectations can be extracted by:

$$U_{dc}(s) = \begin{cases} \dfrac{2}{cs}I_C(s) - ZI(s) \\ \dfrac{1}{cs}I_C(s) + LsI_L(s) \\ 2LsI_L(s) + ZI(s) \end{cases}$$

3-42

So,

$$\begin{gathered} \frac{I_L(s)}{U_{dc}} = \frac{ZCS + 1}{ZLCS^2 + 2LS + Z} \\ \rightarrow \frac{I_C(s)}{U_{dc}} = \frac{LCS^2 + ZCS}{ZLCS^2 + 2LS + Z} \\ \rightarrow Z\left(\frac{I_L(s)}{U_{dc}} - \frac{I_C(s)}{U_{dc}}\right) = \left(\frac{1 - LCS^2}{ZLCS^2 + 2LS + Z}\right)Z \end{gathered}$$

3-43

In contrast the boost factor that is normally defined by $\frac{U_i}{U_{dc}}$ which is independent from the Z-source output and consequently from input grid power and dependent to induction motor elements as:

$$BF_c = \frac{U_i(s)}{U_{dc}(s)} = \frac{ZI(s)}{U_{dc}(s)} = \frac{1 - LCS^2}{LCS^2 + 2\frac{LS}{Z} + 1} \quad 3\text{-}44$$

where the roots of numerator and denominator are the zeroes and poles respectively:

$$\text{zeros: } \pm\frac{1}{\sqrt{LC}} \quad 3\text{-}45$$

$$\text{poles: } \frac{-\frac{L}{Z} \pm \sqrt{\left(\frac{L}{Z}\right)^2 - LC}}{\sqrt{LC}} \quad 3\text{-}46$$

Equation 3-45 shows the system zeros are real and placed on x-axis only. The equation also yields zeros are depended on the z-source inductance and capacitor values only. The zeros of system converge to the same value of zero as the LC increases to infinity, where they get apart and tend to infinity as the LC goes to zero.

Assuming the Z-source inductance and capacitor are preselected and constant during the implementation, the system poles are depended on the load. Considering the load starts from very small value close zero (*Z≈0*), the (L/Z) predominate 3-46, so it could be rewritten as follows:

$$\text{poles: } \left(-\left(\frac{L}{Z}\right) \mp \left(\frac{L}{Z}\right)^{-}\right) * \left(\frac{1}{\sqrt{LC}}\right) \quad 3\text{-}47$$

$$\Rightarrow \text{poles: } \begin{matrix} p_1: -\left(\frac{L}{Z}\right) + \left(\frac{L}{Z}\right)^{-} \rightarrow 0^{-} \\ p_2: \left(\left(-\frac{L}{Z}\right) - \left(\frac{L}{Z}\right)\right) * \left(\frac{1}{\sqrt{LC}}\right) \approx -2\left(\frac{L}{Z}\right) * \left(\frac{1}{\sqrt{LC}}\right) \rightarrow -\infty \end{matrix} \quad 3\text{-}48$$

Equation above yields even disconnecting the load never leads the system into instability. As load increases from zero to $\sqrt{\frac{L}{C}}$, the system poles converge to -1. Proceeding increasing the load to infinity, $(\frac{L}{Z})$ descents to zero; thus 3-46could be simplified as follow:

$$\text{critical point of poles:}\frac{\pm\sqrt{-\mathrm{LC}}}{\sqrt{\mathrm{LC}}} = \pm\mathrm{i} \qquad 3\text{-}49$$

Equation 3-49 indicates the system is stable for a large variation of load type where the steady state response contains a persistent sinusoidal component $sin(t + \phi)$.

In order to increase the ratio of the boost factor, we have two approaches based on 3-40 and 3-44. First, increase the T_0 time and make it close to T_1; secondly, choose the value of L and C for drawing the poles to zero and approximating 3-44 to infinite. The second approach is a necessary condition for finding the Z-source values. In the other word, two approaches are plausible to increase the boost factor ratio. First, by increasing T_0 to near T_1 based on 3-40; second, determining L and C values in the way that the poles are drawn to zero based on 3-44. *To* determine the L and C, equation 3-44 should be plotted. This curve (Figure 3-10(a)) represents the relation between the Z-source element (L and C) and voltage transfer ratio, while Z is replaced with the value of the IM parameters detailed in Table 3-2. Hence, a persistent sinusoidal component ($sin(t+\varphi)$) can be observed.

On the other hand, sufficient and complementary second approach is the following:

$$\mathrm{C} \geq \frac{\mathrm{D_0 I_L}}{2\mathrm{R_1}\%\mathrm{U_c f_s}}$$

$$\mathrm{L} \geq \frac{\mathrm{D_0 U_c}}{2\mathrm{R_2}\%\mathrm{I_L f_s}} \qquad 3\text{-}50$$

where, D_0 is the shoot-through duty cycle and has been defined by T_0/T, $\mathrm{f_s}$ is the switching frequency. The ripple of capacitor voltage is shown as R_1 ($^{dU_c}/_{U_c}$) and inductive current as R_2 ($^{dI_L}/_{I_L}$) in percentage (Changliang & Xinmin, 2015; Shen, Joseph, Wang, Peng, & Adams, 2007; Xiong, Poh Chiang, Peng, & Xiaoqing, 2012). It means that satisfying inequality of 3-50 is the necessary condition for choosing the value of L and C, which

introduces boundaries for the L and C values as depicted in Figure 3-10(b), Figure 3-10(c) and Figure 3-10(d). Practically, the satisfying inequality of 3-50 is the necessary condition for choosing the value of L and C, which introduces boundaries for the L and C values as depicted in Figure 3-10(c) and Figure 3-10(d).

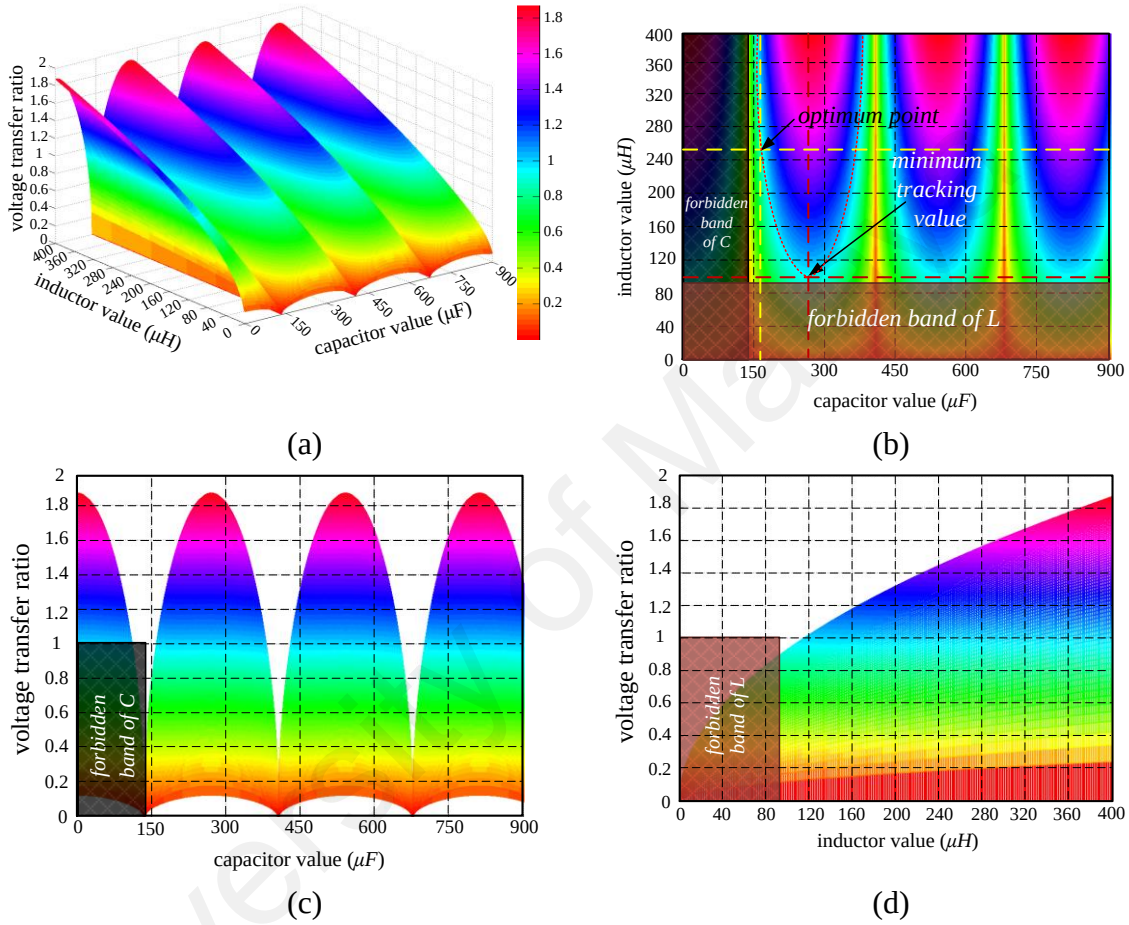

Figure 3-10: Variation of Z-source elements (a) voltage transfer ratio via C and L, (b) minimum tracking value of L and C, (c) forbidden band of C, (d) forbidden band of L.

In Figure 3-10(a), based on 3-44 we have the curve of the Z-source elements and their relationship with the voltage transfer ratio where the values of the inductors and capacitors are effective for the boost factor. Figure 3-10(b) shows the minimum tracking value of the elements according to 3-50 the condition under the stability margin of 3-44. It can be satisfied for load condition where the optimum point of C and L for chosen IM have been specified as 170μF and 250μH, respectively. They are achieved tentatively in order to have optimum performance, reliability, cost effectiveness, weight, and occupied

space. The unity voltage transfer ratio surface with capacitive and inductive value are shown in Figure 3-10(c) and Figure 3-10 (d), respectively.

Consequently, from Figure 3-10(b), it can be observed that the most optimum value of capacitor and inductor is around 270μF and100μH respectively. Since these values are not plausible, a feasible point should be determined from the tracking curve. As a result, the feasible point of L and C can be achieved under the load condition as 250μH and 170μF respectively. The values are obtained tentatively in order to reach maximized performance, reliability and cost effectiveness, while minimizing the weight and volume of the overall driver.

3.3.1 Optimum Control to Minimize the THD

The optimization problem that we consider here is motivated by the need to minimize the THD in the output current to a certain level. To achieve this, PSO is applied to the PI controllers to adjust the values.

PSO is an artificial intelligence method that can be used to find approximate solutions to extremely difficult or impossible problems. It has been proven to be both fast and effective when applied to a wide variety of optimization problems.

In PSO, the potential solutions are called particles, and, in terms of their exploration and exploitation, the particles of the swarm fly through hyperspace and have two essential reasoning capabilities:

1) The memory of their own best position or local best (l_b), which allows it to remember the best position in the feasible search space that has been visited, and
2) Knowledge of the global or their neighborhood's best or global best (g_b), which is the best value obtained so far by any particle in the neighborhood of the particle.

The position of each particle in the swarm is updated using the following equation:

$$x_{k+1}^{i} = x_{k}^{i} + v_{k+1}^{i} \quad 3\text{-}51$$

where *x* is the particle position and *v* is the particle velocity in the iteration *k*. The velocity is calculated as follows:

$$v_{k+1}^{i} = w \times v_{k}^{i} + c_1 r_1 (p_{k}^{i} - x_{k}^{i}) + c_2 r_2 (p_{k}^{g} - x_{k}^{i}) \quad 3\text{-}52$$

where, p_k^i is the best individual particle position and p_k^g is the best global position, c_1 and c_2 are the cognitive and social parameters, respectively; r_1 and r_2 are random numbers between 0 and 1. c_1 and c_2 are usually close to 2 and affect the size of the particle's step towards the individual best and global best, respectively. In this study, both values are assumed to be 2 in order to attract the particle towards the best points equally.

$c_2 r_2 (p_k^i - x_k^i)$ is called the social component, which causes the particle to tend to return to the best region the swarm has found so far and to follow the best neighbor's direction. If $c_1 >> c_2$ then each particle is more attracted to the individual best position, conversely, if $c_2 >> c_1$, then the particles are more attracted to the global best positions.

v_k^i, called inertia, makes the particle move in the same direction and with the same velocity. In this work inertia weight (*w*) starts with maximum amount and decrease linearly during evolution which provides a balance between global and local explorations, thus requiring less iteration on average to find a sufficiently optimal solution. The maximum inertia weight is set to 0.9 and the minimum is 0.4, which linearly decreases during a run, and it is calculated according to the following equation:

$$w_k = w_{max} - ((w_{max} - w_{min})/k) \quad 3\text{-}53$$

where w is inertia weight and k is the current number of iterations.

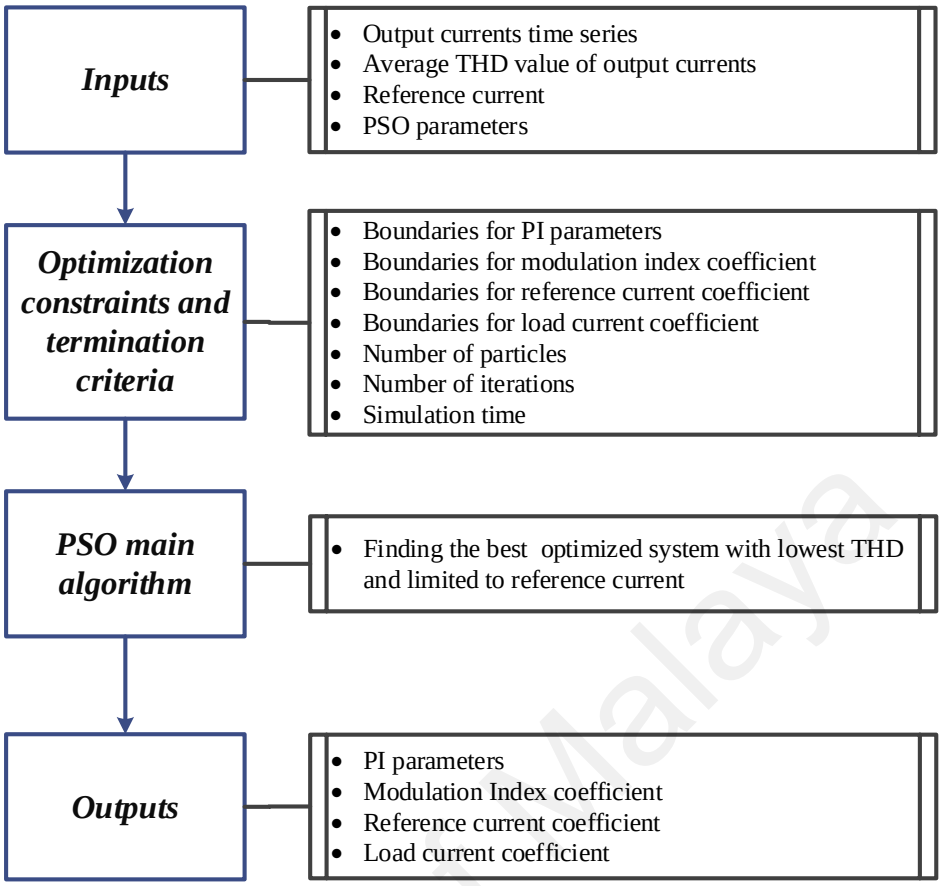

Figure 3-11: PSO algorithm

The PSO program is coded using MATLAB software and the performances of the proposed PSO controllers are evaluated via simulation for 40% unbalance input voltage with shifted phase. The switching frequency is strictly related to quality of output current waveform and the switching losses of the converter. The general model for PSO that has been applied in this study is illustrated by the flow diagram in Figure 3-11.

The problem described here has seven variables, which are the PI parameters for the closed loop current control and coefficients for modulation index, reference current and load current. In PSO, these variables are easily coded which each particle has a dimension space of seven. Figure 3-12 illustrates the designed controlling system and the parameters which are optimized by PSO.

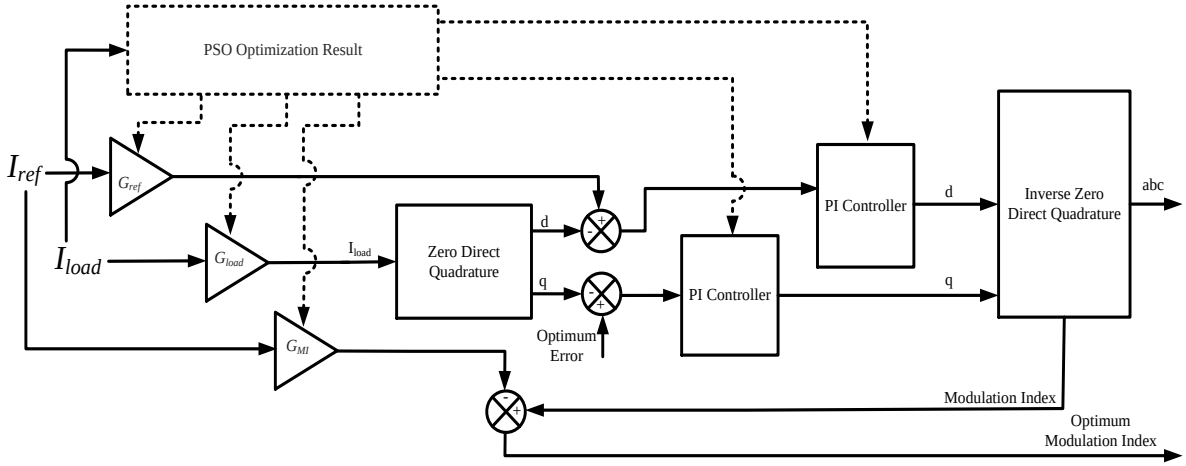

Figure 3-12: PSO optimized parameters

The variables to be controlled are the PI's parameters and controlling coefficients. The control objectives are the following: 1) decrease the THD level in output current and 2) to control the output current to constantly follow the reference current.

The goal is to decrease the undesirable harmonics in output currents by optimizing the PI parameters and other controlling parameters. In addition, the difference between the peaks in the sinusoidal waveform of phases is also added to the fitness function in order to make the output current closer to normal three phase sinusoidal while the output is limited to the reference current. The fitness function computes as:

$$\text{fitness} = \left(\sum_{k=a,b,c} \left\{ \text{Average} \left(\frac{\sqrt{\sum_{n=2}^{N} i_n^2}}{|i_1|} \right) \right\}_k + \sum_{k=a,b,c} \left\{ \langle |i_a^{peak} - i_{ref}| \rangle + \langle |i_b^{peak} - i_{ref}| \rangle + \langle |i_c^{peak} - i_{ref}| \rangle \right\} - \langle \text{THD}, i | \text{transient mode} \rangle \right) \quad \text{3-54}$$

where k represents the a-b-c phase sequence of a three-phase AC power source, in is the RMS current of n-th harmonic and i_1 is the fundamental frequency. In general, the

fitness function calculates the average THD after each simulation and also the maximum amount of sinusoidal waveform of current for each phase without considering the transition time as it can effect on the accuracy of results.

The best values, determined by the PSO algorithm, are used for the simulation and for real-time implementation. The process is off-line and this method does not require heavy online computation for adjusting PI parameters using artificial intelligent system, and can overcome up to 40% abnormality with high standard results in terms of normalization and output current THD.

3.3.2 Current Control of Voltage Source Inverter under Abnormal Conditions

The output voltage and current of the USZSMC is affected by abnormal input voltage disturbance, which contains twice the input frequency +/- output frequency on low order harmonics (Mohan & Undeland, 2007; Song et al., 2013). Additionally, the Z-source network property ameliorates the performance of the MC to be protected under abnormal input voltage perturbation (Peng, Shen, & Holland, 2007). The proportion between reducing the amplitude of U_{dc} and output voltage with input sag voltage has high impact on the rotation of the motor under normal conditions and may cause some damage (Bose, 1986; Erickson & Maksimovic, 2007). The output voltage and current can deliver a constant range of power, which is enormously dependent on U_{dc} and I_L. If $V_{a,refmax}$ is assumed to be the reference vector with maximum amplitude then it matches the radius of the biggest circle that can be encompassed by the hexagon shown in the control unit of the VSI in Figure 3-13. The relation between U_i and maximum rms fundamental output line-to-line voltage is as follows (Blaabjerg, Chen, & Kjaer, 2004):

$$\overrightarrow{U_o} = \sqrt{3}\left({V_{a,ref_{max}}}/{\sqrt{2}}\right) = 0.707 \times \left(\left|\overrightarrow{U_i}\right|\right) \quad 3\text{-}55$$

Due to the DC property of U_{dc}, its vector does not have an angle character and is introducing the magnitude of U_{dc}. On the other hand, the relation between $\left|\overrightarrow{U_{dc}}\right|$ and $\left|\overrightarrow{U_i}\right|$ has been illustrated in 3-40. In referring to 3-55, it can be computed as follows:

$$\frac{\overrightarrow{U_o}}{\left|\overrightarrow{U_{dc}}\right|} = \frac{0.707T}{T_1 - T_0} \quad 3\text{-}56$$

The property of $|Z| \times \vec{I}$ places $\overrightarrow{U_o}$ as the first assumption of steady-state mode with rated speed of motor for the equivalent circuit of IM. The U_{dc} on the same momentum needs to expand to $\sqrt{3} \times \overrightarrow{U_{in}}$ where the $\overrightarrow{U_{in}}$ is the consequent vector from three abnormal input voltages and placement of them into 3-56 brings the proportion shown below:

$$\frac{|Z| \times \vec{I}}{\overrightarrow{U_{in}}} = \frac{1.224T}{T_1 - T_0} \quad 3\text{-}57$$

The controlling system for the proposed method has been divided into the two major parts of CSR and VSI, as shown in Figure 3-13. The CSR controlling unit has the duty of controlling the rectifier under the abnormal input where the reference is the three-phase input voltage but in the range of unity. They determine the $\overrightarrow{V_d}$,$\overrightarrow{V_q}$, and $\overrightarrow{V_0}$. Consequently, these three vectors define the duty cycle of each space vector switching scheme based on the aforementioned stage of working principle of the ultra-sparse rectifier in section 2.2.5.1. The asymmetrical timing sequences can be achieved by the aforementioned stage above; however, it needs to be synchronized with the carrier signal of VSI in order to prepare the intransitive symmetrical system. The calculated duty cycles and carrier signal generate the switching state vectors in the symmetric sequence of the vector based on the selected sector where S_1, S_2, and S_3 can be generated.

The reference signal has been determined as the output phase current in the VSI control unit, which should be divided into $\overrightarrow{V_d}$,$\overrightarrow{V_q}$, and $\overrightarrow{V_0}$ elements and applied to the optimum PI controller by deducting the reference current value. Despite the fact that $\overrightarrow{V_0}$ does not need to be modified in any special operation, the reference current value can be set based on the controlled d and q parameters and optimized PI controller output. With the inversion of $\overrightarrow{V_d}$,$\overrightarrow{V_q}$ in the previous operation and the same $\overrightarrow{V_0}$ as the previous stage, the value of the modulation index can be calculated by multiplying to the coefficient of modulation index which has been generated from PSO result as shown in Figure 3-13.

The value of modulation index, to achieve the unity voltage transfer ratio under 40% unbalance input voltage with shifted phase, is 0.9587 which is presented in PSO section. Another two parameters have some effects on the gain of PI controllers, the coefficient for the reference current and the load current. As it can be seen from Figure 3-11, the coefficient for the reference current and the load current has some impacts on PI's outputs. Therefore, by optimizing those parameters, not only our system is stable and reliable but also it can be effectively used in industry.

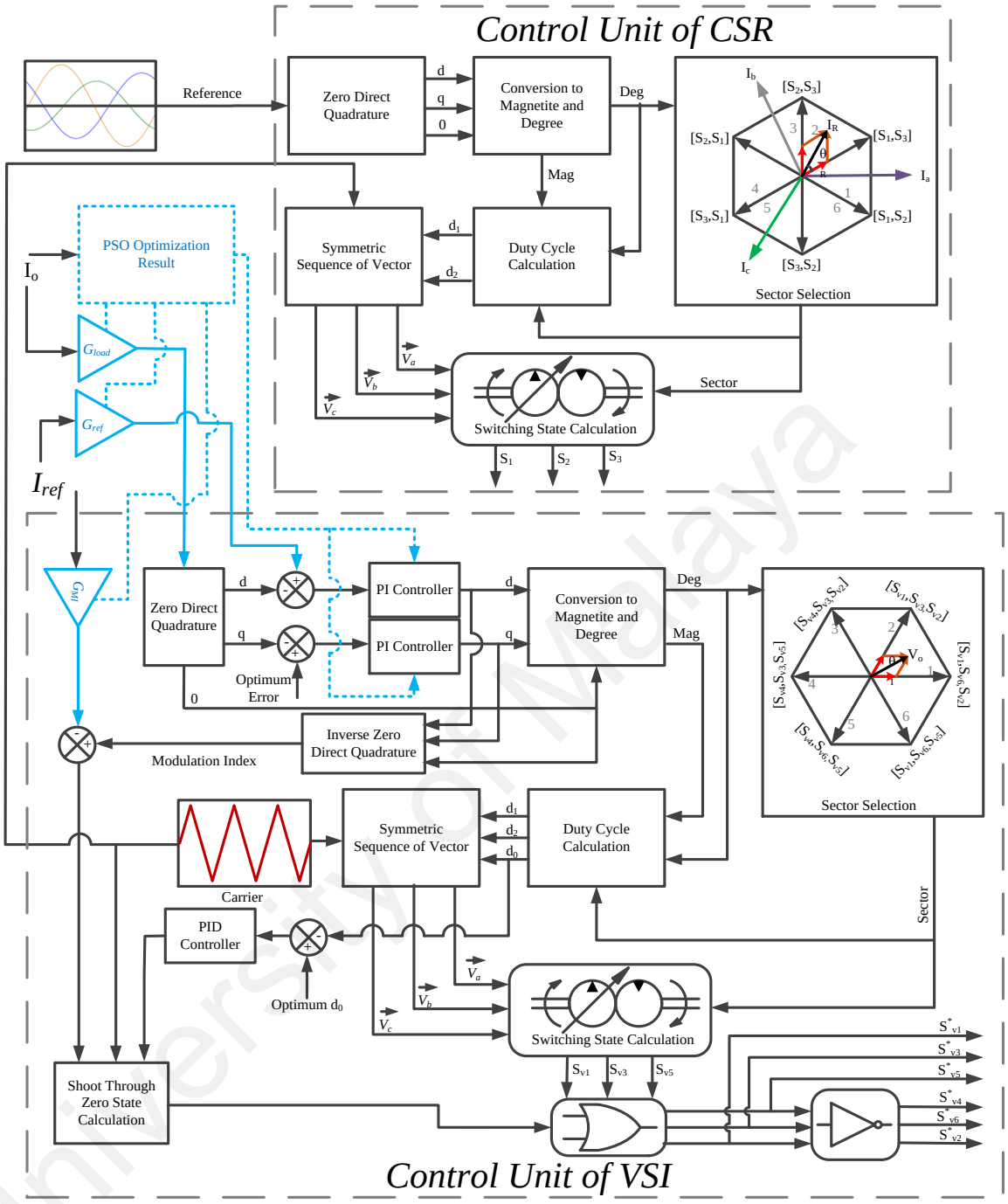

Figure 3-13: Current control diagram of USZSMC.

3.4 Switching State of the Ultra-Sparse Matrix Converter with 12 sectors

The indirect matrix converter with ultra-sparse topology has been presented in Figure 3-1 is of the most compact topology of matrix converter, which connects a three-phase grid to a three-phase load (normally a motor). There are 21 possible switching configurations, but only 18 of them are useful in DTC algorithm, which are given in Table

3-6 including the first 18 active voltage vectors having fixed directions. As shown in Table 3-6, the magnitudes of voltage vectors depend on the input voltages. The fourth and fifth columns of Table 3-6 show real (α) and imaginary (β) components of the matrix converter's output voltage vectors in stationary reference frame. The last three switching configurations correspond to zero-output voltage vectors.

Table 3-6: Ultra-sparse Matrix converter switching configuration.

Sw. Combination	on switches					voltage-vector		α-component value	β-component value
	Rectifier		Inverter			v_o	α_o		
+1	S_1	S_2	S_{v1}	S_{v3}	S_{v2}	$2/3v_{AB}$	0	$2/\sqrt{3}V_m\cos(\omega t+\pi/6)$	0
+4	S_1	S_2	S_{v1}	S_{v3}	S_{v2}	$2/3v_{AB}$	$2\pi/3$	$-1/\sqrt{3}V_m\cos(\omega t+\pi/6)$	$V_m\cos(\omega t+\pi/6)$
+7	S_1	S_2	S_{v1}	S_{v3}	S_{v2}	$2/3v_{AB}$	$4\pi/3$	$-1/\sqrt{3}V_m\cos(\omega t+\pi/6)$	$-V_m\cos(\omega t+\pi/6)$
-1	S_2	S_1	S_{v4}	S_{v6}	S_{v5}	$-2/3v_{AB}$	0	$-2/\sqrt{3}V_m\cos(\omega t+\pi/6)$	0
-4	S_2	S_1	S_{v4}	S_{v6}	S_{v5}	$-2/3v_{AB}$	$2\pi/3$	$1/\sqrt{3}V_m\cos(\omega t+\pi/6)$	$-V_m\cos(\omega t+\pi/6)$
-7	S_2	S_1	S_{v4}	S_{v6}	S_{v5}	$-2/3v_{AB}$	$4\pi/3$	$1/\sqrt{3}V_m\cos(\omega t+\pi/6)$	$V_m\cos(\omega t+\pi/6)$
+2	S_2	S_3	S_{v4}	S_{v3}	S_{v5}	$2/3v_{BC}$	0	$2/\sqrt{3}V_m\cos(\omega t-\pi/2)$	0
+5	S_2	S_3	S_{v4}	S_{v3}	S_{v5}	$2/3v_{BC}$	$2\pi/3$	$-1/\sqrt{3}V_m\cos(\omega t-\pi/2)$	$V_m\cos(\omega t-\pi/2)$
+8	S_2	S_3	S_{v4}	S_{v3}	S_{v5}	$2/3v_{BC}$	$4\pi/3$	$-1/\sqrt{3}V_m\cos(\omega t-\pi/2)$	$-V_m\cos(\omega t-\pi/2)$
-2	S_3	S_2	S_{v1}	S_{v6}	S_{v2}	$-2/3v_{BC}$	0	$-2/\sqrt{3}V_m\cos(\omega t-\pi/2)$	0
-5	S_3	S_2	S_{v1}	S_{v6}	S_{v2}	$-2/3v_{BC}$	$2\pi/3$	$1/\sqrt{3}V_m\cos(\omega t-\pi/2)$	$-V_m\cos(\omega t-\pi/2)$
-8	S_3	S_2	S_{v1}	S_{v6}	S_{v2}	$-2/3v_{BC}$	$4\pi/3$	$1/\sqrt{3}V_m\cos(\omega t-\pi/2)$	$V_m\cos(\omega t-\pi/2)$
+3	S_1	S_3	S_{v1}	S_{v6}	S_{v5}	$2/3v_{CA}$	0	$2/\sqrt{3}V_m\cos(\omega t+5\pi/6)$	0
+6	S_1	S_3	S_{v1}	S_{v6}	S_{v5}	$2/3v_{CA}$	$2\pi/3$	$-1/\sqrt{3}V_m\cos(\omega t+5\pi/6)$	$V_m\cos(\omega t+5\pi/6)$
+9	S_1	S_3	S_{v1}	S_{v6}	S_{v5}	$2/3v_{CA}$	$4\pi/3$	$-1/\sqrt{3}V_m\cos(\omega t+5\pi/6)$	$-V_m\cos(\omega t+5\pi/6)$
-3	S_3	S_1	S_{v4}	S_{v3}	S_{v2}	$-2/3v_{CA}$	0	$-2/\sqrt{3}V_m\cos(\omega t+5\pi/6)$	0
-6	S_3	S_1	S_{v4}	S_{v3}	S_{v2}	$-2/3v_{CA}$	$2\pi/3$	$1/\sqrt{3}V_m\cos(\omega t+5\pi/6)$	$-V_m\cos(\omega t+5\pi/6)$
-9	S_3	S_1	S_{v4}	S_{v3}	S_{v2}	$-2/3v_{CA}$	$4\pi/3$	$1/\sqrt{3}V_m\cos(\omega t+5\pi/6)$	$V_m\cos(\omega t+5\pi/6)$

Figure 3-14 shows the block diagram of the proposed USMC-based DTC scheme. The actual stator flux ψ_s and electromagnetic developed torque T_e are compared with their corresponding command values (ψ_s^* and T_e^*). The flux and torque errors are then sent to a separate hysteresis controller. The output of the torque hysteresis comparator is H_{Te}, and the output of the flux hysteresis comparator is H_φ. The switching states are the most important part of the control scheme and directly affect the driving performance. The switching states of the MC are generated based on H_{Te}, H_φ and the optimum switching configuration are selected to minimize the switching frequency based on the averaged variation of the flux in each voltage sector. Here, the amounts of input/output voltage/current are required for the estimators. However, input voltages (e_i) and output currents (i_o) are measured by proper sensors in each sampling cycle while other components are synthesized by combining the matrix converter's active switching.

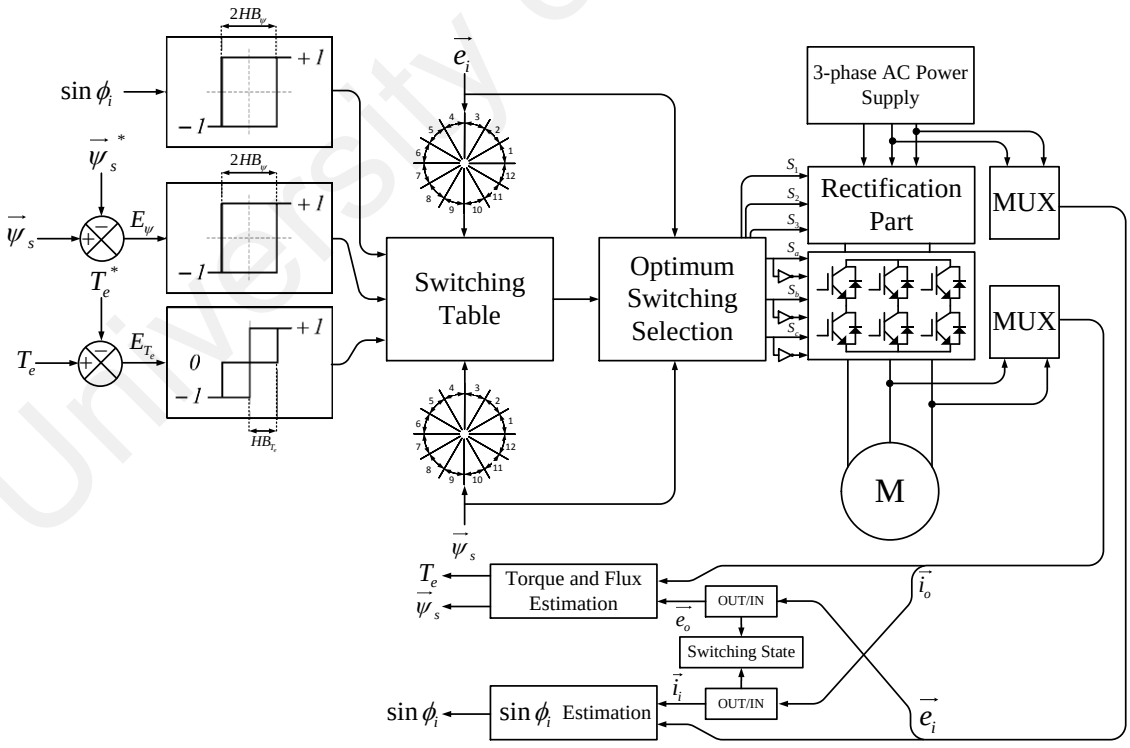

Figure 3-14: 30° sector-based switching scheme for an ultra-sparse matrix converter.

3.5 Z-source DTC for ultra-sparse matrix converter

Figure 3-15 shows the strategy of maximum boost control for the Z-source. This method is similar to the traditional carrier-based PWM control method. This control method keeps the six active states with no change and turns all zero states into shoot-through zero states. Therefore, for any given modulation index, the supreme T_0 and consequently BF_t can be obtained without distorting the output waveform. The system is in shoot-through mode when the carrier signal is either bigger than the supreme arc of the output current (I_a I_b I_c) or less than the minimum of output current. As can be seen in Figure 3-15, the duty-cycle is subsequently obtained from intercepting of modified modulation index with crossing the carrier waveform. In the mentioned figure, the non-shoot-through and shoot-through signal of lag A in both positions of odd and even switching have clarified that the shoot-through would happen when their sequence signals are alternatively in the OFF mode.

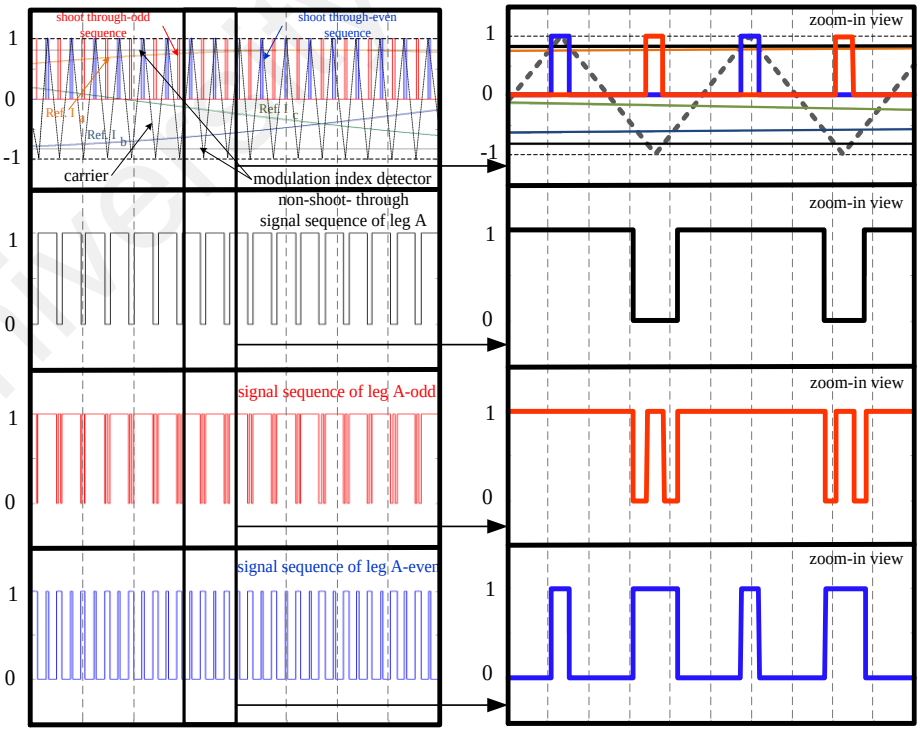

Figure 3-15: The pulse sequence generated with applied shoot-through state**.**

The concluding control algorithm of this study is shown in Figure 3-16, which includes the Z-source network and its control block diagrams at Figure 3-14.

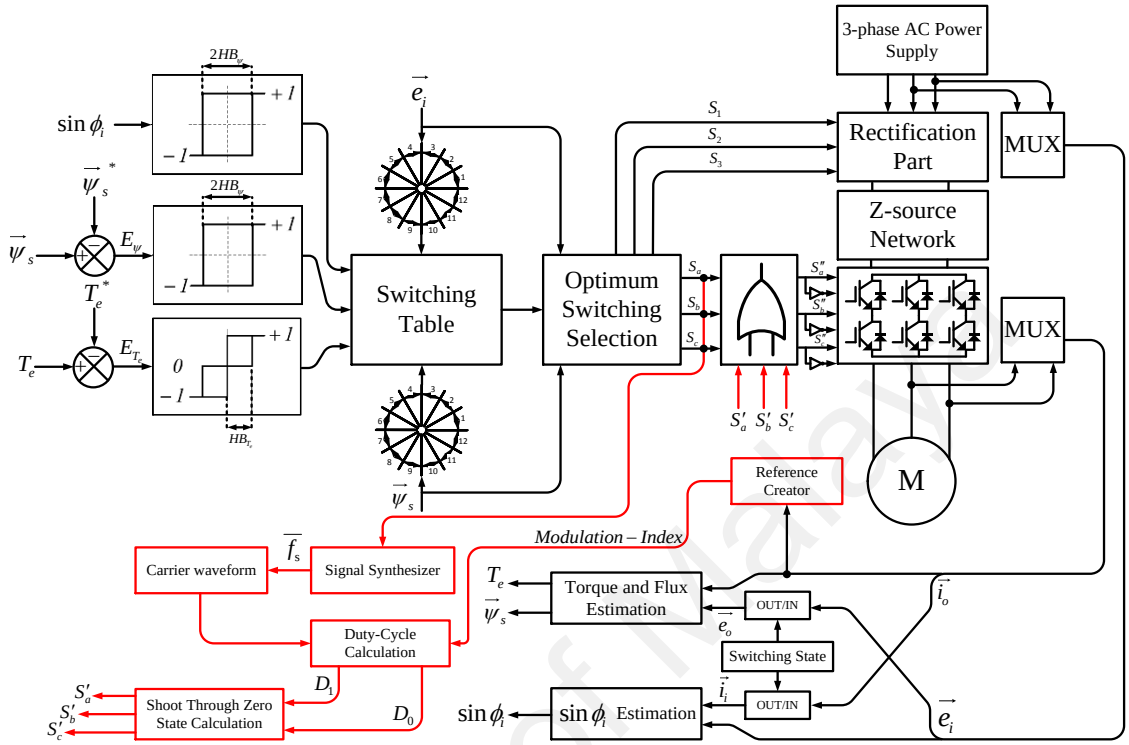

Figure 3-16: A 12-sector DTC-based control unit for ultra-sparse Z-source matrix converter.

The signal synthesizer unit detects the average switching frequency. Then, the carrier waveform is generating the saw-tooth wave in the average switching frequency. The results cross the modulation index to determine the shoot-through zero state. Therefore, the initial states of the optimum switching selection part, for the VSI, sum with the generated results of shoot-through calculation. Finally, the switching command of S_a'', S_b'' and S_c'' can be the applied as appropriate switching state to consider the torque ripple reduction up to 60%, boosting of the voltage ratio to the unity, and tolerating the abnormality in main up to 40%.

3.6 Chapter Summary

A new switching strategy based on 30° sectors of both flux and voltage is developed to increase the degrees of freedom in selecting voltage vectors. The change rates of both

torque and flux of IM as a function of voltage vectors are analytically derived. In order to simplify calculation and reduce the dependency of switching to motor parameter, an enhanced switching table of appropriate voltage and flux vector a proposed switching is established. The performance of the proposed switching strategy-based on matrix converter is compared to that of the conventional switching-based matrix converter for the DTC-based IM drive. The proposed switching strategy provides additional degrees of freedom to select voltage vectors and by selecting, the optimum switching state the torque ripple and switching frequency are reduced significantly. As a result, the proposed switching method has proven to be also effective in order to diminish the total harmonic distortion (THD) of input current.

The size of Z-source converter has been reduced by applying a novel calculation method with respect to timing and circuit perspective. The integrated metaheuristic algorithm (PSO) is employed to find the optimum values of PI and the coefficient of references, load current and modulation index in a single multimodal problem. Hence, the effect of all coefficients in minimizing THD is considered simultaneously. In this scheme, the modulation index can be spontaneously adapted to any variation in reference current or frequency without extra computational cost.

CHAPTER 4: RESULTS AND DISCUSSIONS

4.1 Simulation Results

In this chapter, the simulation results of 12 sector DTC for the direct matrix converter and under normal condition are discussed, which verified by their experimental. The simulation results of PSO-PI control of Z-source ultra-sparse matrix converter with abnormal input voltage are presented and their experimental results are depicted as well. The simulation and experimental results of 12-sector DTC to drive an induction motor under abnormal condition and unity voltage transfer ratio are discussed as well. It should be noted that the specification of system is exactly set as mentioned in Chapter 3. These specifications can be listed as induction motor (IM) (Table 3-2), topology of direct matrix converter (DMC) (Figure 2-2) and ultra-sparse Z-source matrix converter (USZSMC) (Figure 3-1).

4.1.1 12 sector DTC in DMC

The proposed DTC based IM drive is simulated extensively at different operating conditions using Matlab/Simulink software based on the detailed information on the diagram of Figure 3-3. The sample results are presented as follows.

Figure 4-1 compares the starting responses of the DTC based IM drive at rated speed under full load and 20% of load conditions for the proposed (30°-sector) and conventional (60°-sector) switching scheme, respectively. Figure 4-1(a) depicts how actual speed follows the reference speed. It is seen from Figure 4-1(b) and Figure 4-1 (c) that the torque ripple is less for the proposed switching scheme as compared to the conventional switching under full load terms and also in Figure 4-1(d) and 4.1(e) the comparison has been applied between suggested and conventional methods for 20% of loading conditions. Thus, the proposed switching scheme introduces lower vibration to the motor.

As the input current of the matrix converter is an important variable that should be monitored, the waveform of input current and its harmonic spectrum in the steady-state operation of the motor for both proposed and conventional methods at rated load are shown in Figure 4-1(f) and Figure 4-1(g), respectively and then for 20% of rated load illustrated in Figure 4-1(h) and Figure 4-1 (i). The components of the input filter are inductance ($L_r=4mH$) and capacitor ($C_r=40\mu F$). It can be seen that the distortion of input current for the conventional method is more severe than that of the proposed method. The THDs of the conventional and proposed methods under full load condition are 8.56% and 5.15%, respectively as well as one fifth of rated load are similarly 24.19% and 40.27%.

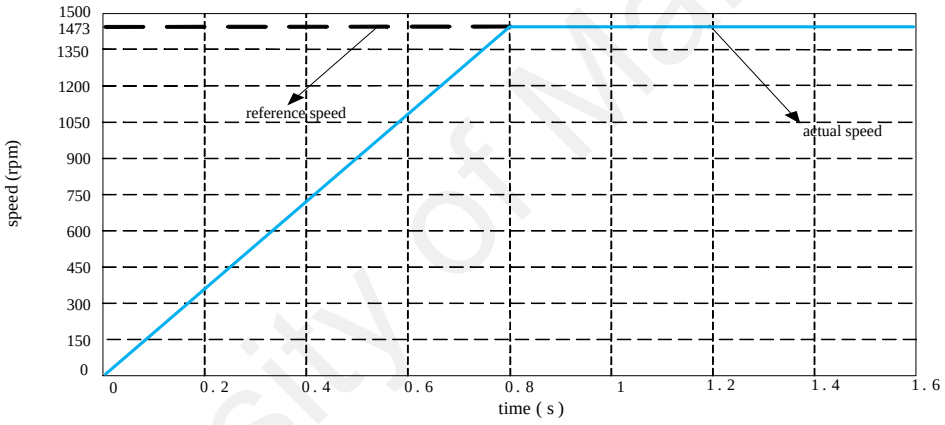

(a)

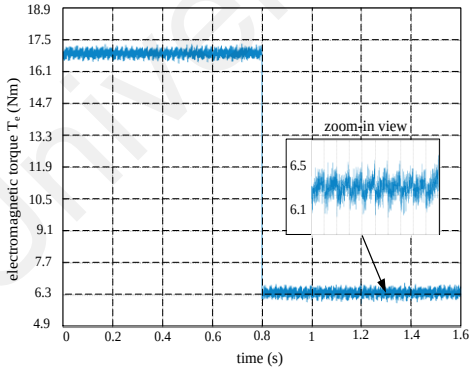

(b)

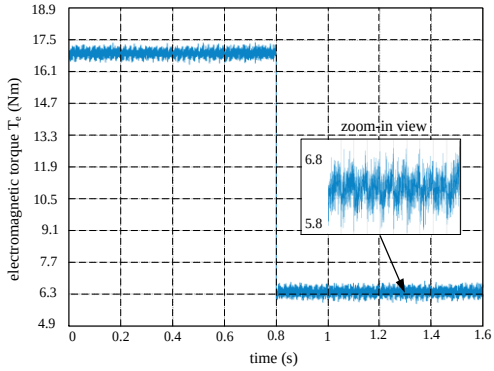

(c)

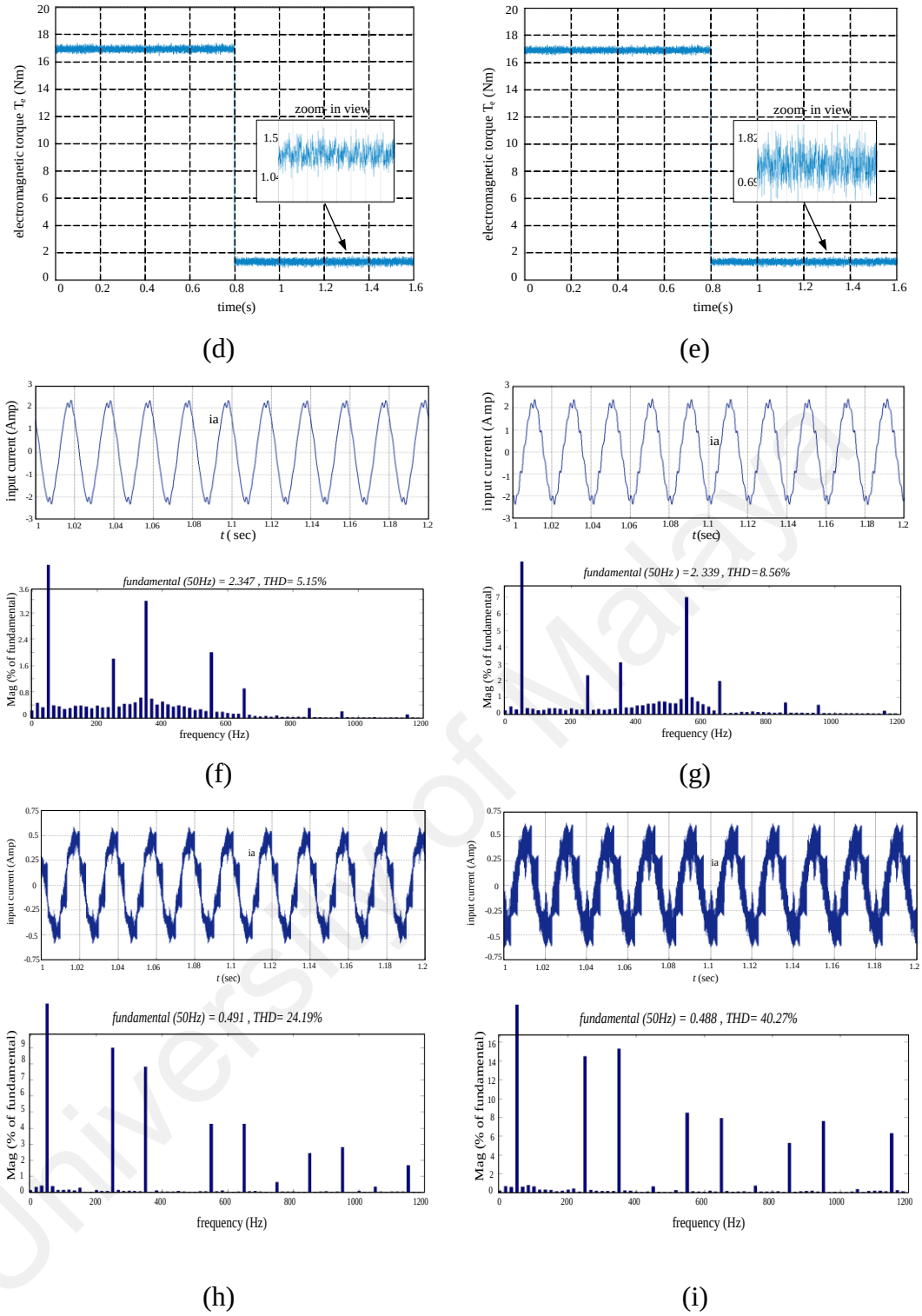

Figure 4-1: Responses comparison of the proposed switching method with conventional switching method at rated speed (*1473* rpm),rated load (*6.3* Nm), and 20% of rated load (a) speed; (b) torque response of the proposed method under rated load; (c) torque response of the conventional method under rated load; (d) torque response of the proposed method under 20% of rated load ;(e) torque response of the conventional method under 20% of rated load ; (f) input current and its THD spectrum of the proposed method under rated load; (g) input current and its THD spectrum of the conventional method under rated load; (h) input current and its THD spectrum of the proposed method under 20% of rated load; (i) input current and its THD spectrum of the conventional method under 20% of rated load

Figure 4-2shows the responses of the proposed DTC based IM drive at step changes of load conditions. It is seen from Figure 4-2(a) that the motor can follow the command speed in spite of changes from no-load to full-load conditions. Thus, the proposed drive is insensitive to load variations. It is also seen from Figure 4-2(b) that the torque ripple is very low at different load conditions. It is found that the flux remains constant while the load changes and the stator current changes with load, accordingly. Figure 4-2(c) and (d) show the produced flux and stator currents, respectively.

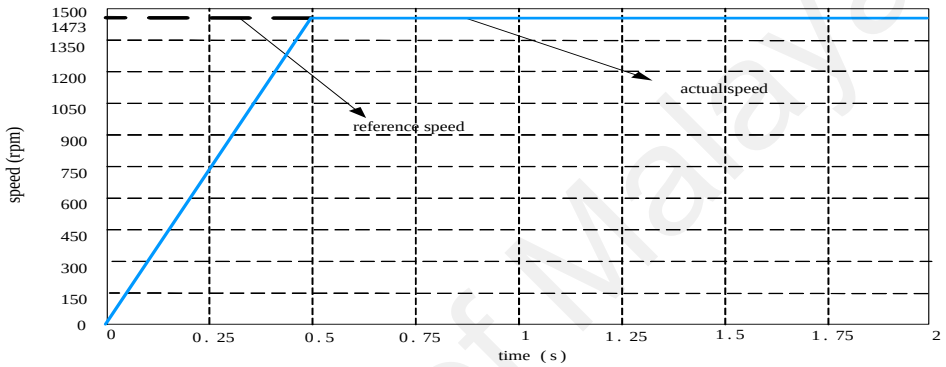

(a)

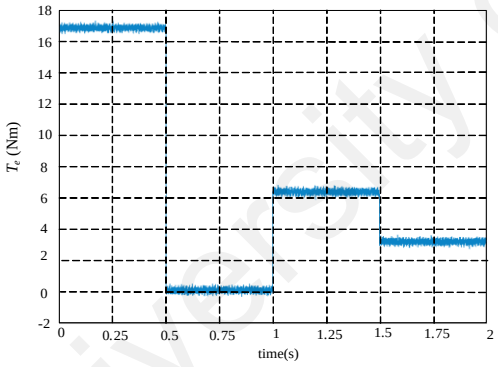

(b)

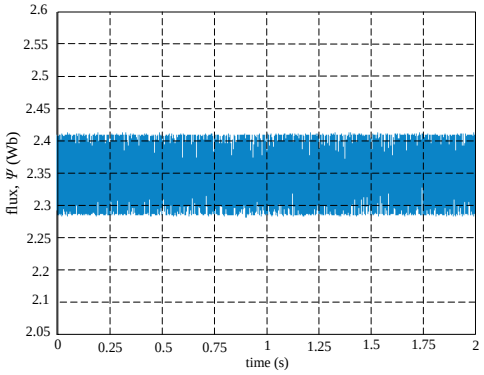

(c)

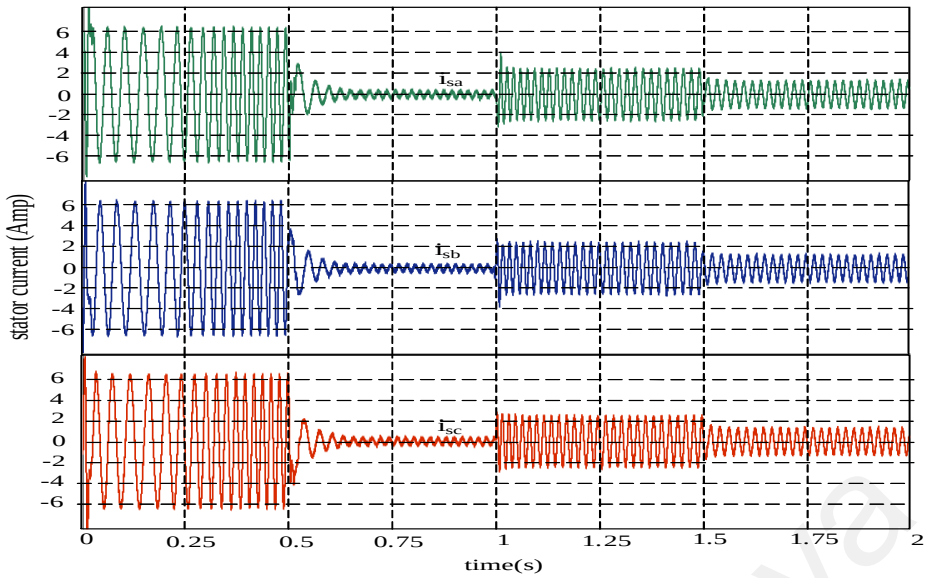

(d)

Figure 4-2: Responses of the proposed DTC based IM drive for step changes of load condition (a) speed; (b) electromagnetic torque; (c) stator flux; (d) stator-phase currents.

It is found that the motor can follow the command speed even if it changes to the reverse direction. Therefore, the performance of the proposed switching based matrix converter for IM drive is found robust at different operating conditions. Figure 4-3shows the speed, produced electromagnetic torque, flux and stator currents, respectively. It is clear that the motor can reverse rotation direction smoothly without any overshoot/undershoot or steady state error.

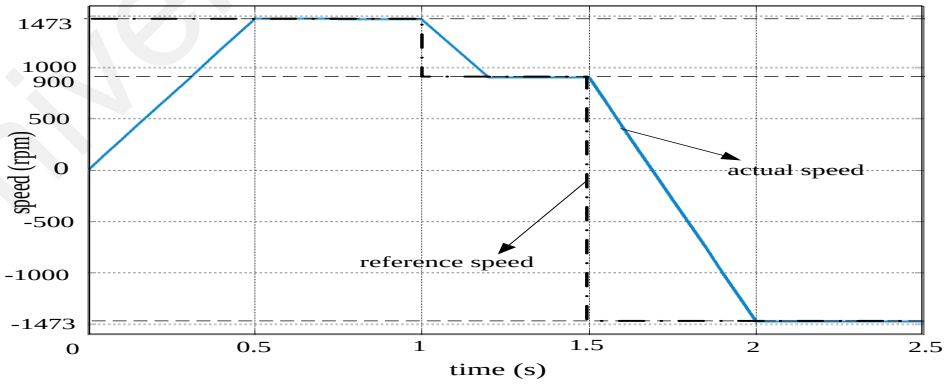

(a)

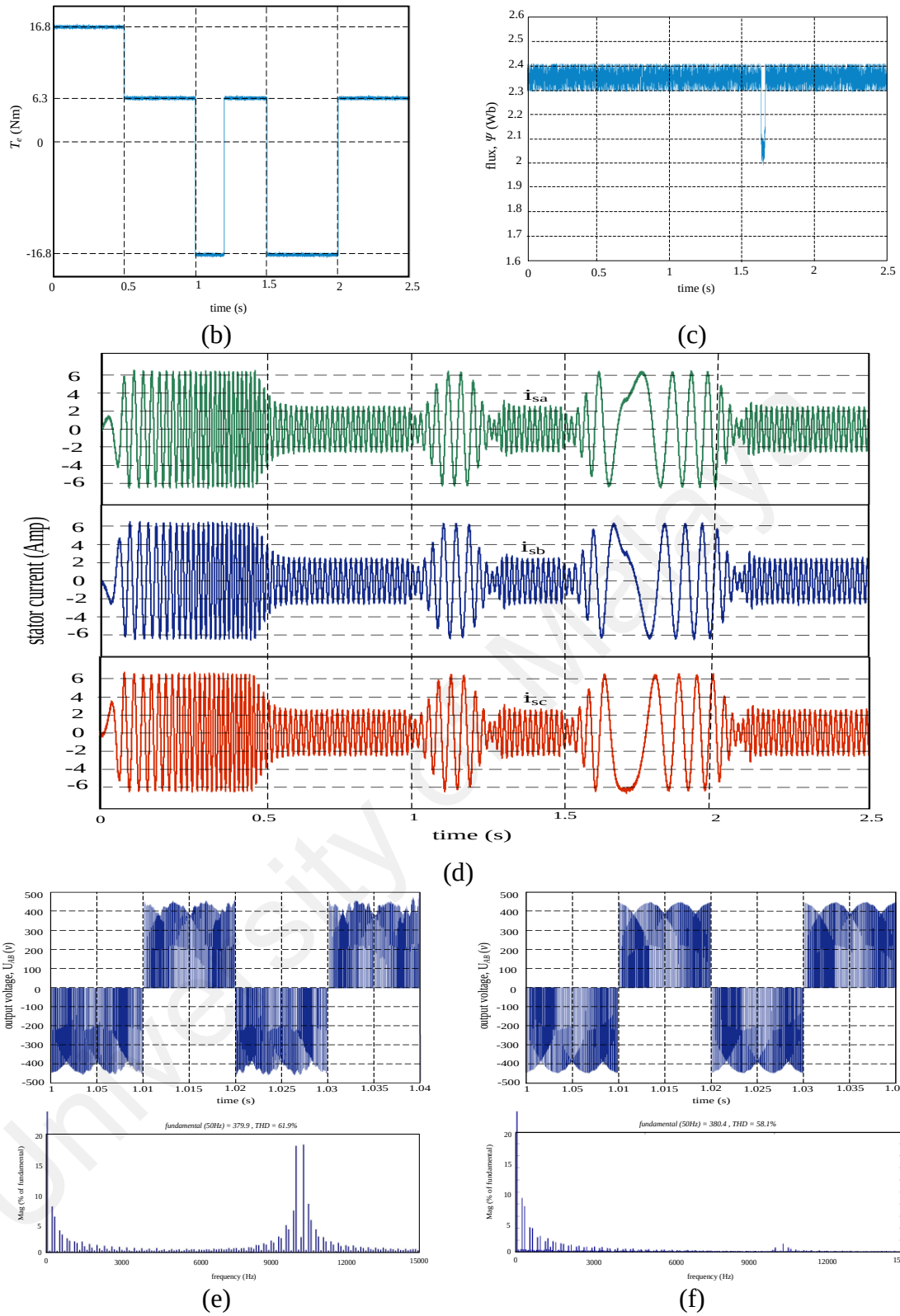

Figure 4-3: Responses of the proposed DTC based IM drive for step changes of command speed; (a) speed; (b) electromagnetic torque; (c) stator flux; (d) stator-phase currents; (e) output voltage and its THD spectrum of the proposed method; (f) output voltage and its THD spectrum of the conventional method

Figure 4-3(c) shows a short transient pick in the stator flux variation, which is caused by the changing the direction of rotor. In addition, the waveform of output voltage and its

harmonic spectrum in the steady-state operation of the motor for both proposed and conventional methods are shown in Figure 4-3(e) and (f), respectively. It can be seen that the harmonics of the proposed method are mainly in the vicinity of the switching frequency (10 kHz) as shown in Figure 4-3(e), while the harmonics of the conventional method are mainly distributed within the range of 0.5–6 kHz as shown in Figure 4-3(f). The result shows that the output voltage THDs of the conventional and proposed methods are 58.1% and 61.9%, respectively. To evaluate performance of the proposed method precisely, the comparison of the proposed method and the conventional switching method is summarized and tabulated in Table 4-1.

Table 4-1: Comparison of proposed switching method and conventional method**.**

parameters of comparison	proposed method	conventional method (Jose Rodriguez et al., 2012)
THD of MC input current	5.15%	8.56%
THD of MC output voltage	61.9%, harmonics are mainly in the vicinity of the switching frequency (10 kHz)	58.1%, harmonics are mainly distributed within the range of (0.5–6 kHz)
torque ripple reduction	60% reduction	fixed
maximum limit of reference voltage within circular locus of space vectors without over modulation	$V_{sm1} \times 1.11$	V_{sm1}
degrees of freedom to select appropriate voltage vectors for DTC	intensified	fixed

4.1.2 PSO-PI control of USZSMC

To verify the simulation results of the optimized current controlled USZSMC, several different operating conditions are tested using Matlab/Simulink® software based

on the details on the diagram of Figure 3-13 that the selected results are presented as follows.

4.1.2.1 Steady-State Response

The abnormal grid voltage, the equations of 100sin(ωt-10), 60sin(ωt-107) and 80sin(ωt+129) for phases A, B, and C, respectively and the corresponding 3-phase input current are demonstrated in Figure 4-4 (a). Figure 4-4(b) shows the virtual DC-link voltage, which is the CSR output (U_{dc}) and applied voltage as the DC output voltage of the Z-Source network (U_i).

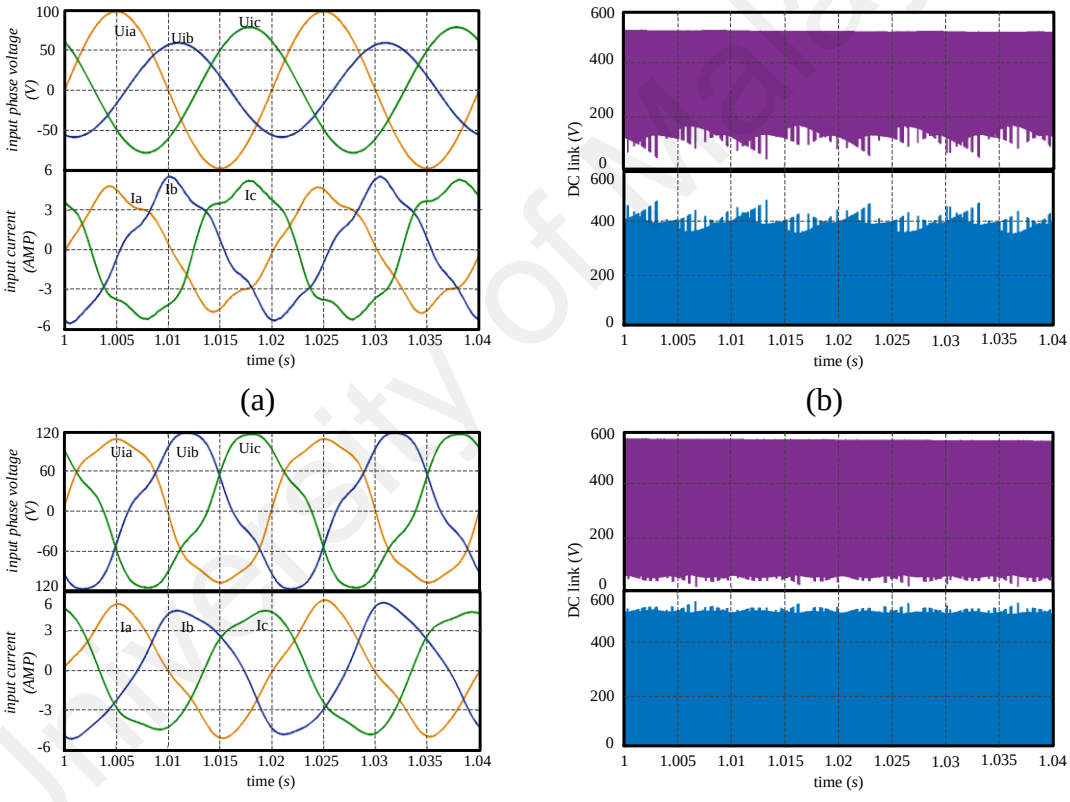

Figure 4-4: Input (a) abnormal-grid voltage and current; (b) abnormal supplied for DC-link voltage after and before Z-source; (c) distorted-grid voltage and current; (d) distorted supplied for DC-link voltage after and before Z-source.

It indicates the boost up level of the DC-link from the average 80 to 100√3 V. The distorted input voltage with 10% of 3rd harmonics and 5% of 5th harmonics, along with corresponding input current as shown in Figure 4-4(c). The DC-link voltage before (U_{dc}) and after (U_i) Z-source are shown in Figure 4-4(d) respectively.

The quality of output current for steady state condition of IM is shown in Figure 4-5(a) while the test is launched for distorted input grid supply and the THD of that is shown in Figure 4-5(b). The quality of output voltage is suitable for driving the mentioned IM, as can be seen in Figure 4-5(c). The THD analysis is illustrated in Figure 4-5(d) while the switching frequency is fixed on 10*kHz*.

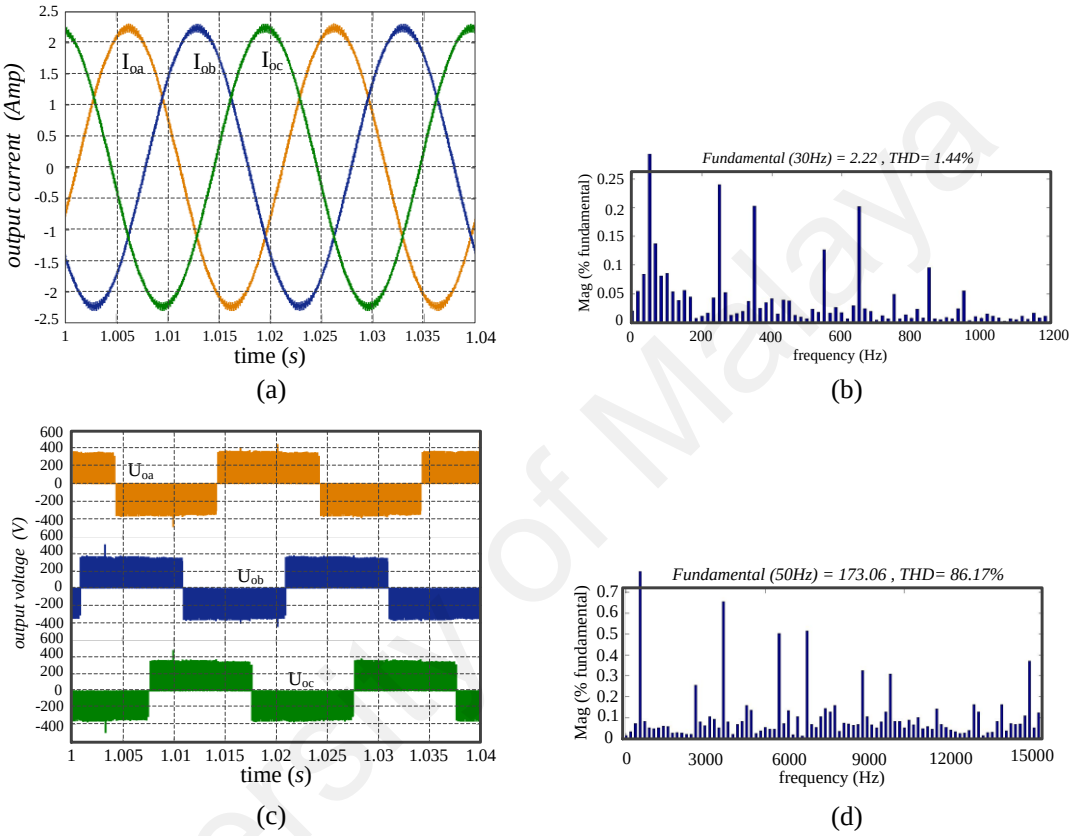

Figure 4-5: Output current and voltage under rated condition of IM with distorted supply (a) output current; (b) THD spectrum of output current; (c) output voltage; (d) THD spectrum of output voltage.

The comparison between conventional topology and ultra-sparse aims to show that the THD for the output current in the proposed method is less than the conventional (Figure 4-6(a) and Figure 4-6(b)). Here are three main differences between the proposed and conventional method: the topology, Z-source elements, and the control strategy. The six bidirectional switches for the CSR topology with a bypass diode in Z-source is known as conventional topology; and the PI-controllers have been tuned by using the Ziegler–Nichols method.

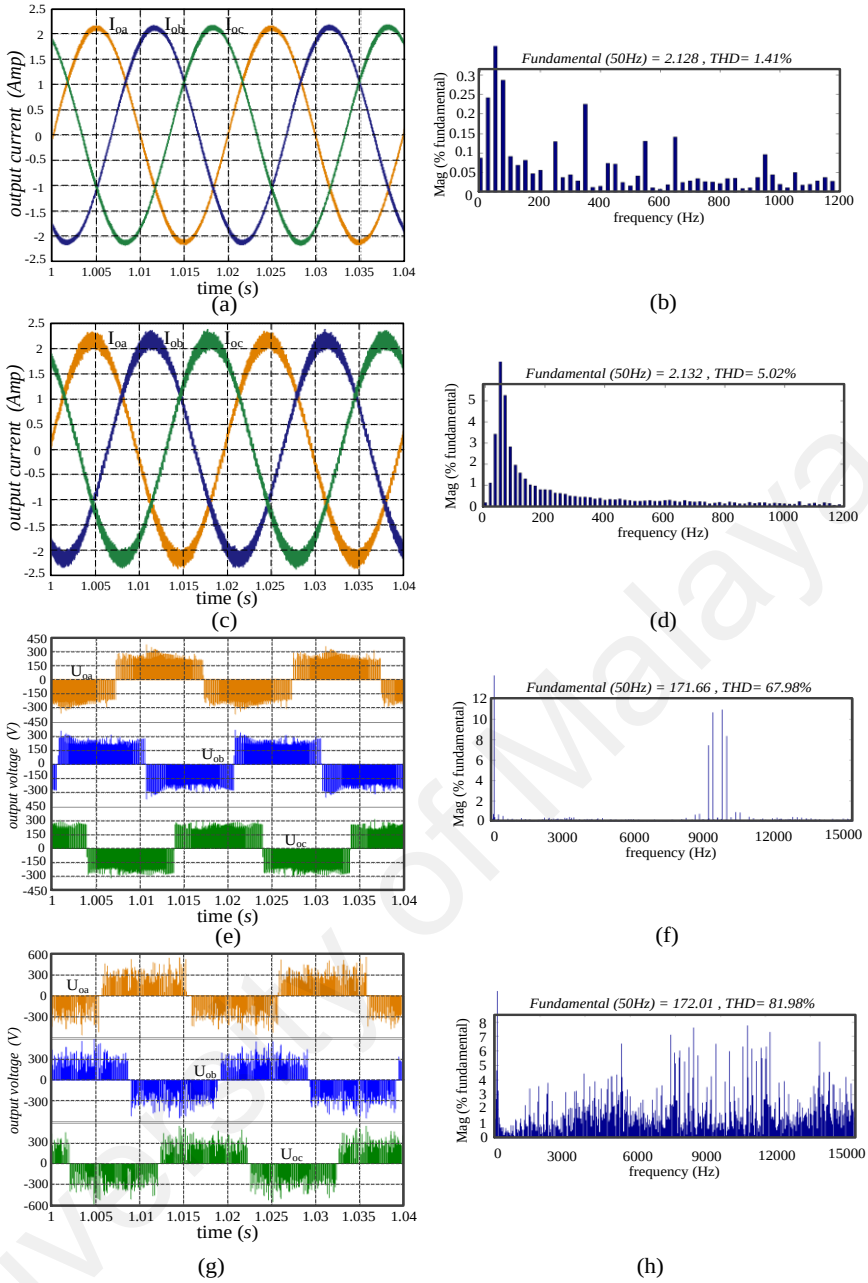

Figure 4-6 Output current and voltage under rated condition (a) output current with proposed method; (b) THD spectrum of output current with proposed method; (c) output current with conventional method; (d) THD spectrum of output current with conventional method; (e) output voltage with proposed method; (f) THD spectrum of output voltage with proposed method; (g) output voltage with conventional method; (h) THD spectrum of output voltage with conventional method.

Therefore, the proposed method has been improved from different perspectives. Meanwhile, for both methods the switching frequency is kept on 10kHz. According to Figure 4-6(c) and Figure 4-6 (d), the THD of the conventional prototype is 5.02%, which exposures more than triple of the target pattern (1.41%). Moreover, the accumulation of

the disturbance harmonics can be clarified by comparison between Figure 4-6(b) and Figure 4-6(d).

The unity voltage transfer ratio for the abnormal input voltage is defined based on the minimum compensation of the Z-source. In this case, our reference point is seeking the hypothesis for the normal input voltage with the magnitude of 100V. However, the system is created for the unbalanced condition, and can carry out abnormality up to 40%. Figure 4-6(e) and Figure 4-6(g) show the output line voltage for the conventional and the proposed method, respectively. In addition, the maximum range of the voltage surge in Figure 4-6(e) does not exceed 350V, whereas, in the ordinary prototype, it reached 600V, as clearly shown in Figure 4-6(g). As can be seen in Figure 4-6(f), the spectrum of harmonics is limited around the switching frequency and the THD is 67.98%, while the conventional topology in Figure 4-6(h) shows 81.98% for the THD. In addition, the spectrums of the various harmonics are not only serenaded the switching frequency but also from 3^{rd} to the very high order harmonics.

4.1.2.2 Dynamic Response

Figure 4-7(a) shows the variation of reference current, which can determine the applied current of IM. The dynamic response of the controlling system depends on the variation of D_0 and D_1 for which the duty cycle of the shoot-through and non-shoot-through states have been determined and displayed in Figure 4-7(b) and Figure 4-7(c), respectively. The alteration in the reference current should be followed by the actual output current, as shown in Figure 4-7(d). Initially, the IM is launched intensively with threefold the full load current (6.3A), which the starting current of the induction motor can reach maximally. After a quarter of a second, the reference value goes to 50% of the full load current (1.05A) with an instant decrement of the output current to 5.25A. To express the fact that the reliability of the controlling system validates both actions of decrement and

increment, the reference point has been set to 80% of the full load current, which has 30% increment in the output current compared to the previous period. The referral rate has been set for 20% of the full load current in the last fourth of 0.25 seconds with the target showing more than 50% decrement in the steady state response.

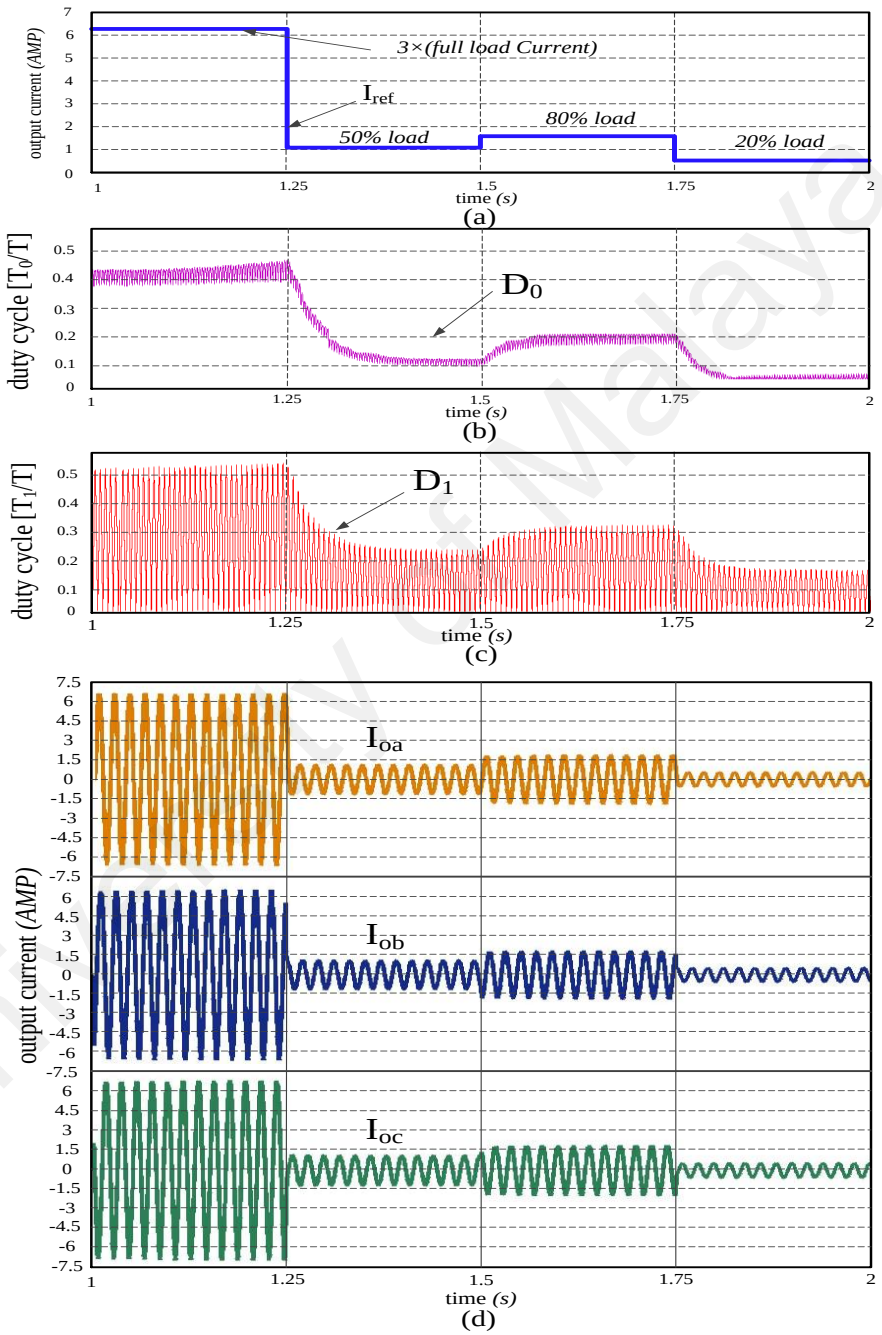

Figure 4-7: Dynamic response to changing magnitude in the output current (a) reference point of output current; (b) D_o variation; (c) variation of D_1; (d) stator-phase current.

In Figure 4-8, the THD analysis of each period of Figure 4-7(d) is shown separately. Figure 4-8(a) is threefold the full load current while the induction motor is starting. The

amplitude is 6.329A with 1.43% THD for the output current. Figure 4-8(b) shows 1.64% THD for 50% of the full load current with 1.091A as the magnitude of the output current. The output current with 1.688 amps and 1.46% THD for 80% of load has been illustrated in Figure 4-8(c). The last period of 20% of load is 2.24% and still lower than the THD of the full load current.

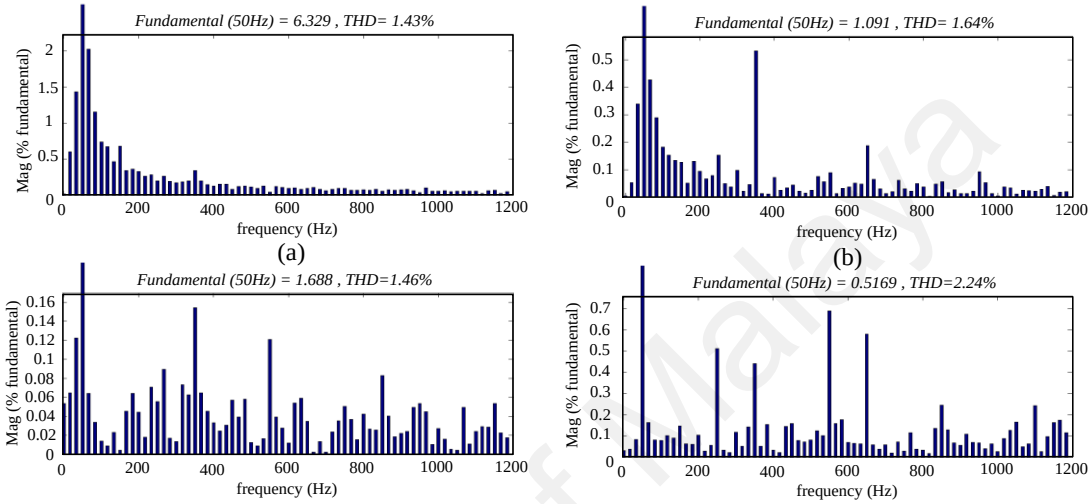

Figure 4-8: THD analysis of output current (a) triple the full-load current; (b) 50% of full-load current; (c) 80% of full-load current; (d) 20% of full-load current.

As an AC/AC converter, the most important part of the application for the USZSMC is to be a frequency converter, which drives the system under the required variation of frequency when the load is constant and the speed of IM has a direct interaction with the frequency. The frequency variations are surrounded around the fundamental frequency, which, in this case, is 50Hz. In Figure 4-9(a) the reference frequency for the input of IM and output of the converter has been set to 5Hz for half a second and then to 60Hz for a quarter of a second, and, similarly, 30Hz for the last period of 0.25 seconds. The conversion of frequency is shown in Figure 4-9(b) and Figure 4-9(c) for D_0 and D_1, respectively, which illustrates the constant value under different change. Figure 4-9(c) displays the constant magnitude of the output current in all three periods of frequency changing. It also shows the fast dynamic response of the proposed method for the sake of stability in the timing duty cycle.

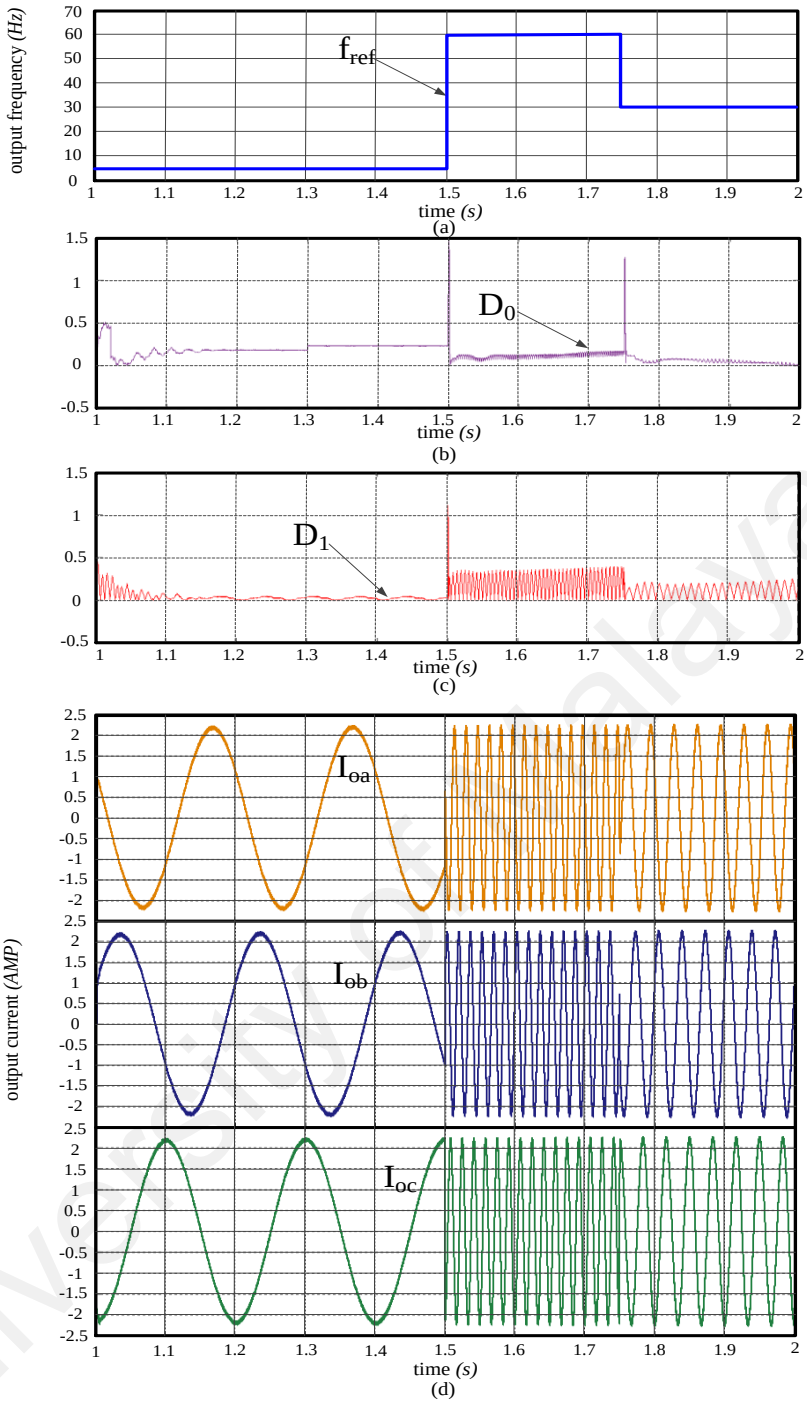

Figure 4-9: Dynamic response to changing frequency in the output current (a) reference point of output current; (b) D_o variation; (c) variation of D_1; (d) stator-phase current**.**

Figure 4-10(a) shows 1.3% THD for the output current at 2.1A magnitude with 5*Hz*. It appears that the lower harmonic orders have an insignificant effect on the total distortion and overall accumulation located up to the 50th order of harmonic. In Figure 4-10(b), the THD of the output current is 1.65% for the fundamental frequency of 60Hz,

and, in Figure 4-10(c), the reduction of THD for the output current compared with 60Hz is significant. When the reference frequency is changed to 30Hz, the THD becomes 0.81%.

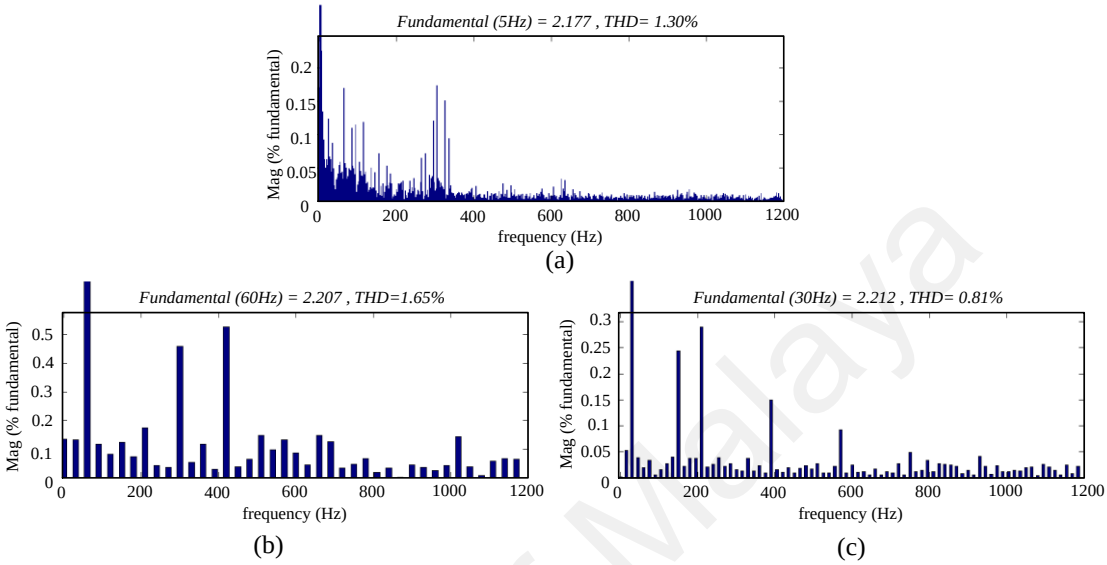

Figure 4-10: THD analysis of output current (a) 5Hz; (b) 60Hz; (c) 30Hz.

4.1.3 30° sector DTC for USZSMC

The combination of 12-sector DTC method by applying on USZSMC and 40% abnormal supplied is considered as the ultimate performance of this system. Therefore, the simulation results are presented based on various tests, which have been performed at the different operation conditions using Matlab/Simulink® software. The considered diagram is same as the previous section and performed based on Figure 3-16.

4.1.3.1 Steady-State Response

The input voltage equations of phase a, b, and c are considered as 380sin(ωt-20°), 228sin(ωt-110°), and 304sin(ωt+139°) respectively. The proper input voltage and current are displayed in Figure 4-11(a). The virtual DC-link voltage which is the CSR output (U_{dc}) and applied voltage as the DC output voltage of the Z-source network (U_i) are also shown in Figure 4-11(b). It points out the boost-up level of the DC-link from the average

304 to 380√3V. The unity voltage transfer ratio is determined with respect to the minimum compensation of Z-source. Therefore, the reference point seeks the hypothesis for the normal input voltage with 380V.

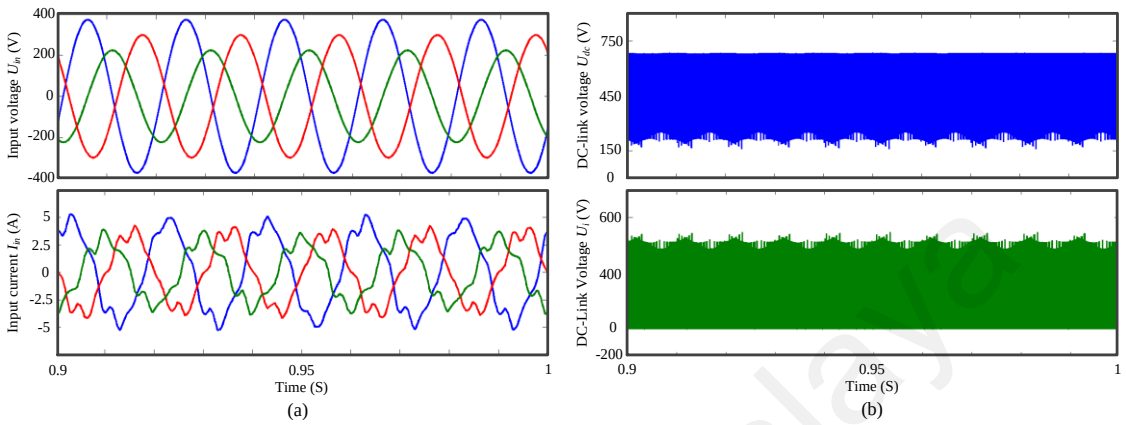

Figure 4-11: Input (a) voltage and current. (b) DC-link voltage before and after Z-source network.

The steady state response and under the abnormal condition, the proposed DTC system has been compared with the conventional Z-source matrix converter including standard DTC in which DTC technic has six sector of 60°. These two systems have been tested with the identical input voltage as shown in Figure 4-11(a). The input current is relatively distorted which is not a significant issue where the supplied grid is not connected to the power network. As discussed in the previous chapters, according to the expected specification of proposed system, this platform is portable and not connected to the national grid. Therefore, the distortion of input current is not the significant issue.

A comparison between the steady state of the conventional and proposed model in terms of stator current and voltage are depicted in Figure 4-12. Figure 4-12(a) and (c) are the stator current and voltage of suggested method and Figure 4-12(b) and (d) belong to the conventional model. It is clearly exposed that the quality of stator current and voltage of induction motor in proposed 12-sector DTC method are relatively better than the standard DTC driving control. Moreover, the maximum and minimum bound of stator

voltage in standard model is considerably higher than the recommended system, which increases the switching loss, stress, and consequently total loss of system.

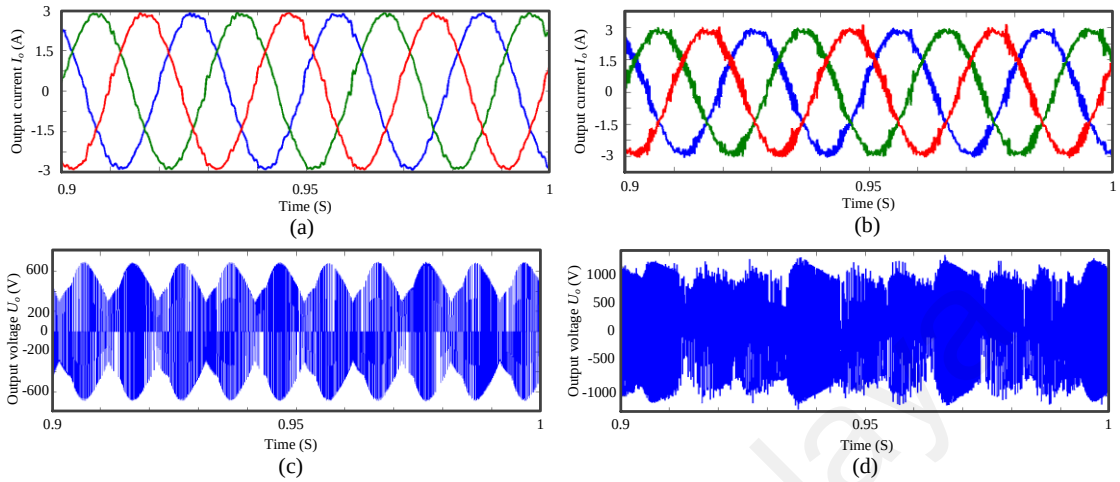

Figure 4-12: Steady state response of stator (a) current in proposed method. (b)current in conventional method. (c) voltage in proposed method. (d) current in conventional method.

4.1.3.2 Dynamic Response

To test the system in dynamic response, it is necessary to examine it by two benchmarks as follow,

1) The rotor speed is constant at nominal point and electromagnetic torque is varying.
2) The rotor speed and electromagnetic torque vary appropriately.

Hence, for the first stage of the dynamic test, the speed command is set on rated speed at 1473rpm. As can be seen in Figure 4-13(a), the rotor speed reaches to the nominal speed after 0.5 second. Accordingly, the torque command is set to the full load (6.3N.m) for the first 0.5 second in steady state speed, then, it changes to 50%, 80% and 20% of full load, respectively, for the rest of 0.5-second periods. By comparing the response of proposed and 60° sector strategy in Figure 4-13(b) and Figure 4-13(c), it can be realized the electromagnetic torque ripple is relatively diminished in proposed method.

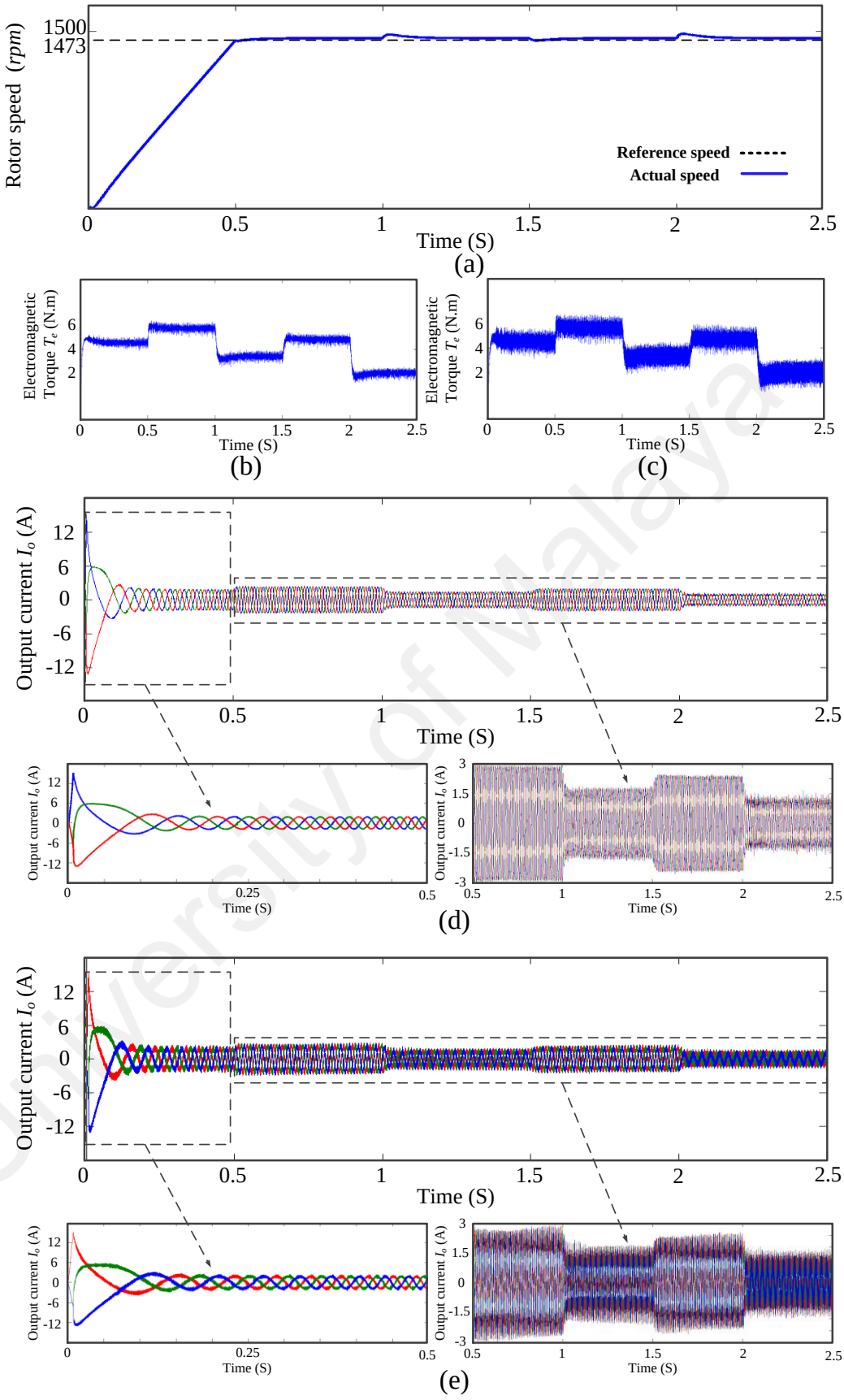

Figure 4-13: The dynamic response of system with constant speed. (a) Rotor speed. (b)Electromagnetic torque of proposed method. (c)Electromagnetic torque of conventional method. (d) stator current in proposed method. (e) stator current in conventional method

Figure 4-13 compares the starting responses of the DTC based IM drive at the variable load and rated speed conditions for the proposed (30°-sector) and conventional (60°-sector) switching scheme that the motor can follow the command speed in spite of changes of the load from no-load to full-load conditions. The reference point of electromagnetic torque varies from full load to 50% of its value, and then, 80% and 20%. The torque ripple is less for the proposed switching scheme as compared to the conventional switching. Thus, the proposed switching scheme introduces less vibration to the motor. It is depicted that the motor can follow the command speed even if it is change to the close value of zero (20%). Therefore, the performance of the proposed switching based ultra-sparse matrix converter for IM drive is found robust at different operating conditions.

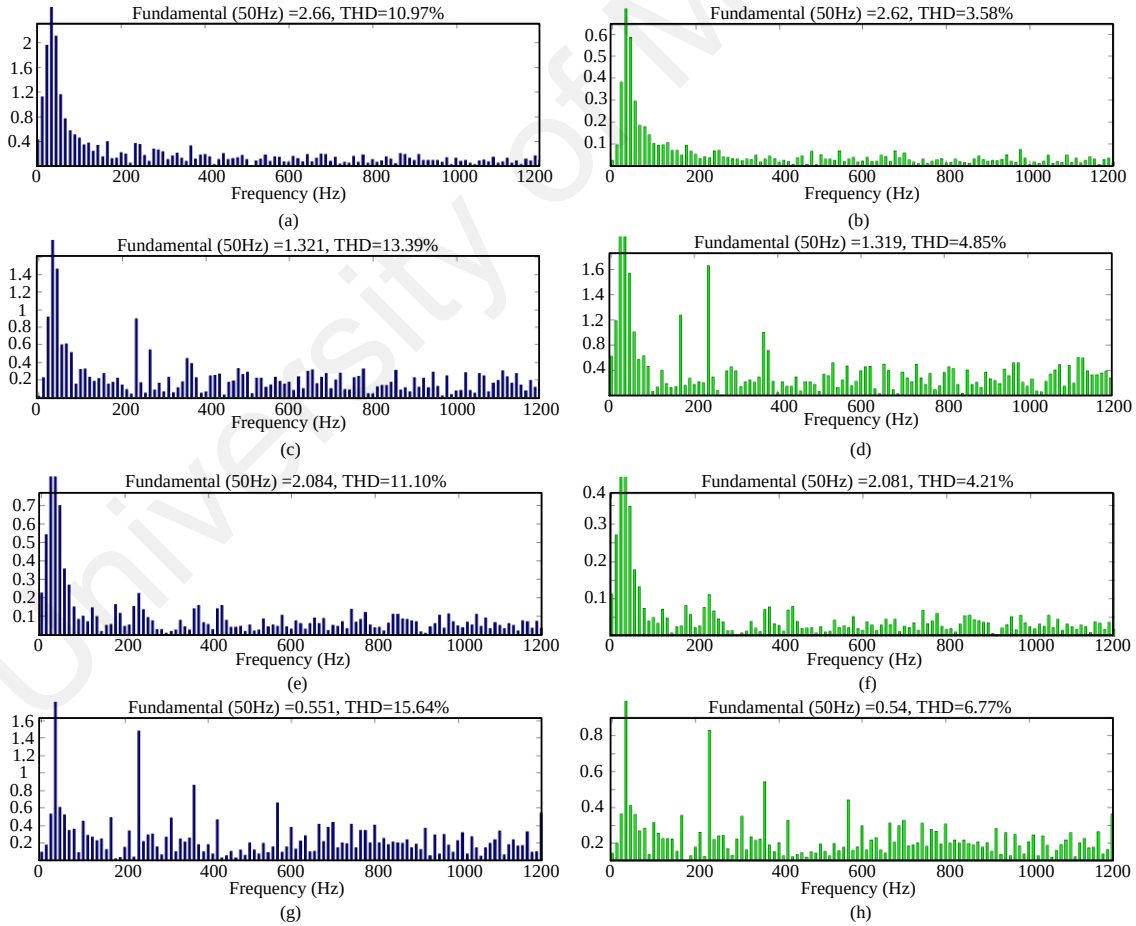

Figure 4-14: THD analysis: (a) conventional -full load current. (b) proposed -full load current. (c) conventional - 50%. (d) proposed -50%.(e) conventional - 80%. (f) proposed -80%. (g) conventional - 20%. (h) proposed -20%.

The THD analysis for the proposed and conventional switching scheme for the above mentioned variations are displayed in Figure 4-14, which proves the enhancement in quality of proposed method in compared with conventional 60° sector.

The speed, produced electromagnetic torque, and stator currents, at different operating conditions are shown in Figure 4-15. The motor can reverse rotation direction smoothly without any overshoot/undershoot or steady state error. It is clear that the motor can reverse rotation direction smoothly without any overshoot/undershoot or steady state error.

In Figure 4-15(a), the reference speed is seeking the rated speed at 1470rpm, then, after a second is decreased to the 50% of rated speed (735rpm). It follows the 50% of rated speed until 1.5*sec*, and then, it reached to the rated speed in the reverse direction at the 2.5*sec*. Therefore, the reference of electromagnetic torque is kept at the rated value with the considering the direction that motor is rotating. In the other word, the absolute value of T_e is constantly fixed on the full load (6.3N.m) while the direction of motor is considered. As can be seen in Figure 4-15(b) and Figure 4-15(c), the torque ripple of proposed method is significantly less than the conventional switching scheme. The ripple of torque has effect on the quality of output current of inversion part of converter, which supplies the induction motor. Consequently, in this benchmark, the stator current THD is significantly diminished in the proposed method in compare with the standard six sector-switching scheme.

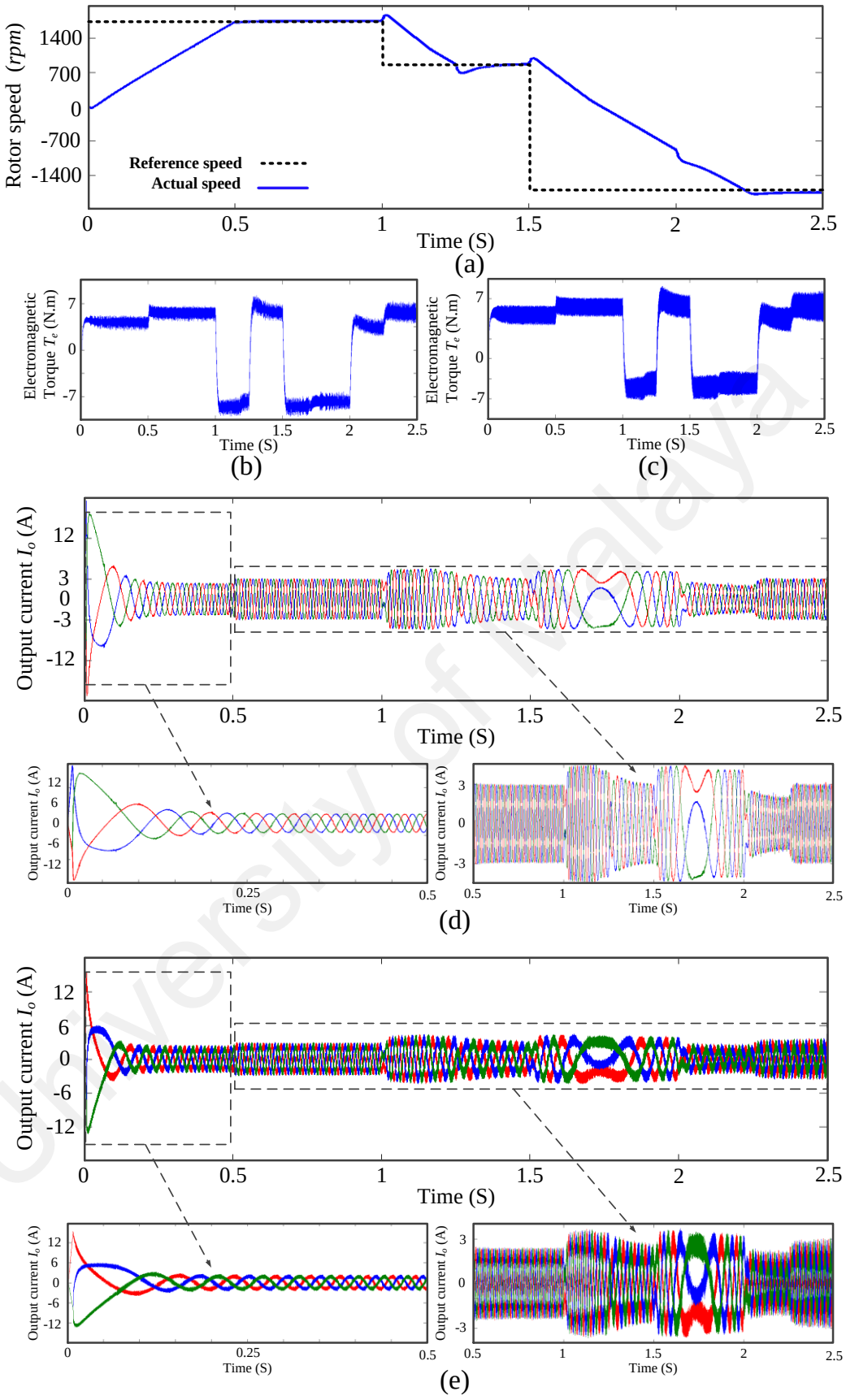

Figure 4-15: The dynamic response of system with variable speed. (a) Rotor speed. (b)Electromagnetic torque of proposed method. (c)Electromagnetic torque of conventional method. (d) stator current in proposed method. (e) stator current in conventional method.

4.2 Experimental Results

In this section, three experimental setups, which have been examined the proposed system for the following stages,

1) The proposed 12-sector DTC drives an induction motor by direct matrix converter under the normal input voltage.
2) The PSO-DQ current control drives an induction motor by ultra-sparse matrix converter under abnormal main and the unity voltage transfer ratio.
3) A 30° sector DTC drives an induction motor by the ultra-sparse matrix converter under abnormal input voltage and the unity voltage transfer ratio.

4.2.1 12 sector DTC in DMC

To verify the feasibility and effectiveness of the proposed DTC scheme based on 12-side polygonal space vector of voltage and flux, a matrix converter connected to 3-phase network through a variable AC power supply to feed a 1kw 3-phase IM was implemented. The experimental setup is shown in Figure 4-16 while the motor parameters are same as the parameters for simulation and listed in Table 3-2. In order to attenuate the harmonics of switching, an LC input filter was designed based on the values extracted from simulation. The matrix converter bidirectional switching is configured using IGBTs as in Figure 3-4. The proposed control algorithm is implemented by using TMS320F28335 digital signal processor (DSP).

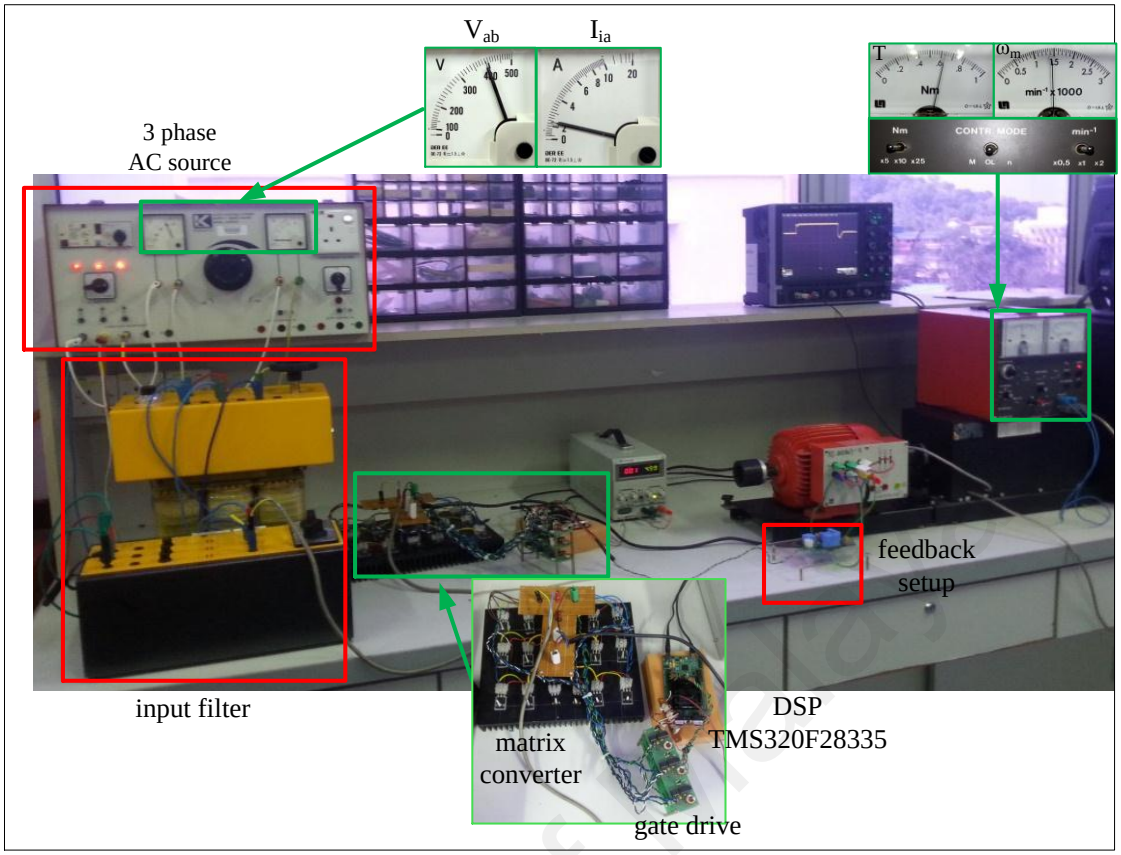

Figure 4-16: photograph of experimental setup of 12 Sector DTC Matrix Converter

4.2.1.1 Steady-State performance

Figure 4-17 presents the steady-state performance of the proposed switching scheme under rated conditions of the motor, speed (1473 rpm) and load (6.3Nm). The there-phase waveform of the output voltage and stator current are shown in Figure 4-17(a) and Figure 4-17(b), respectively. Figure 4-17(c) shows the three-phase input currents of the matrix converter at the steady - state performance under rated conditions of IM. The electromagnetic torque and speed waveforms of induction motor at rated condition are shown in Figure 4-17(d) and Figure 4-17(e), respectively. As it is evident in the zoom-in view, the ripples for both speed and electromagnetic torque are rather acceptable despite of high-frequency ripples.

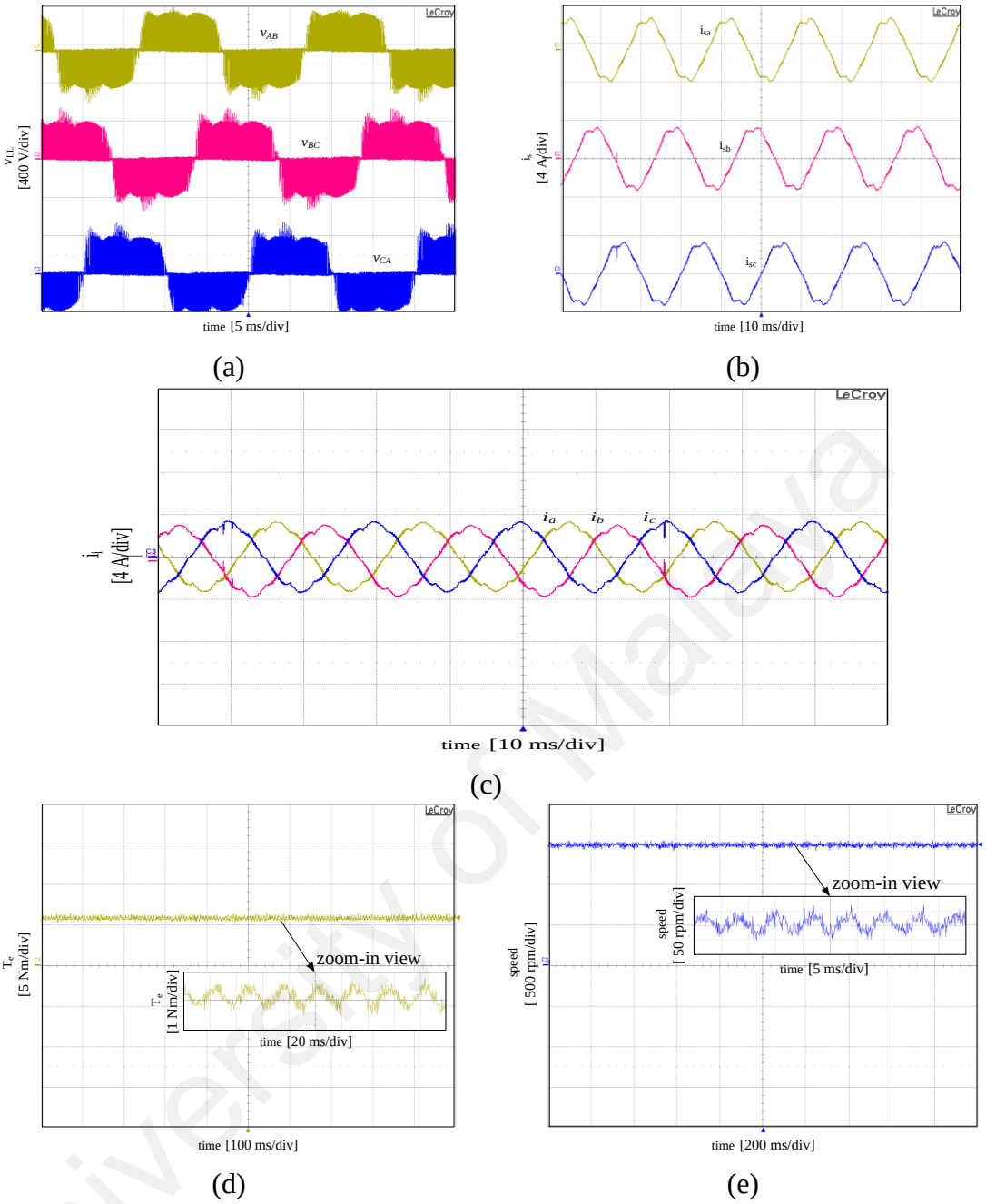

Figure 4-17: experimental waveforms of steady-state performance of proposed method at rated speed (1473 rpm) and rated load (6.3 Nm) (a) output voltage ; (b) stator current ; (c) input current ; (d) electromagnetic torque; (e) speed

4.2.1.2 Dynamic performance

Figure 4-18 shows the waveforms of the speed, electromagnetic torque and stator current of the IM drove by proposed method with speed reference value stepping up from 500 rpm to 1000 rp*m* at full-load condition (6.3 Nm). It is evident that with the step change of speed reference value the electromagnetic torque steps up within a short period. Once the actual speed reaches to the reference value, the electromagnetic torque reaches to the nominate value for a short period of time. It is concluded that the

proposed method has the advantage of fast torque, dynamic response with acceptable ripples.

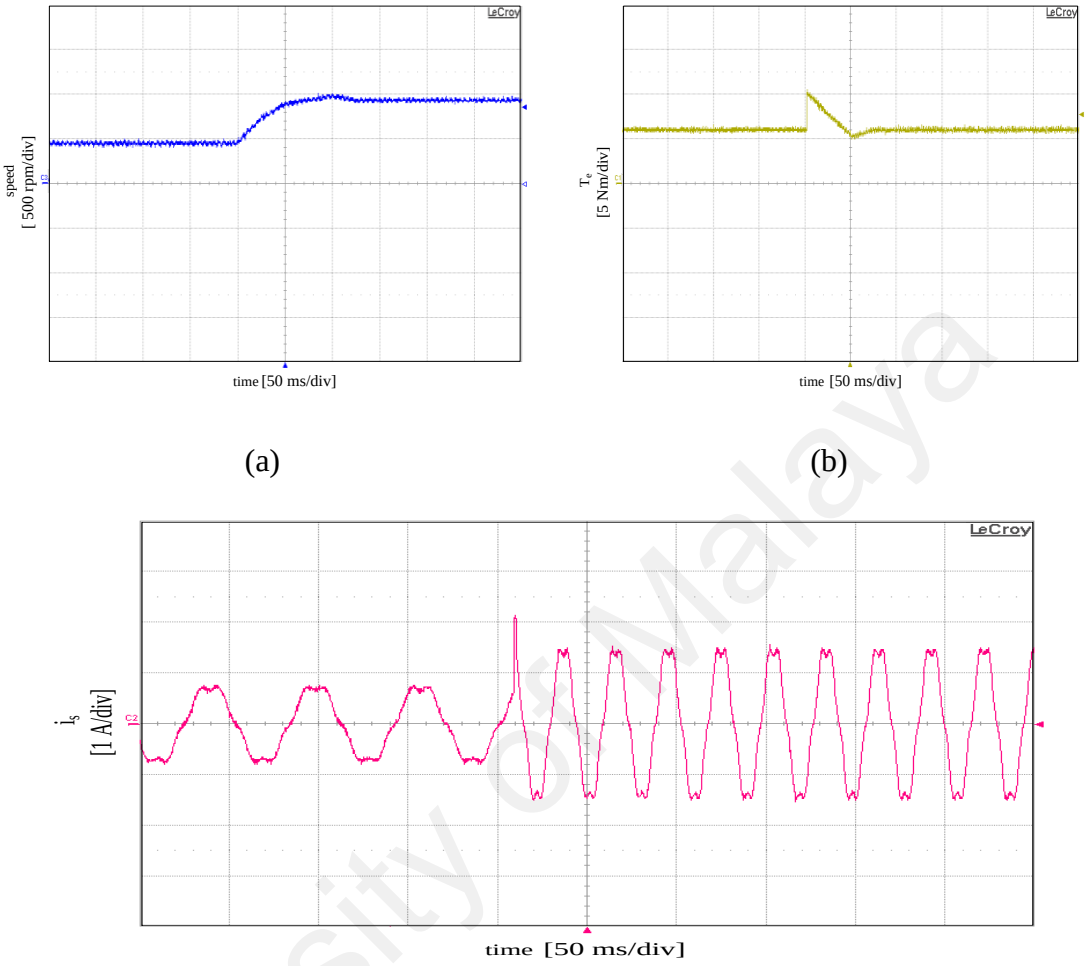

Figure 4-18: experimental waveforms of dynamic performance of the proposed method for speed reference step change, with speed reference increasing from *1/3* rated speed (1473/3 rpm) to 1/2 rated speed (1473/2 rpm) at rated load (6.3 Nm) (a) speed; (b) electromagnetic torque; (c) stator current

Figure 4-19 shows the waveforms of the speed, electromagnetic torque and stator current of the IM drove by proposed method with load torque step up from no-load to full-load, while the reference speed is kept constant at rated speed of 1475 rpm. The experimental results show that with the abrupt change of load, the electromagnetic torque increases rapidly and the speed reaches to the reference value only after a short period of time.

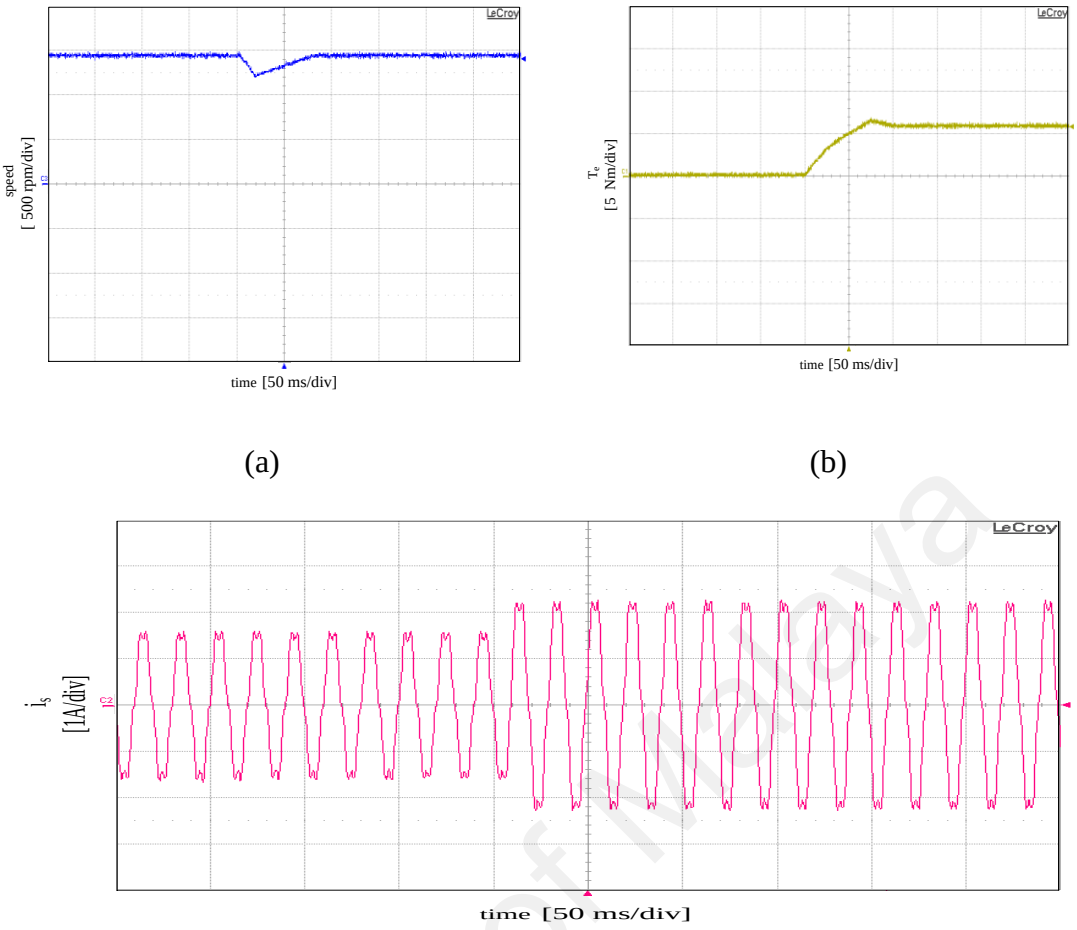

Figure 4-19: experimental waveforms of dynamic performance of the proposed method for load torque step change, with load torque increasing from no-load (0 Nm) to rated load (6.3 Nm) at rated speed (1473 rpm) (a) speed; (b) electromagnetic torque; (c) stator current

4.2.2 PSO-PI control of USZSMC

The PSO algorithm was mainly utilized to determine optimal controller parameters such that the controlled system could obtain a good response output and to improve the characteristics of output currents. For each iteration, the best among the 20 particles considered as potential solution and the best values for 50 iterations are sketched with respect to iterations in Figure 4-20.

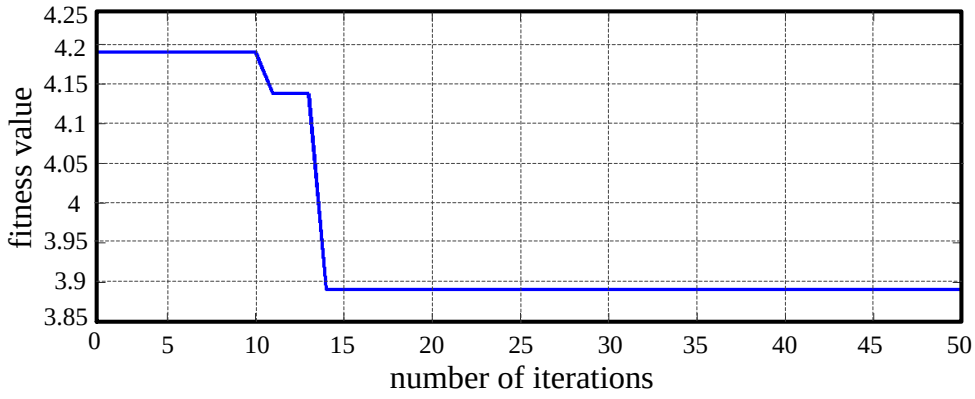

Figure 4-20: Fitness values for 50 iterations via simulation under 40% unbalance input voltage with shifted phase

The PSO method is applied in order to obtain the best output of the system by adjusting the PI parameters. The optimum values for the proportional and the integral parameters selected to control d are 16.5444 and 4.0826; and for parameter q they are 7.4637 and 5, respectively. The modulation index in the proposed method is controlled in real-time with a coefficient of reference current, 0.025, and load current of 0. 026. The modulation index confident is 0.01962 which results in 0.9587 modulation index. By applying any changes in current or frequency, the modulation index can be automatically adjusted and respond to changes without additional optimization or changing PI parameters in the system

The purpose of using PSO in this research is to find the most optimum value of K_{Pd} K_{Pq} K_{id} K_{Iq} G_{Iload} G_{Iref} G_{mi}, as the output vector, by evaluating the cost function which is THD of output current (3-54). The MATLAB simulator software is performed to evaluate the performance of the proposed PSO-PI controller. To find the accurate value of the output vector, the boundary for the elements of this vector is initially set to [0,10e6]. The first run of the algorithm is executed with the initial boundary. The results indicated that the boundary should be reduced to [0,300]. Therefore, PSO explores within smaller search space for the next runs. As a result, the more precise output vector is achievable. The PSO results is depicted in detail in Figure 4-21. The maximum function evaluation

is set to 6000. For better illustration of the result, the first twenty iterations are neglected and fifty critical points are selected from the total iterations.

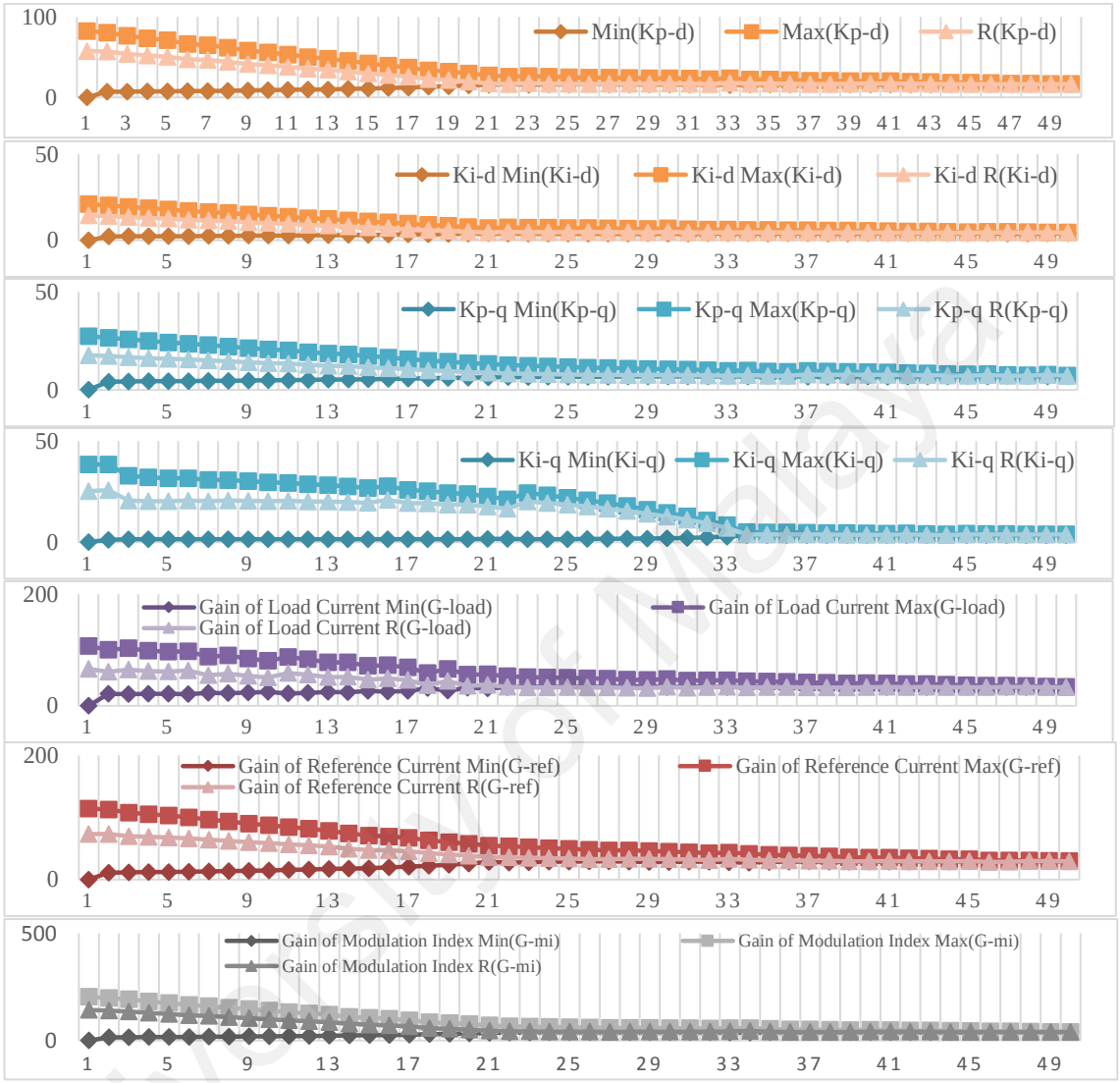

Figure 4-21: Fifty iterations out of 6000

The value for modulation index represents the main/average value for steady state condition, while can be varied in dynamic conditions. The modulation index in the proposed method is controlled in real-time with a coefficient of reference current, 0.025, and load current of 0.026. By applying any changes in current or frequency, the modulation index can be automatically adjusted and respond to changes without additional optimization or changing PI parameters in the system. This advantage is one of the features in the proposed method which help us to have a simple, yet cost effective

and efficient system with no heavy online computation that can satisfy some of requirements of industry.

To verify the feasibility and effectiveness of the proposed scheme, an USZSMC was implemented with its current control strategy connected to an abnormal 3-phase network through a variable abnormal AC power supply to feed a 1kw 3-phase IM. The suggested topology and control method were experimentally tested using the experimental prototype shown in Figure 4-22 with the same motor parameters as those for the simulation listed in Table 3-2. The component values chosen for the simulation were similar to those assembled for the hardware setup; the Z-source values are summarized as C_Z = 170μF and L_Z = 0.25mH for the Z-source network. It is noted that the Z-source inductance chosen was quite high because of the low average currents flowing in the setup, which, somehow, made the sixth order ripples appear prominently if the inductance was not high enough. For better performance at a higher current level, the design rules in 2.2.5.1 should be followed, which will likely result in smaller C_Z and L_Z values.

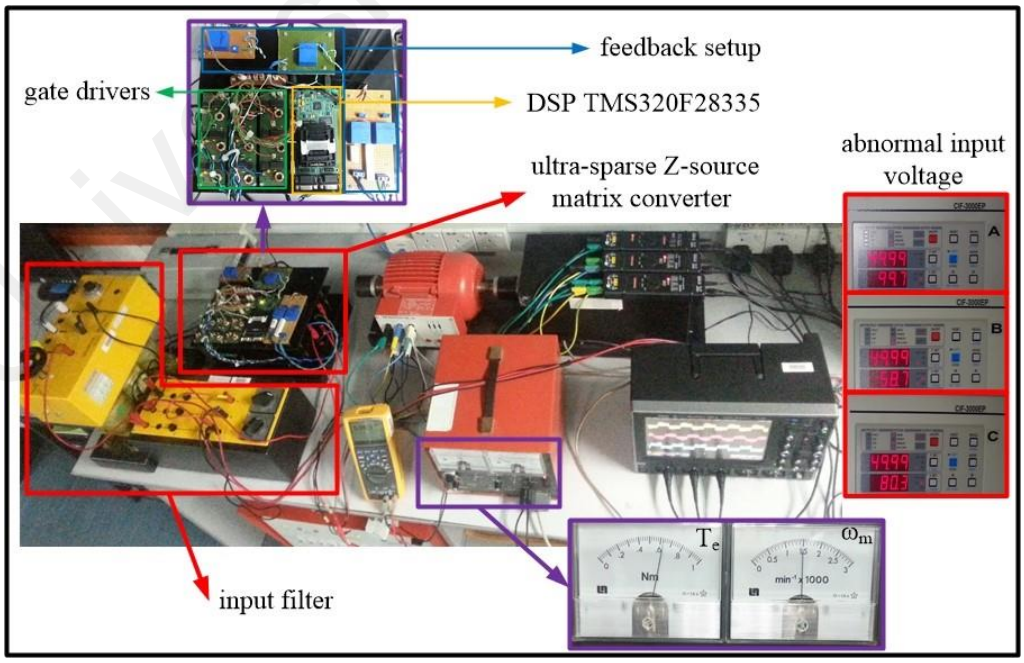

Figure 4-22: Photograph of the experimental setup of PSO-DQ for USZSMC

In order to diminish the harmonics of switching, an input filter was designed based on the values extracted from simulation for L_f =1mH and C_f =10μF. The USZSMC switching was configured using IKW40N120H3 and IGW30N60T IGBT and IDP30E120 diode, as shown in Figure 4-22. The bottom level of the framework includes the ultra-sparse rectifier and two-stage inverter; the mid-level consists of the Z-source network elements with no sensor for detecting the voltage of capacitor or current of the inductor; and the overhead level comprises gate drives, controlling unit process, and feedback setup. The closed loop control was carried out using a TMS320F28335 digital signal processor (DSP).

4.2.2.1 Steady-State performance

The three phase abnormal input voltage with the magnitude of U_a=100V, U_b= 60V and U_c=80V has been shown in Figure 4-23(a) where U_c and U_b are respectively engaged with a 40% and 20% abnormality rate from U_a. For phase A, the input voltage (U_{ia}) and input currents (I_{sa}) after and before filter is presented in Figure 4-23(b) in order to prove the input unity power factor of the system. The virtual DC-links voltage for after(U_i) and before (U_{dc}) Z-source network at the steady-state performance under rated condition of IM by applying the shoot-through duty cycle are shown in Figure 4-23(c).

The output voltage waveforms under abnormal input voltage are shown in Figure 4-24(a). The output current waveform is shown in Figure 4-24(b) and presents the steady-state performance of the proposed scheme under rated conditions of the motor with a speed of 1473 rpm, 6.3 Nm for load, unbalanced magnitude, and shifted input phase voltage $|\Delta\emptyset_{U_a}|$= 10º , $|\Delta\emptyset_{U_b}|$= 13º, and $|\Delta\emptyset_{U_c}|$= 9º.

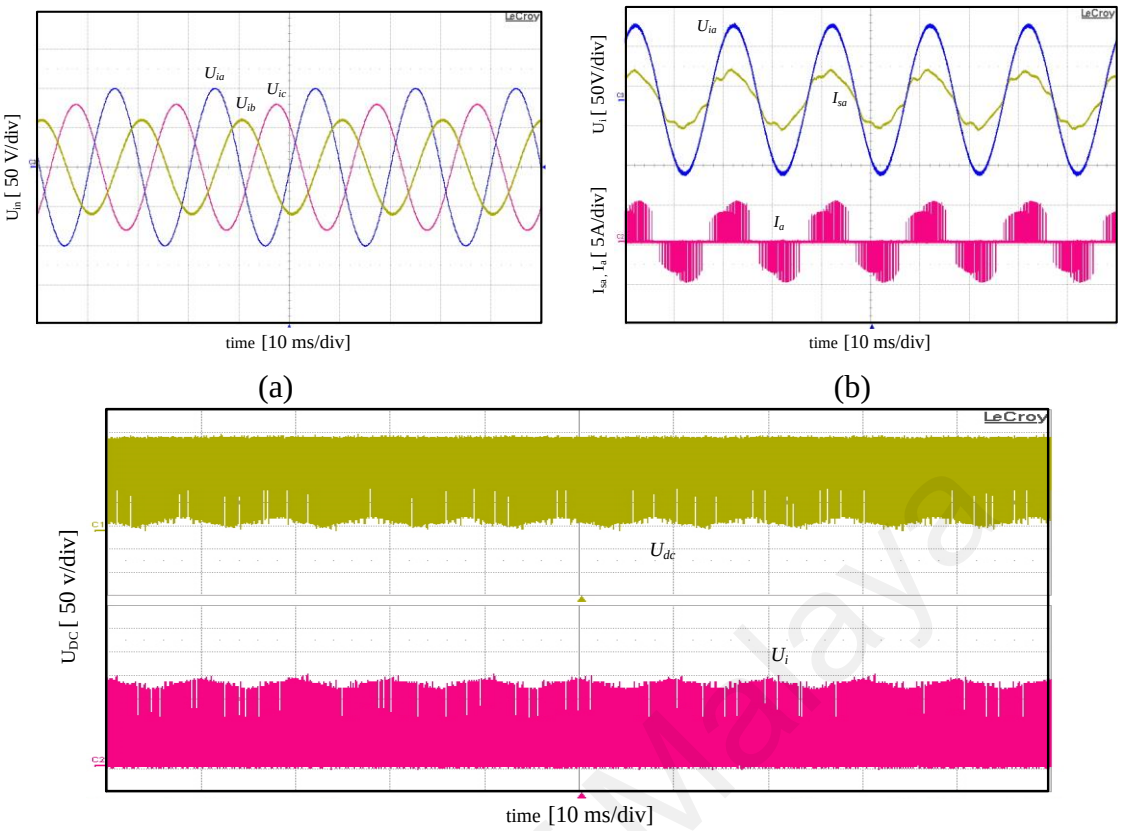

Figure 4-23: Steady-State performance (a) three phase abnormal input voltage, (b) input current after and before filter, (c) voltage of U_{DC} (after Z-source) and U_i (before Z-source) at DC-link.

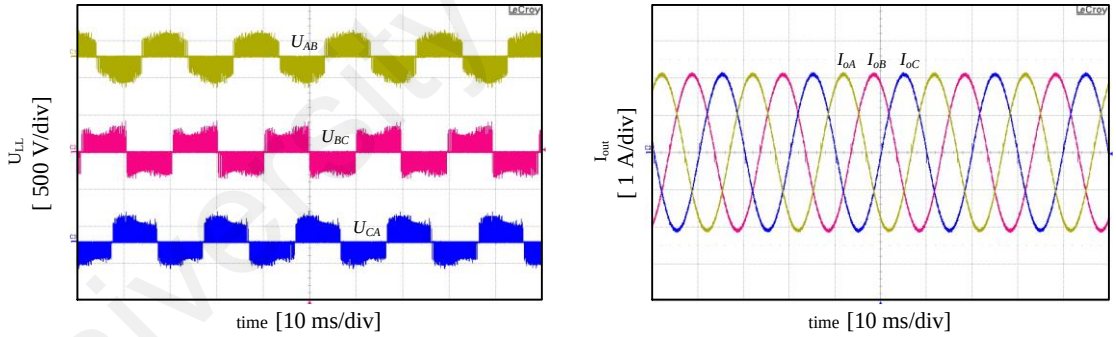

Figure 4-24: Steady-State performance (a) output three phase voltage, (b) stator current.

The experimental FFT analysis aims to prove the simulated THD results as can be seen in Figure 4-25. The spectrum of harmonics in frequency range and near to fundamental frequency has been shown between 5 and 250Hz for unfiltered input current at the converter side of filter in Figure 4-25(a), as well the input current on grid side of filter in

Figure 4-25(b). The FFT analysis of output current and voltage are displayed in Figure 4-25(c and d) respectively.

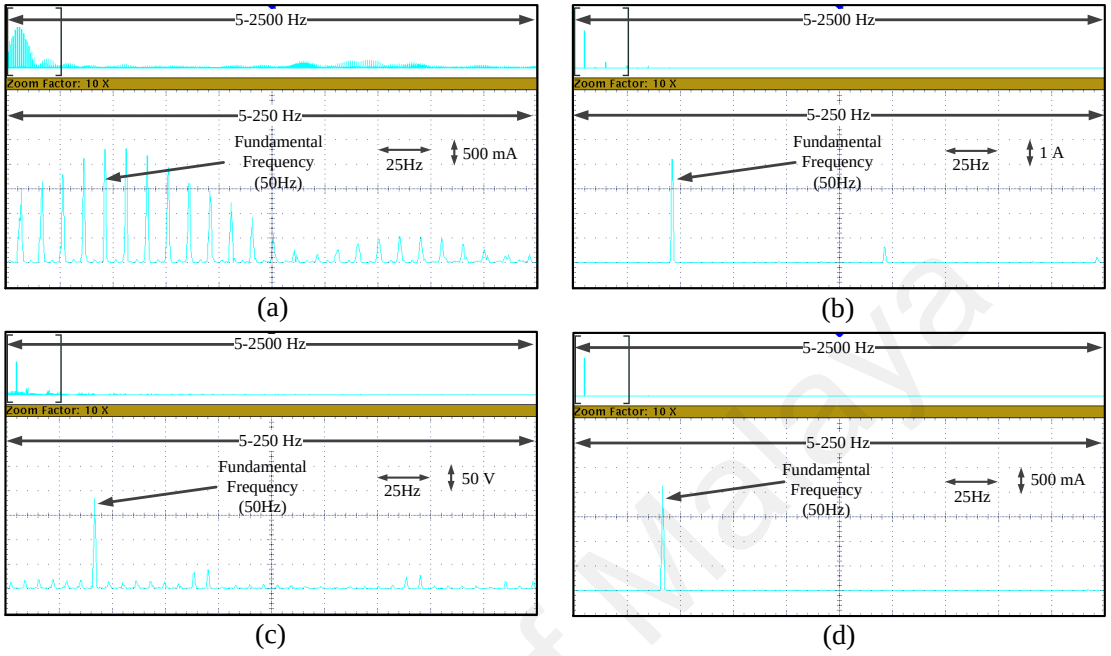

Figure 4-25: FFT Analysis around fundamental frequency (a) input current on converter side of filter(i1); (b) input current on grid side of filter; (c) output voltage; (d) output current**.**

4.2.2.2 Dynamic performance

Figure 4-26(a) shows the waveforms for the stator current of the IM driven by the proposed method with the current reference value stepping down from 2.1A (rated condition) to 50% of the full load, whereas the frequency is constant at 50Hz. It is concluded that the proposed method has the advantage of a fast dynamic response with acceptable THD in terms of changing the amplitude. Figure 4-26(b) displays the waveforms balanced stator current of the IM drove by the proposed method with a frequency step down from 50Hz to 30Hz, while the reference current is kept constant at the rated condition of 2.1A. The experimental results show that with the abrupt change in frequency, the magnitude does not change.

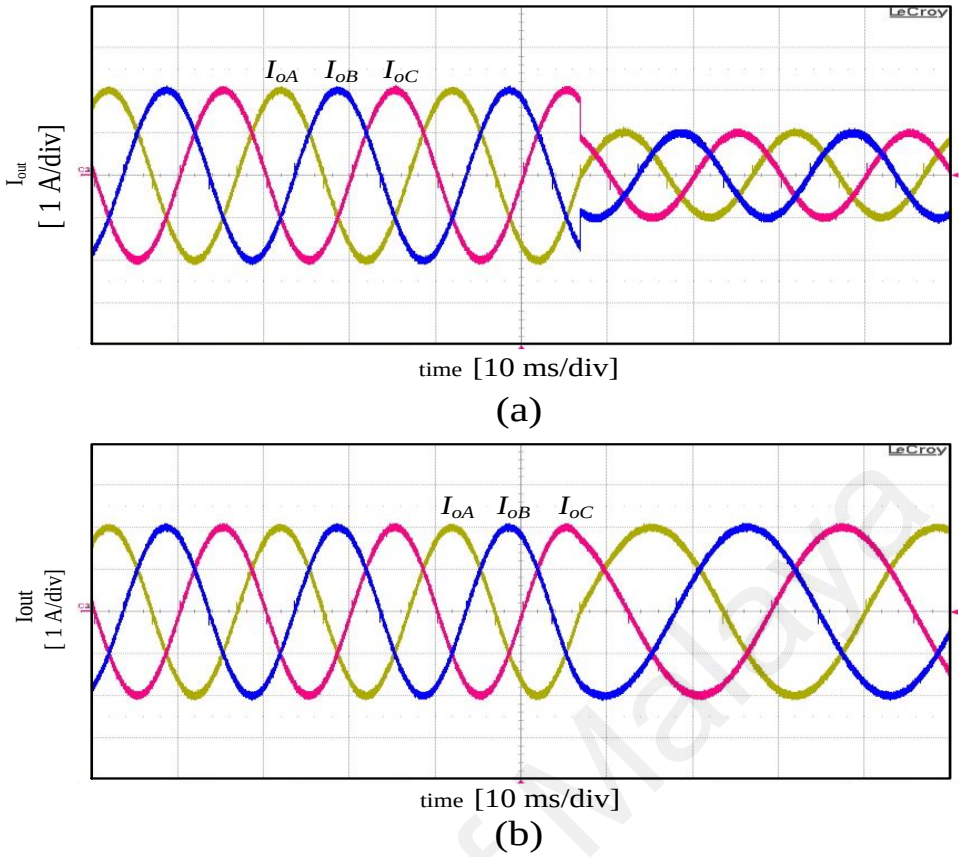

Figure 4-26: Dynamic response for variable (a) magnitude; (b) frequency

The proposed method shows a slight increase in the THD percentage for the output current with diminishing the rate of load current, which does not exceed 2.24% in the recommended testing margin. In the conventional method, an approximate linear relation can be seen between the reduction of the load and the increase in the output current THD with a sharper slope. The suggested technique optimizes the shoot-through timing to abate the distortion spectrum and increase the performance of the total system, which has 3.61% improvement in reduction of output current THD in compare with conventional model. The accuracy of the proposed method attains the exact target with only 1.3% lapse in steady-state analysis for the output current and 0.89% for the output voltage. It means that the error of normalization of three-phase waveform is almost 0.05% for output current, 0.32% for output voltage. The fast dynamic response in terms of magnitude with 3µs transient time and 6µs for frequency changing can be achieved based on the endorsed experimental testing.

A comparison between the obtained results of this investigation and other Z-source Matrix Converters in different research is provided in Table 4-2 which is covered the quantity of elements in topology, maximum voltage transfer ratio, the quantity and values of Z-source elements, switching frequency, output current THD, and maximum tolerated abnormality of input voltage. The proposed strategy aims to drive an IM fed by an USZSMC under 40% abnormal rate of input voltage, while, (Klumpner, 2006; Liu, Loh, Wang, & Han, 2012; Park, Lee, & Blaabjerg, 2012; Wijekoon, Klumpner, Zanchetta, & Wheeler, 2008) have lunched the static RL load. This result has at least 0.32% improvement in compare with comparable works in different algorithms. In recommended prototype, the overall volume and weight of the system is diminish and kept in 2.3 *L* which is significantly lower than the conventional back-to-back converter that has a volume of 4.6 *L* for the same power rating and thermal limitations of the USMC (Johann W Kolar et al., 2007; Round et al., 2006). It shows that the topology is suitable for kind of specific application such as aerospace production. Furthermore, the response of proposed driving method is quick and accurate enough to apply in this sensitive industry.

Table 4-2: Comparison of the performance of Z-source Matrix Converter with other findings.

Literature	Element quantity of MC topology		Voltage Transfer Ratio	Element quantity of Z-source				The value of Z-source elements		Switching Frequency (kHz)	Output current THD	Maximum Tolerated abnormality ratio
	Sw.	D.		L	C	Sw.	D.	L(*H*)	C(*F*)			
(Weizhang et al., 2013)	15	18	>1	2	2	0	0	0.65m	12.4µ	10	1.73%	40%
(Liu et al., 2012)	9	18	>1	2	2	0	0	20m	470µ	5*	Not mentioned	Balanced
(T. Wijekoon et al, 2008)	18	18	1	1	1	4	5	1.1m	20µ	10	15%	10%
(C. Klumpner, 2006)	18	18	0.955	0	1	4	4	-	1500µ	10	Not mentioned	10%
(Park et al., 2012)	12	30	1.15	2	2	1	1	3m	60µ	7.5	5.12%	30%
Proposed method	9	18	>1	2	2	0	0	0.25m	170 µ	10	1.41%	40%

*This is only for CSR part; the f_s of VSI part is not mentioned

4.2.3 30° sector DTC for USZSMC

For the purpose of verification, a 1 kW 3-phase IM is selected and fed by the abnormal AC programmable power supply through an implemented USZSMC with its 12-sector DTC control scheme. In addition, an experimental prototype as shown in Figure 3-16 is designed for testing of the proposed scheme with the same motor parameters as listed in Table 3-2. The value of capacitors and inductors of the Z-source network are selected to be the same as the obtained values in 3.3. It can be observed that the optimum value of capacitor and inductor is around 270μF and100μH respectively. Since these values are not plausible, a feasible point should be determined from the tracking curve. As a result, the feasible point of L and C can be achieved under the load condition as 250μH and 170μF respectively. The values are obtained tentatively in order to reach maximized performance, reliability and cost effectiveness, while minimizing the weight and volume of the overall driver. Moreover, the design rules in 3.3 should be followed to have a better performance at higher current level resulting in larger C and L values. The input filter elements have been set to the values so that the switching harmonics are eliminated (L_f =1mH and C_f=10μF).

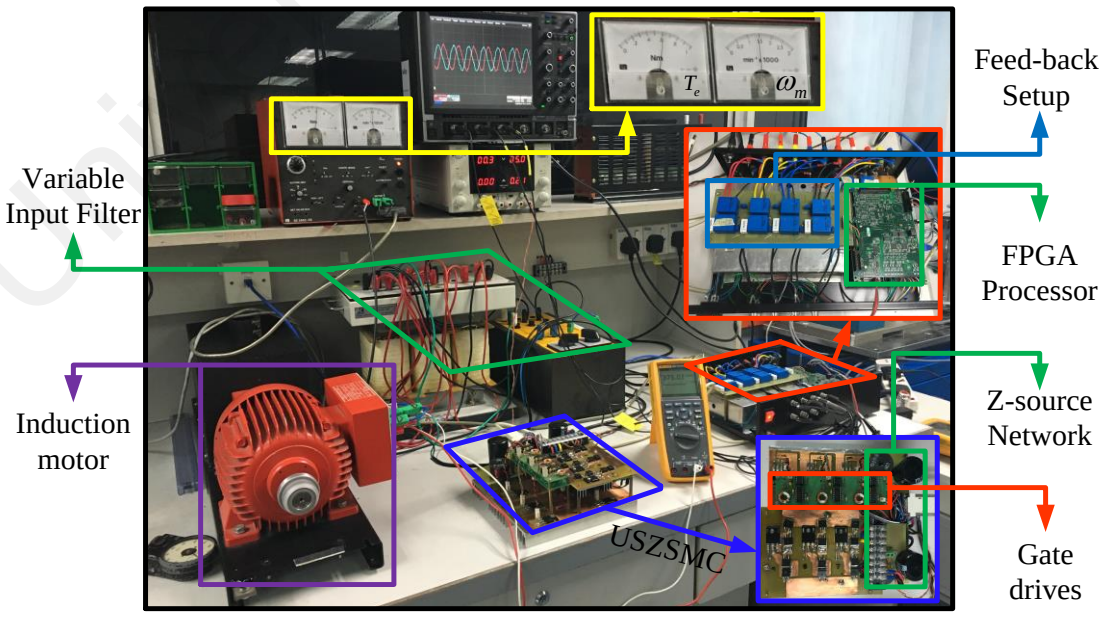

Figure 4-27: Photograph of the experimental setup of 12-sector DTC for USZSMC under abnormal main

To configure the USZSMC, IKW40N120H3, IGW30N60T IGBTs and IDP30E120 diode are used as depicted in Figure 4-27. The Ultra-sparse rectifier and a two-stage inverter are placed at the bottom level of the framework. The mid-level includes the Z-source network components without any sensor for detecting the capacitor voltage or inductor current. Gate drives, control unit process and feedback setup are also placed at the overhead. The GPIC-NI FPGA (field-programmable gate array) is used for the closed loop control as well.

4.2.3.1 Steady State performance

Steady-state performance has been tested under the condition which the abnormal voltage is supplied as illustrated in Figure 4-28(a). The abnormal condition is defined: Ua=380V and $|\Delta\emptyset_{Ua}|$= 20º, Ub= 228V and $|\Delta\emptyset_{Ub}|$= 10º, Uc=304V and $|\Delta\emptyset_{Uc}|$= 19º.

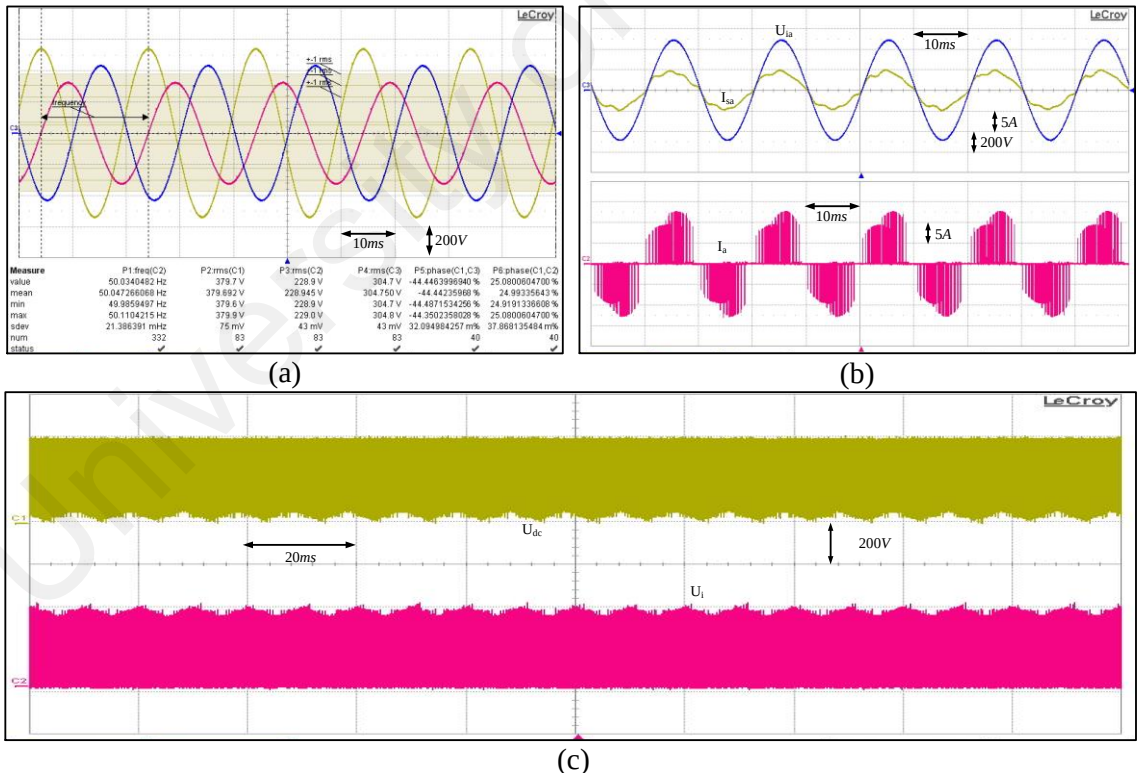

Figure 4-28: Steady-State performance (a) three phase abnormal input voltage. (b) input current after and before filter. (c) voltage of U_{dc} (after Z-source) and U_i (before Z-source) at dc-link.

As the input voltage, U_b and U_c are respectively engaged with a 40% and 20% abnormality rate from U_a. Figure 4-28(b) illustrates the input voltage (U_{ia}) and input currents (I_{sa}) after and before filter for phase A, which proves the unity of input power *(cosφ)*. Figure 4-28(c) also depicts the virtual DC-link voltage for after (U_i) and before (U_{dc}) Z-source network at the steady state and rated condition of IM by applying the shoot-through duty cycle.

Figure 4-29(a) and Figure 4-29(b) show the output voltage and current waveforms. As can be seen in the displayed measurement, the shift phase and magnitude in all of three phase are equal. It means the delivered power on IM not only is balanced but also compensated by the Z-source network.

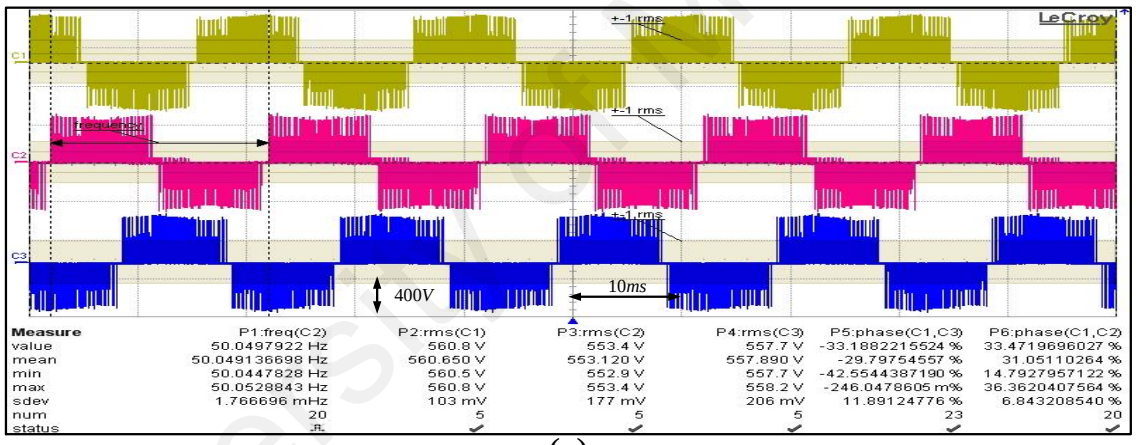

(a)

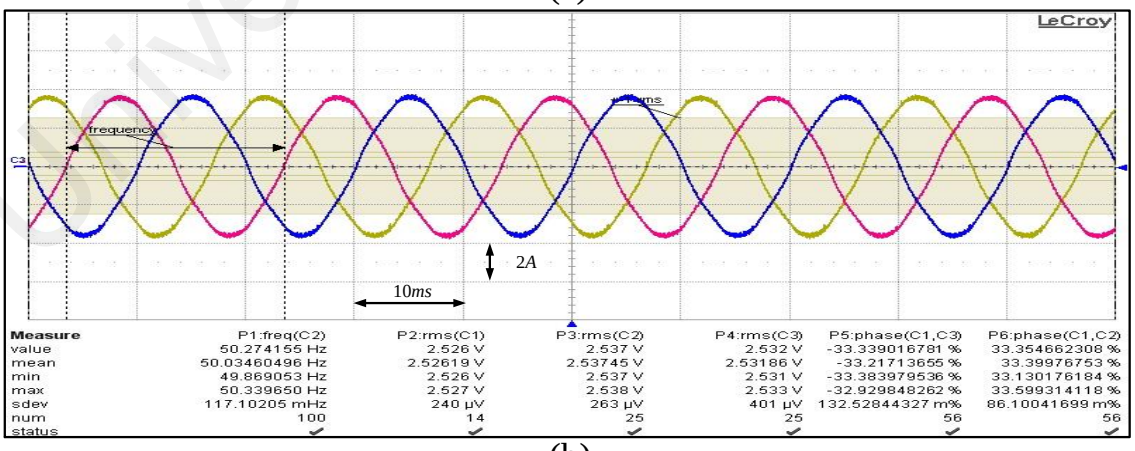

(b)

Figure 4-29: Steady-State performance (a) output three-phase voltage. (b) stator current.

Figure 4-30 shows the experimental FFT analysis, which verifies the simulated THD results. In Figure 4-30(a), the spectrum of harmonics is depicted for the range of

frequency between 5*Hz* and 250*Hz* for unfiltered input current at the converter side of filter. The spectrum of harmonics for the input current on grid side of filter is also shown in Figure 4-30(b). The FFT analysis of the output current and voltage are presented in Figure 4-30(c) and Figure 4-30(d) respectively.

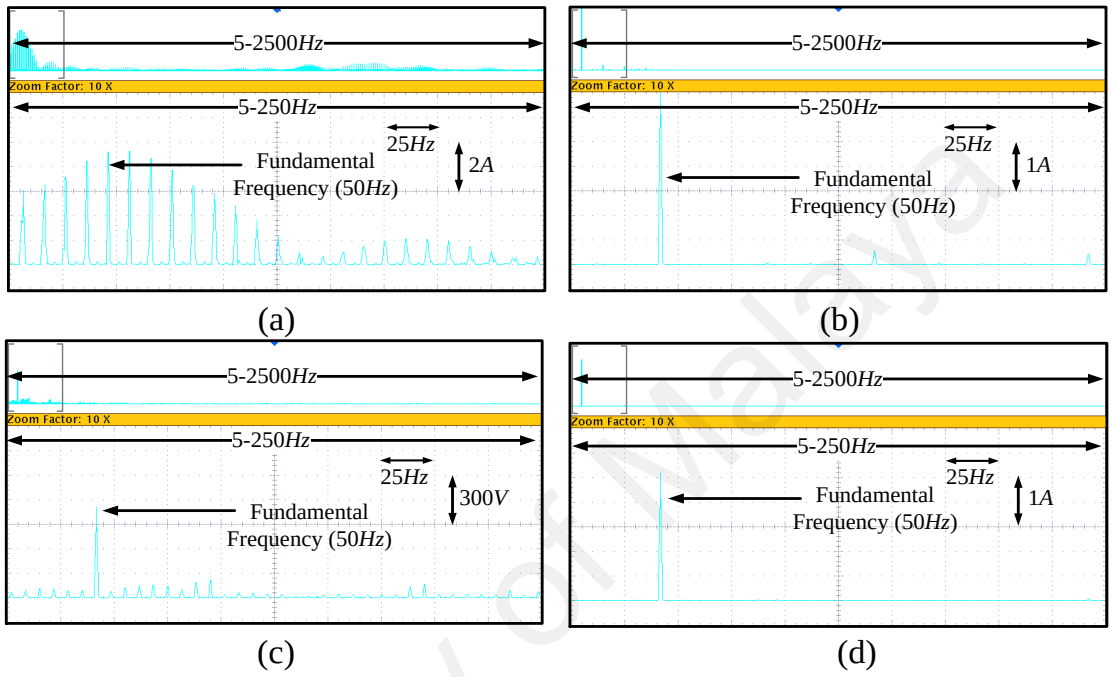

Figure 4-30: FFT Analysis around fundamental frequency (a) input current on converter side of filter. (b) input current on grid side of filter. (c) output voltage. (d) output current.

4.2.3.2 Dynamic performance

Figure 4-31 shows the dynamic performance of system in two benchmarks to validate the response of control algorithm. Figure 4-31(a) displays the waveforms of the IM stator current driven by the proposed control scheme with the electromagnetic torque value stepping down from rated condition (6.3*N.m*) to 50% of the full load keeping the speed constant at 1473*rpm*. It can be concluded that the proposed method has a considerably fast and dynamic response with acceptable THD with regards to changing T_e. It is validated that with the sudden changes of torque, the rotor speed is constant and the slight fluctuation can be practically neglected.

The waveforms of the stator current of IM are shown in Figure 4-31(b), whereas, the IM is driven by the proposed controlling scheme. The dynamic response examines 20% stepping up the electromagnetic torque from 5. 04N.m to 6.3*N.m*, and simultaneously, the rotor speed decreases from rated speed to 589*rpm* (40% decrement). The experimental results indicate that the quality of stator current does not change with the abrupt change in T_e and ω_m . Moreover, the torque ripple remains low under the unbalanced main.

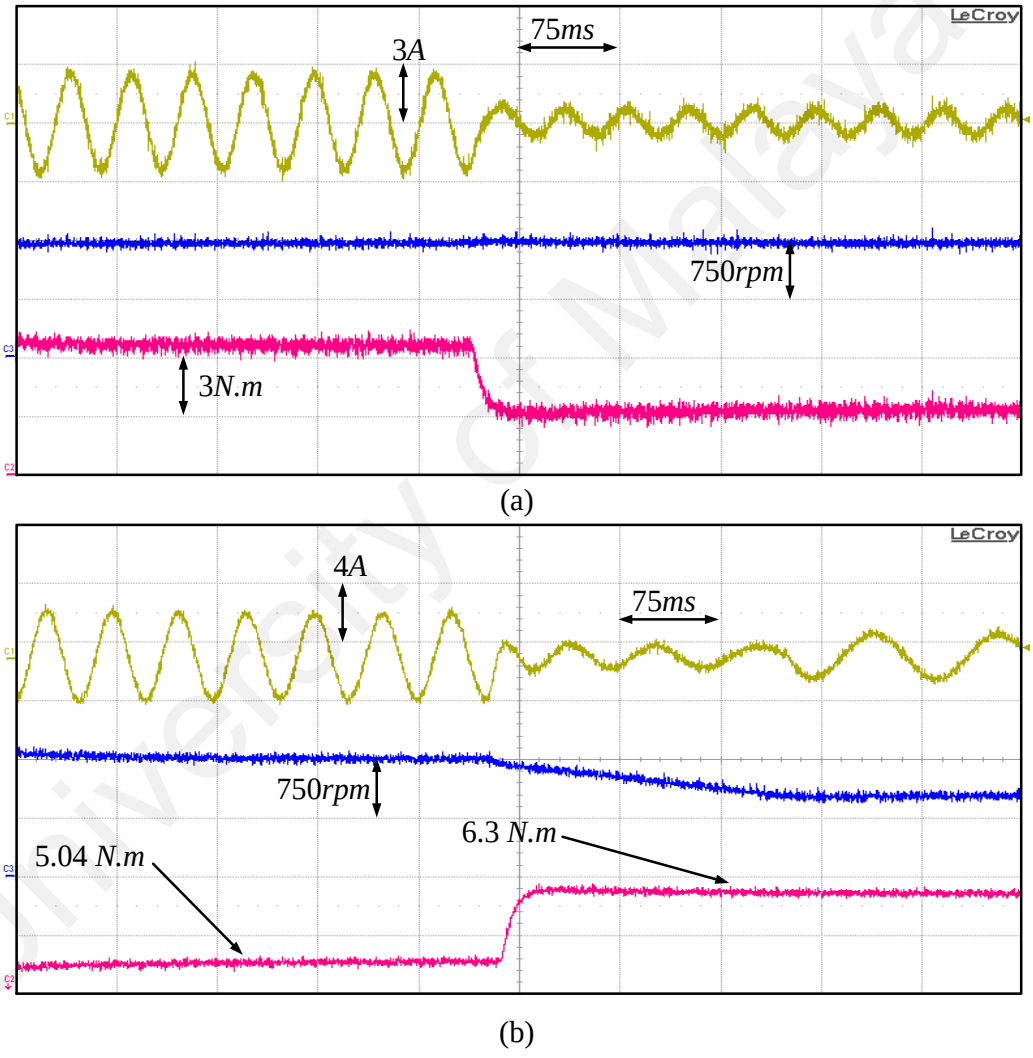

Figure 4-31: Dynamic response of stator current, rotor speed and electromagnetic torque (a) constant speed and 50% decrement of T_e. (b) 40% decrement of rotor speed and 20% increment of the electromagnetic torque.

4.3 Chapter Summary

The performance of the proposed switching strategy-based on matrix converter is compared with the conventional switching-based matrix converter for the DTC-based IM

drive in simulation and experimental benchmarks. The proposed switching strategy provides additional degrees of freedom to select voltage vectors and by selecting, the optimum switching state the torque ripple and switching frequency are reduced significantly. The complexity of control, increasing THD of output voltage, and computing time are the most significant disadvantages of 12-sector DTC method. As a result, the proposed switching method has proven to be also effective in order to diminish the total harmonic distortion (THD) of input current.

The performance of the proposed PSO-PI current control on USZSMC under abnormal input voltage is compared with conventional switching-based matrix converter. The integrated metaheuristic algorithm is employed to find the optimum values of PI and the coefficient of references, load current and modulation index in a single multimodal problem. While, the output current and voltage follow the reference point for all of three phase, the effect of all coefficients in minimizing THD is considered simultaneously. Therefore, the functionality of proposed model is verified by the simulation and experimental benchmarks.

Consequently, the combination of 12-sector DTC method by applying on USZSMC and 40% abnormal supplied is considered as the ultimate performance of this system. Therefore, the simulation and experimental results of this phase of study are compared with each other and approved the validity of the concept.

CHAPTER 5: CONCLUSIONS AND FUTURE WORKS

5.1 Conclusions

A novel space vector modulation based on twelve 30° sectors of both flux and voltage vectors within a circular locus of space vector for speed control of an IM fed by DMC based DTC was developed. The performance of the proposal switching strategy was compared to the hexagonal boundary space vector modulation based matrix converter for direct torque control of IM. The method provides additional degrees of freedom to select appropriate voltage vectors, which resulted in 60% reduction of torque ripple. The simulation and experimental results verify the applicability of the 12-sector space vector switching scheme for direct torque control of IM fed by DMC for different industrial application where, there is high demand for fast transient response of controlling scheme, less torque ripple and accurate control of torque with compact and high reliability adjustable speed drive.

The second aspect of this study illustrates an USZSMC under abnormal input voltage which could properly reduce the THD of output current equal to 1.10% by applying compensation method in Particle Swarm Optimization (PSO) PI controller. This result has at least 0.63% improvement in compare with comparable works in different algorithms. Although, the Z-source network is cause of intensification of low order harmonics in input and output current, the proposed method optimizes the shoot-through timing in order to abate the distortion spectrum and increase the performance of the total system 3.61% more than conventional model. The error of normalization of three-phase waveform is less than 0.05% for output current, 0.32% for output voltage, while the phase difference is synchronized on $(2\pi/3)\,rad$. The maximum tolerated abnormality for input voltage is 40%. However, this rate of toleration is one of the highest recommendation of recent years; as long as it is being limited to a specific rate, it can be sorted as a weakness of this method. Therefore, increasing the limitation of maximum tolerated abnormality

can bring new momentum for future studies. The appropriate simulation and experimental results display the reliability of planned model.

In the applications that require unidirectional power flow, high voltage transfer ratio, and lightweight, (such as aerospace industry) the Ultra-sparse Z-source Matrix Converter is well suited as meet all the above criteria. In this research, a new method has been proposed to determine the optimum value of Z-source parameters considering both timing and circuit approach. The PSO-PI controller is integrated with a DQ current control method in order to find the optimum coefficients values in a single multimodal problem. This control scheme can consider the inter-correlations of the other elements and the PI parameters together. The system has been tested for the unbalanced (40%), phase shifted (32°), and distorted (15%) of input voltage. By applying this compensation method, the control algorithm could properly reduce the THD of the output current equal to 1.41% in the rated condition of motor. The simulation and experimental results demonstrate that the proposed system produces high quality output currents.

As the ultimate benchmark, the combination of 30° sector DTC method by applying USZSMC topology and 40% abnormal supplied is considered. The promising results of simulation and the experimental test can verify that the system has an acceptable performance while the torque ripple of IM is diminished up to 60%, and simultaneously, the Z-source compensates the drop voltage ratio.

5.2 Future Works

One of the biggest difficulties in the operation of this converter was the commutation of the bidirectional switches. This problem has been solved by introducing intelligent and soft commutation techniques, giving new momentum to research in this area, while with a suitable modulation method there is no need for special commutation methods of MCs.

In the applications, that require unidirectional power flow, high voltage transfer ratio, and lightweight are the determinative factors in selecting converters. The USZSMC is well suited for these applications as meet all the above criteria. On the other hand, any unexpected faults in the system can result in a disastrous situation. Abnormal input can be considered as one of these faults. Hence, a driver is required to be designed to handle these faults safely.Therefore, according to the fast response, low torque ripple and THD of output current of the recommended control algorithm, this system can be implemented as a new generation of AC/AC converter. It may bring new momentum in this sensitive manufacturing and related researches.

REFERENCES

Ahmadi, M. Z. R. Z., Jidin, A., Othman, M. N., Jamil, M. L. M., Sutikno, T., & Nair, R. (2014). *High efficiency of switching strategy utilizing cascaded H-bridge multilevel inverter for high-performance DTC of induction machine.* Paper presented at the IEEE Conference on Energy Conversion (CENCON).

Alesina, A., & Venturini, M. (1989). Analysis and design of optimum-amplitude nine-switch direct AC-AC converters. *IEEE Transactions on power electronics, 4*(1), 101-112.

Alsofyani, I. M., & Idris, N. R. N. (2016). Simple Flux Regulation for Improving State Estimation at Very Low and Zero Speed of a Speed Sensorless Direct Torque Control of an Induction Motor. *IEEE Transactions on power electronics, 31*(4), 3027-3035.

An, S., Sun, X., Zhong, Y., & Matsui, M. (2012). *Research on a new and generalized method of discontinuous PWM strategies to minimize the switching loss.* Paper presented at the Innovative Smart Grid Technologies-Asia (ISGT Asia).

Andreu, J., Kortabarria, I., Ormaetxea, E., Ibarra, E., Martin, J. L., & Apinaniz, S. (2012). A Step Forward Towards the Development of Reliable Matrix Converters. *IEEE Transactions on Industrial Electronics, 59*(1), 167-183.

Arnold, M., & Andersson, G. (2011). *Model predictive control of energy storage including uncertain forecasts.* Paper presented at the Power Systems Computation Conference (PSCC), Stockholm, Sweden.

Aten, M., Towers, G., Whitley, C., Wheeler, P., Clare, J., & Bradley, K. (2006). Reliability comparison of matrix and other converter topologies. *IEEE Transactions on Aerospace and Electronic Systems, 42*(3), 867-875.

Blaabjerg, F., Chen, Z., & Kjaer, S. B. (2004). Power electronics as efficient interface in dispersed power generation systems. *IEEE Transactions on power electronics, 19*(5), 1184-1194.

Bose, B. K. (1986). Power electronics and AC drives. *Englewood Cliffs, NJ, Prentice-Hall, 416 p., 1*.

Casadei, D., Serra, G., & Tani, A. (1998). Reduction of the input current harmonic content in matrix converters under input/output unbalance. *IEEE Transactions on Industrial Electronics, 45*(3), 401-411.

Casadei, D., Serra, G., & Tani, A. (2001). The use of matrix converters in direct torque control of induction machines. *IEEE Transactions on Industrial Electronics, 48*(6), 1057-1064.

Changliang, X., & Xinmin, L. (2015). Z-Source Inverter-Based Approach to the Zero-Crossing Point Detection of Back EMF for Sensorless Brushless DC Motor. *IEEE Transactions on power electronics, 30*(3), 1488-1498.

Chattopadhyay, A. K. (1976). Digital Computer Simulation of an Adjustable-Speed Induction Motor Drive with a Cycloconverter-Type Thyristor-Commutator in the Rotor. *IEEE Transactions on Industrial Electronics and Control Instrumentation, IECI-23*(1), 86-92.

Chen, D. F., & Yao, K. C. (2006). *A Dynamical Modulation Strategy of the Virtual DC-Link Voltage for Matrix Converters Under Input Voltage Unbalance.* Paper presented at the 1ST IEEE Conference on Industrial Electronics and Applications.

Cho, Y., Lee, K.-B., Song, J.-H., & Lee, Y. I. (2015). Torque-ripple minimization and fast dynamic scheme for torque predictive control of permanent-magnet synchronous motors. *IEEE Transactions on power electronics, 30*(4), 2182-2190.

Cruz, S. (2004). Diagnosis of stator inter-turn short circuits in DTC induction motor drives. *IEEE Transactions on Industry Applications, 40*(5), 1349-1360.

Dabour, S. M., Allam, S., & Rashad, E. M. (2015). *A simple CB-PWM technique for five-phase matrix converters including over-modulation mode.* Paper presented at the IEEE 8th GCC Conference and Exhibition (GCCCE).

Dalla Vecchia, M., Brunelli Lazzarin, T., & Barbi, I. (2015). A Three-Phase AC-AC Converter in Open-Delta Connection Based on Switched Capacitor Principle. *IEEE Transactions on Industrial Electronics, 62*(10), 6035-6041.

Dehghan, S. M., Mohamadian, M., Yazdian, A., & Ashrafzadeh, F. (2010). A dual-input–dual-output Z-source inverter. *IEEE Transactions on power electronics, 25*(2), 360-368.

Dementyev, Y. N., Bragin, A. D., Kojain, N. V., & Udut, L. S. (2015). *Control system with sinusoidal PWM three-phase inverter with a frequency scalar control of induction motor.* Paper presented at the International Siberian Conference on Control and Communications (SIBCON), .

Dewan, S. B., & Rosenberg, S. A. (1970). Output Voltage in Three-Phase Pulsewidth-Modulated Inverters. *IEEE Transactions on Industry and General Applications, IGA-6*(6), 570-579.

Empringham, L., Kolar, J. W., Rodriguez, J., Wheeler, P. W., & Clare, J. C. (2013). Technological Issues and Industrial Application of Matrix Converters: A Review. *IEEE Transactions on Industrial Electronics, 60*(10), 4260-4271.

Erickson, R. W., & Maksimovic, D. (2007). *Fundamentals of power electronics*: Springer Science & Business Media.

Faraji, V., Aghasi, M., Khaburi, D. A., & Ghorbani, M. J. (2011). *A modified DTC for induction motor drive system fed by Indirect Matrix Converter using Active Learning Method.* Paper presented at the 2nd Power Electronics, Drive Systems and Technologies Conference (PEDSTC)

Friedli, T., Kolar, J. W., Rodriguez, J., & Wheeler, P. W. (2012). Comparative evaluation of three-phase AC–AC matrix converter and voltage DC-link back-to-back converter systems. *IEEE Transactions on Industrial Electronics, 59*(12), 4487-4510.

Gharakhani, A., & Radan, A. (2007). *Analytical study of affecting characteristic of voltage vectors of a three-level NPC inverter on torque and flux of DTC controlled drives.* Paper presented at the IEMDC IEEE International Conference on Electric Machines & Drives.

Helle, L., Larsen, K. B., Jorgensen, A. H., Munk-Nielsen, S., & Blaabjerg, F. (2004). Evaluation of modulation schemes for three-phase to three-phase matrix converters. *IEEE Transactions on Industrial Electronics, 51*(1), 158-171.

Holtz, J., & Boelkens, U. (1989). Direct frequency convertor with sinusoidal line currents for speed-variable AC motors. *IEEE Transactions on Industrial Electronics, 36*(4), 475-479.

Huber, L., & Borojevic, D. (1995). Space vector modulated three-phase to three-phase matrix converter with input power factor correction. *IEEE Transactions on Industry Applications, 31*(6), 1234-1246.

Huu-Nhan, N., & Hong-Hee, L. (2016). A DSVM Method for Matrix Converters to Suppress Common-mode Voltage With Reduced Switching Losses. *IEEE Transactions on power electronics, 31*(6), 4020-4030.

Iimori, K., Shinohara, K., Tarumi, O., Zixum, F., & Muroya, M. (1997). *New current-controlled PWM rectifier-voltage source inverter without DC link components.* Paper presented at the Power Conversion Conference - Nagaoka, Proceedings of the.

Irwin, J., Kazmierkowski, M. P., Krishnan, R., & Blaabjerg, F. (2002). *Control in power electronics: selected problems*: Academic press.

Ishiguro, A., Furuhashi, T., & Okuma, S. (1991). A novel control method for forced commutated cycloconverters using instantaneous values of input line-to-line voltages. *IEEE Transactions on Industrial Electronics, 38*(3), 166-172.

Jothibasu, S., & Mishra, M. K. (2015). An Improved Direct AC-AC Converter for Voltage Sag Mitigation. *IEEE Transactions on Industrial Electronics, 62*(1), 21-29.

Jussila, M., & Tuusa, H. (2006). *Comparison of direct and indirect matrix converters in induction motor drive.* Paper presented at the IEEE IECON 32nd Annual Conference on Industrial Electronics.

Karaman, E., Farasat, M., & Trzynadlowski, A. M. (2014). A Comparative Study of Series and Cascaded Z-Source Matrix Converters. *IEEE Transactions on Industrial Electronics, 61*(10), 5164-5173.

Kates, B. K. (1995). DC-AC inverter: Google Patents.

Kaufman, C. (1995). Rocky Mountain Research Lab. *Boulder, CO, private communication*.

Khoucha, F., Lagoun, M. S., Kheloui, A., & El Hachemi Benbouzid, M. (2011). A comparison of symmetrical and asymmetrical three-phase H-bridge multilevel inverter for DTC induction motor drives. *IEEE Transactions on Energy Conversion, 26*(1), 64-72.

Kiwoo, P., Eun-Sil, L., & Kyo-Beum, L. (2010). *A Z-source sparse matrix converter with a fuzzy logic controller based compensation method under abnormal input voltage conditions.* Paper presented at the IEEE International Symposium on Industrial Electronics (ISIE).

Klumpner, C. (2006). *A hybrid indirect matrix converter immune to unbalanced voltage supply, with reduced switching losses and improved voltage transfer ratio.* Paper presented at the Twenty-First Annual IEEE APEC Applied Power Electronics Conference and Exposition.

Kolar, J., Baumann, M., Schafmeister, F., & Ertl, H. (2002). *Novel three-phase AC-DC-AC sparse matrix converter.* Paper presented at the APEC Seventeenth Annual IEEE Applied Power Electronics Conference and Exposition.

Kolar, J. W., Friedli, T., Rodriguez, J., & Wheeler, P. W. (2011). Review of three-phase PWM AC–AC converter topologies. *IEEE Transactions on Industrial Electronics, 58*(11), 4988-5006.

Kolar, J. W., Friedli, T., Rodriguez, J., & Wheeler, P. W. (2011). Review of Three-Phase PWM AC/AC Converter Topologies. *IEEE Transactions on Industrial Electronics, 58*(11), 4988-5006.

Kolar, J. W., Schafmeister, F., Round, S. D., & Ertl, H. (2007a). Novel Three-Phase AC-AC Sparse Matrix Converters. *IEEE Transactions on power electronics, 22*(5), 1649-1661.

Kolar, J. W., Schafmeister, F., Round, S. D., & Ertl, H. (2007). Novel three-phase AC–AC sparse matrix converters. *IEEE Transactions on power electronics, 22*(5), 1649-1661.

Kolar, J. W., Schafmeister, F., Round, S. D., & Ertl, H. (2007b). Novel Three-Phase AC/AC Sparse Matrix Converters. *IEEE Transactions on power electronics, 22*(5), 1649-1661.

Korkmaz, Y., Korkmaz, F., Topaloglu, I., & Mamur, H. (2014). Comparing of Switching Frequency on Vector Controlled Asynchronous Motor. *International Journal on Soft Computing, Artificial Intelligence and Applications (IJSCAI), 3*(3/4), 19-27.

Kumar, B. S., Gupta, R., & Kumar, R. (2006a). *12-sector methodology of torque ripple reduction in a direct torque controlled induction motor drive.* Paper presented at the SICE-ICASE, 2006. International Joint Conference.

Kumar, B. S., Gupta, R., & Kumar, R. (2006b). *12-sector methodology of torque ripple reduction in a direct torque controlled induction motor drive.* Paper presented at the International Joint Conference SICE-ICASE.

Lascu, C., Boldea, I., & Blaabjerg, F. (2000). A modified direct torque control for induction motor sensorless drive. *IEEE Transactions on Industry Applications, 36*(1), 122-130.

Lascu, C., Jafarzadeh, S., Fadali, S. M., & Blaabjerg, F. (2015). *Direct torque control with feedback linearization for induction motor drives.* Paper presented at the 17th European Conference on Power Electronics and Applications (ECCE-Europe).

Lee, K.-B., & Blaabjerg, F. (2007). An improved DTC-SVM method for sensorless matrix converter drives using an overmodulation strategy and a simple nonlinearity compensation. *IEEE Transactions on Industrial Electronics, 54*(6), 3155-3166.

Lee, M. Y., Wheeler, P., & Klumpner, C. (2010). Space-vector modulated multilevel matrix converter. *IEEE Transactions on Industrial Electronics, 57*(10), 3385-3394.

Liu, X., Loh, P. C., Wang, P., & Han, X. (2012). Improved modulation schemes for indirect Z-source matrix converter with sinusoidal input and output waveforms. *IEEE Transactions on power electronics, 27*(9), 4039-4050.

Loh, P. C., Rong, R., Blaabjerg, F., & Wang, P. (2009). Digital carrier modulation and sampling issues of matrix converters. *IEEE Transactions on power electronics, 24*(7), 1690-1700.

Meng-Jiang, T., & Po-Tai, C. (2015). *Evaluation of PWM methods for suppressing circulating current among parallel connected four-pole inverters.* Paper presented at the IEEE Energy Conversion Congress and Exposition (ECCE).

Metidji, B., Taib, N., Baghli, L., Rekioua, T., & Bacha, S. (2013). Novel Single Current Sensor Topology for Venturini Controlled Direct Matrix Converters. *IEEE Transactions on power electronics, 28*(7), 3509-3516.

Mohan, N., & Undeland, T. M. (2007). *Power electronics: converters, applications, and design*: John Wiley & Sons.

Mutschler, P., & Marcks, M. (2002). A direct control method for matrix converters. *IEEE Transactions on Industrial Electronics, 49*(2), 362-369.

Ng, G. (2015). *An Improvement in Operation for Steel Rolling Mill Crop Cobble Shear using Direct Torque Control Induction Motor Drive.* UNIVERSITY OF IDAHO.

Nguyen, H. M., Lee, H.-H., & Chun, T.-W. (2009). *An investigation on direct space vector modulation methods for matrix converter.* Paper presented at the 35th Annual Conference of IEEE Industrial ElectronicsIECON.

Niaki, S. A. N., Iravani, R., & Kojori, H. (2014). *A robust commutation circuit for reliable single-step commutation of the matrix converter.* Paper presented at the Twenty-Ninth Annual IEEE Applied Power Electronics Conference and Exposition (APEC).

Ortega, C., Arias, A., Caruana, C., Balcells, J., & Asher, G. M. (2010). Improved waveform quality in the direct torque control of matrix-converter-fed PMSM drives. *IEEE Transactions on Industrial Electronics, 57*(6), 2101-2110.

Pan, L. (2014). LZ-Source Inverter. *IEEE Transactions on power electronics, 29*(12), 6534-6543.

Pan, L., Wang, B., Su, G., Cheng, B., & Peng, G. (2015). A Novel Space Vector modulation Scheme and Direct Torque Control for Four-switch BLDCM Using Flux Observer. *Journal of Electrical Engineering & Technology, 10*(1), 251-260.

Park, K., Lee, K.-B., & Blaabjerg, F. (2012). Improving output performance of a Z-source sparse matrix converter under unbalanced input-voltage conditions. *IEEE Transactions on power electronics, 27*(4), 2043-2054.

Patel, C., Day, R., Dey, A., Ramchand, R., Gopakumar, K., & Kazmierkowski, M. P. (2012). Fast direct torque control of an open-end induction motor drive using 12-sided polygonal voltage space vectors. *IEEE Transactions on power electronics, 27*(1), 400-410.

Patel, C., Ramchand, R., Rajeevan, P., Sivakumar, K., Das, A., Gopakumar, K., & Kazmierkowski, M. (2011). *Direct torque control scheme of IM drive with 12-sided polygonal voltage space vectors.* Paper presented at the Proceedings of the 14th European Conference on Power Electronics and Applications (EPE), .

Pavithra, S., Sivaprakasam, A., & Manigandan, T. (2011). *Performance Improvement of DTC for Induction Motor with 12-Sector Methodology.* Paper presented at the International Conference on Process Automation, Control and Computing (PACC)

Peng, F. Z. (2003). Z-source inverter. *IEEE Transactions on Industry Applications, 39*(2), 504-510.

Peng, F. Z., Shen, M., & Holland, K. (2007). Application of Z-source inverter for traction drive of fuel cell—battery hybrid electric vehicles. *IEEE Transactions on power electronics, 22*(3), 1054-1061.

Peng, F. Z., Shen, M., & Qian, Z. (2005). Maximum boost control of the Z-source inverter. *IEEE Transactions on power electronics, 20*(4), 833-838.

Persson, E. (1992). Transient effects in application of PWM inverters to induction motors. *IEEE Transactions on Industry Applications, 28*(5), 1095-1101.

Rahim, M. K., Patkar, F., Jidin, A., Ahmadi, M., Firdaus, R., Abd Halim, W., & Razi, A. (2015). *Reduced torque ripple and switching frequency using optimal DTC switching strategy for open-end winding of induction machines.* Paper presented at the IEEE 11th International Conference on Power Electronics and Drive Systems (PEDS).

Rashid, M. H. (2010). *Power electronics handbook: devices, circuits and applications*: Academic press.

Read, J. (1945). The calculation of rectifier and inverter performance characteristics. *Journal of the Institution of Electrical Engineers-Part II: Power Engineering, 92*(29), 495-509.

Reddy, B. D., Anish, N., Selvan, M., & Moorthi, S. (2015). Embedded Control of n-Level DC–DC–AC Inverter. *IEEE Transactions on power electronics, 30*(7), 3703-3711.

Richalet, J., Rault, A., Testud, J., & Papon, J. (1978). Model predictive heuristic control: Applications to industrial processes. *Automatica, 14*(5), 413-428.

Rodriguez, J., Pontt, J., Silva, C. A., Correa, P., Lezana, P., Cortés, P., & Ammann, U. (2007). Predictive current control of a voltage source inverter. *IEEE Transactions on Industrial Electronics, 54*(1), 495-503.

Rodriguez, J., Rivera, M., Kolar, J. W., & Wheeler, P. W. (2012). A review of control and modulation methods for matrix converters. *IEEE Transactions on Industrial Electronics, 59*(1), 58-70.

Round, S., Schafmeister, F., Heldwein, M., Pereira, E., Serpa, L., & Kolar, J. (2006). Comparison of performance and realization effort of a very sparse matrix converter to a voltage dc link pwm inverter with active front end. *電気学会論文誌D (産業応用部門誌), 126*(5), 578-588.

Schafmeister, F., & Kolar, J. W. (2012). Novel hybrid modulation schemes significantly extending the reactive power control range of all matrix converter topologies with low computational effort. *IEEE Transactions on Industrial Electronics, 59*(1), 194-210.

Schafmeister, F., Rytz, C., & Kolar, J. W. (2005). *Analytical calculation of the conduction and switching losses of the conventional matrix converter and the (very) sparse*

matrix converter. Paper presented at the APEC Twentieth Annual IEEE Applied Power Electronics Conference and Exposition.

Schönberger, J., Friedli, T., Round, S., & Kolar, J. (2007). *An ultra sparse matrix converter with a novel active clamp circuit.* Paper presented at the PCC Power Conversion Conference-Nagoya.

Shen, M., Joseph, A., Wang, J., Peng, F. Z., & Adams, D. J. (2007). Comparison of traditional inverters and Z-source inverter for fuel cell vehicles. *IEEE Transactions on power electronics, 22*(4), 1453-1463.

Siwakoti, Y. P., Peng, F. Z., Blaabjerg, F., Loh, P. C., & Town, G. E. (2015). Impedance-source networks for electric power conversion part I: a topological review. *IEEE Transactions on power electronics, 30*(2), 699-716.

Snary, P., Bhangu, B., Bingham, C. M., Stone, D. A., & Schofield, N. (2005). Matrix converters for sensorless control of PMSMs and other auxiliaries on deep-sea ROVs. *IEEE Proceedings on Electric Power Applications, 152*(2), 382-392.

Song, W., Zhong, Y., Zhang, H., Sun, X., Zhang, Q., & Wang, W. (2013). A study of Z-source dual-bridge matrix converter immune to abnormal input voltage disturbance and with high voltage transfer ratio. *IEEE Transactions on Industrial Informatics, 9*(2), 828-838.

Stacey, E. J. (1976). *An "unrestricted frequency changer" employing force commutated thyristors.* Paper presented at the IEEE Power Electronics Specialists Conference.

Taïb, N., Metidji, B., & Rekioua, T. (2014). A Fixed Switching Frequency Direct Torque Control Strategy for Induction Motor Drives Using Indirect Matrix Converter. *Arabian Journal for Science and Engineering, 39*(3), 2001-2011.

Takahashi, I., & Noguchi, T. (1986). A New Quick-Response and High-Efficiency Control Strategy of an Induction Motor. *IEEE Transactions on Industry Applications, IA-22*(5), 820-827.

Takeda, K., Yoshinaga, W., Tanaka, T., Naka, T., & Inomata, K. (2015). MATRIX CONVERTER, WIND POWER GENERATION SYSTEM, AND METHOD FOR CONTROLLING MATRIX CONVERTER: US Patent 20,150,188,443.

Tripathy, P. R., & Panigrahi, B. P. (2015). Study of Direct Torque Controlled 3-phase SCIM with Two and Three-level Inverters using ST-DTC and FR-DTC scheme. *Engineering, Technology & Applied Science Research, 5*(1), pp. 748-752.

Vas, P. (1998). *Sensorless vector and direct torque control*: Oxford Univ. Press.

Weerasinghe, S., Thrimawithana, D., & Madawala, U. (2014). Modelling Bi-directional Contactless Grid Interfaces with a Soft DC-link. *IEEE Transactions on power electronics, PP*(99), 1-1.

Weizhang, S., Yanru, Z., Hao, Z., Xiangdong, S., Qi, Z., & Wei, W. (2013). A Study of Z-Source Dual-Bridge Matrix Converter Immune to Abnormal Input Voltage Disturbance and With High Voltage Transfer Ratio. *Industrial Informatics, IEEE Transactions on, 9*(2), 828-838. doi: 10.1109/TII.2012.2222421

Wheeler, P., Clare, J., de Lillo, L., Bradley, K., Aten, M., Whitley, C., & Towers, G. (2006). *A Reliability Comparison of a Matrix Converter and an 18-Pulse Rectifier for Aerospace Applications.* Paper presented at the EPE-PEMC12th International Conference on Power Electronics and Motion Control.

Wheeler, P. W., Rodriguez, J., Clare, J. C., Empringham, L., & Weinstein, A. (2002). Matrix converters: a technology review. *IEEE Transactions on Industrial Electronics, 49*(2), 276-288.

Wheeler, P. W., Rodriguez, J., Clare, J. C., Empringham, L., & Weinstein, A. (2002). Matrix converters: a technology review. *Industrial Electronics, IEEE Transactions on, 49*(2), 276-288.

Wijekoon, T., Klumpner, C., Zanchetta, P., & Wheeler, P. W. (2008). Implementation of a hybrid AC–AC direct power converter with unity voltage transfer. *IEEE Transactions on power electronics, 23*(4), 1918-1926.

Xia, C., Zhao, J., Yan, Y., & Shi, T. (2014a). A Novel Direct Torque and Flux Control Method of Matrix Converter-Fed PMSM Drives. *IEEE Transactions on power electronics, 29*(10), 5417-5430.

Xia, C., Zhao, J., Yan, Y., & Shi, T. (2014b). A Novel Direct Torque Control of Matrix Converter-fed PMSM Drives Using Duty Cycle Control for Torque Ripple Reduction. *IEEE Transactions on Industrial Electronics, 61*(6), 2700-2713.

Xia, C. L., Zhao, J. X., Yan, Y., & Shi, T. N. (2014). A Novel Direct Torque Control of Matrix Converter-Fed PMSM Drives Using Duty Cycle Control for Torque Ripple Reduction. *IEEE Transactions on Industrial Electronics, 61*(6), 2700-2713.

Xiaoyan, H., Goodman, A., Gerada, C., Youtong, F., & Qinfen, L. (2012). A Single Sided Matrix Converter Drive for a Brushless DC Motor in Aerospace Applications. *IEEE Transactions on Industrial Electronics, 59*(9), 3542-3552.

Xiong, L., Poh Chiang, L., Peng, W., & Xiaoqing, H. (2012). Improved Modulation Schemes for Indirect Z-source Matrix Converter With Sinusoidal Input and Output Waveforms. *IEEE Transactions on power electronics, 27*(9), 4039-4050.

Yao, S., Xing, L., Mei, S., Hui, W., Hanbing, D., & Wenjing, X. (2015). Indirect Matrix Converter-Based Topology and Modulation Schemes for Enhancing Input Reactive Power Capability. *IEEE Transactions on power electronics, 30*(9), 4669-4681.

Zaid, S., Mahgoub, O., & El-Metwally, K. (2010). Implementation of a new fast direct torque control algorithm for induction motor drives. *IET Electric Power Applications, 4*(5), 305-313.

Zarri, L., Mengoni, M., Tani, A., & Ojo, J. O. (2014). Range of the Linear Modulation in Matrix Converters. *IEEE Transactions on Power Electronics, 29*(6), 3166-3178.

Zhao, J., Zhang, Z., Ren, Y., & Li, X. (2015). A direct torque intelligent control strategy for induction motor based on matrix converter. *Australian Journal of Electrical and Electronics Engineering*, 1-8.

Zhaoyang, Y., Minli, J., Chunjiang, Z., & Weiyang, W. (2012). An Integration SPWM Strategy for High-Frequency Link Matrix Converter With Adaptive Commutation in One Step Based on De-Re-Coupling Idea. *IEEE Transactions on Industrial Electronics, 59*(1), 116-128.

Zhu, M., Yu, K., & Luo, F. L. (2010). Switched inductor Z-source inverter. *IEEE Transactions on power electronics, 25*(8), 2150-2158.

Ziogas, P. D., Khan, S. I., & Rashid, M. H. (1986). Analysis and Design of Forced Commutated Cycloconverter Structures with Improved Transfer Characteristics. *IEEE Transactions on Industrial Electronics, IE-33*(3), 271-280.

Zmood, D. N., & Holmes, D. G. (2003). Stationary frame current regulation of PWM inverters with zero steady-state error. *IEEE Transactions on power electronics, 18*(3), 814-822.

APPENDIX A

LIST OF PUBLICATIONS AND PAPERS PRESENTED

ISI Journals:

1) **Sebtahmadi, S.S.**; Pirasteh, H.; Kaboli, S.H.A.; Radan, A.; Mekhilef, S., "A 12-Sector Space Vector Switching Scheme for Performance Improvement of Matrix-Converter-Based DTC of IM Drive," in ***IEEE Transactions on Power Electronics***, vol.30, no.7, pp.3804-3817, July 2015
2) **Sebtahmadi, S.**; Borhan A., and Mekhilef S., "A Current Control Approach for Abnormal Grid Supplied Ultra Sparse Z-source Matrix Converter with PSO-PI Controller of IM Drive" (3rd revision) - Submitted in ***IEEE Transaction on Power Electronics***

Proceeding:

1) **Sebtahmadi, S**.; A. Borhan, and S. Mekhilef. "An industrial optimum current control scheme for IM drive fed by Ultra Sparse Z-source Matrix Converter under abnormal input voltage." ***IEEE 2nd International Future Energy Electronics Conference (IFEEC)***, 2015. IEEE, 2015